Chem Soc Rev

# Proton Transfer Kinetics of Transition Metal Hydride Complexes and Implications for Fuel-Forming Reactions

| Journal: | *Chemical Society Reviews* |
|---|---|
| Manuscript ID | CS-REV-05-2023-000355.R1 |
| Article Type: | Review Article |
| Date Submitted by the Author: | 13-Jul-2023 |
| Complete List of Authors: | Montgomery, Charlotte; University of North Carolina, Chemistry<br>Amtawong, Jaruwan; University of North Carolina, Chemistry<br>Jordan, Aldo; University of Texas at El Paso, Department of Chemistry and Biochemistry<br>Kurtz, Daniel; University of North Carolina, Chemistry<br>Dempsey, Jillian; University of North Carolina, Chemistry |
| | |

SCHOLARONE™
Manuscripts

# Proton Transfer Kinetics of Transition Metal Hydride Complexes and Implications for Fuel-Forming Reactions

Charlotte L. Montgomery,[a] Jaruwan Amtawong,[a] Aldo M. Jordan,[a] Daniel A. Kurtz,[a]* and Jillian L. Dempsey[a]*

Proton transfer reactions involving transition metal hydride complexes are prevalent in a number of catalytic fuel-forming reactions, where the proton transfer kinetics to or from the metal center can have significant impacts on the efficiency, selectivity, and stability associated with the catalytic cycle. This review correlates the often slow proton transfer rate constants of transition metal hydride complexes to their electronic and structural descriptors and provides perspective on how to exploit these parameters to control proton transfer kinetics to and from the metal center. A toolbox of techniques for experimental determination of proton transfer rate contants is discussed, and case studies where proton transfer rate constant determination informs fuel-forming reactions are highlighted. Opportunities for extending proton transfer kinetic measurements to additional systems are presented, and the importance of synergizing the thermodynamics and kinetics of proton transfer involving transition metal hydride complexes are emphasized.

## Introduction

Proton transfer reactions are ubiquitous in a wide range of enzymatic and energy-related chemical transformations where they play a central role in hydrogen evolution, carbon dioxide reduction, nitrogen fixation, and water oxidation.[1–4] Transition metal hydride complexes are key intermediates in several of these catalytic transformations, whereby the transfer of proton to or from the metal center can have significant impact on the efficiency and selectivity of fuel-forming reactions.

Proton transfer reactions involving transition metal complexes can be described in general acidity terms where there are both thermodynamic and kinetic factors schematically described by Figure 1
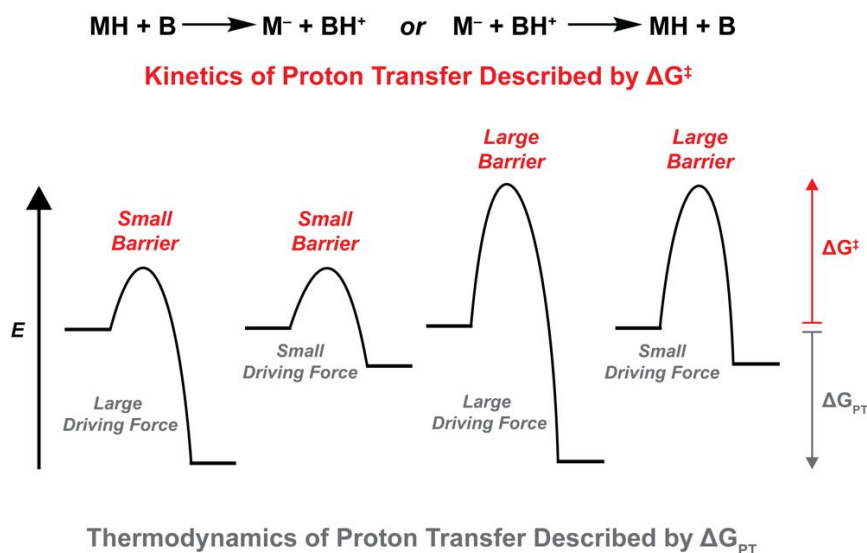


$$MH + B \longrightarrow M^- + BH^+ \quad or \quad M^- + BH^+ \longrightarrow MH + B$$

**Kinetics of Proton Transfer Described by $\Delta G^{\ddagger}$**

Small Barrier — Small Barrier — Large Barrier — Large Barrier

$E$

Large Driving Force — Small Driving Force — Large Driving Force — Small Driving Force

$\Delta G^{\ddagger}$

$\Delta G_{PT}$

**Thermodynamics of Proton Transfer Described by $\Delta G_{PT}$**

**Figure 1.** Reaction coordinate diagrams showcasing transition metal hydride complexes with different thermodynamic and kinetic acidities

a. Department of Chemistry, University of North Carolina at Chapel Hill, Chapel Hill, North Carolina, 27599-3290, USA. Email: dempseyj@email.unc.edu
†*Corresponding authors

The equilibrium constant, $K_{eq}$, for proton removal from the metal hydride (MH) in solution using an exogenous base (B) to form the respective conjugate base (M$^-$) and conjugate acid (BH$^+$) is a quantification of thermodynamic acidity (Equations 1 and 2). This equilibrium is used to quantify the p$K_a$ value of the metal hydride complex (Equation 3). The thermodynamic acidity can also be defined as the magnitude of the free energy change of the reaction under standard conditions, $\Delta G_{PT}$ (Equation 4).

$$\text{MH} + \text{B} \underset{}{\overset{K_{eq}}{\rightleftharpoons}} \text{M}^- + \text{BH}^+ \qquad (1)$$
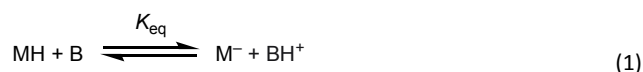
$$K_{eq} = \frac{[M^-][BH^+]}{[MH][B]} \qquad (2)$$

$$pK_a = -\log(K_{eq}) \qquad (3)$$

$$\Delta G_{PT} = -RT \ln(K_{eq}) \qquad (4)$$

Kinetic acidity refers to the rate at which a proton is transferred to or from the metal center. Equation 5 describes this reactivity, where $k_1$ is the rate constant to deprotonate a transition metal hydride complex (MH) using an exogenous base (B) and $k_{-1}$ is the rate constant to protonate a transition metal complex (M$^-$) using an exogenous acid (BH$^+$). The kinetic barrier for this proton transfer reaction can be described by the activation energy, $\Delta G^{\ddagger}$, where faster proton transfer reactions have smaller $\Delta G^{\ddagger}$ values based on the Arrhenius equation, shown as a proportionality in equation 6.

$$\text{MH} + \text{B} \underset{k_{-1}}{\overset{k_1}{\rightleftharpoons}} \text{M}^- + \text{BH}^+ \qquad (5)$$
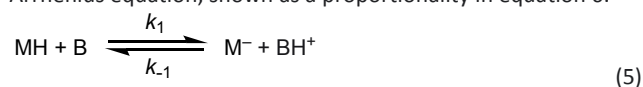
$$k \propto e^{\frac{-\Delta G^{\ddagger}}{RT}} \qquad (6)$$

The $\Delta G^{\ddagger}$ for metal-based proton transfer is often large, corresponding to smaller rate constants for proton transfer. Thus, to better advance catalytic transformations that proceed via metal hydride intermediates, it is imperative to understand and quantify kinetic acidity. For instance, if we can describe the relationships between kinetic barriers and structural and electronic descriptors for metal-based (de)protonation, then transition metal catalysts can be designed to lower kinetic barriers for fuel-forming processes.

The thermodynamic acidity of transition metal hydride complexes has been reviewed in the literature, and the thermodynamics of other metal hydride reactivity such as hydricity (hydride transfer) and H-atom transfer has also been discussed previously.[5–10] In addition, there has been recent review of kinetic hydricity of transition metal hydrides.[11] However, the kinetics of proton transfer, or kinetic acidity, involving transition metal hydride complexes has been documented to a lesser extent. In this Review, we will provide an overview of the current understanding of kinetic acidity of transition metal hydride complexes and outline the factors giving rise to slow proton transfer rate constants for this class of organometallic compounds. We will then discuss the breadth of techniques used to measure proton transfer rate constants involving transition metal hydride complexes. Finally, we discuss applications

of kinetic acidity in fuel-forming reactions and provide perspective on how kinetic acidity can be leveraged to aid future catalyst design.

## Part I: Understanding and Quantifying Kinetic Acidity

### Effects of Electronic and Structural Changes on Proton Transfer Kinetics

The proton transfer rate constants for reactions involving metal hydride complexes are generally slow and often times below the diffusion limit. The slow kinetics suggest that there are kinetically limiting factors for proton transfer to or from the metal center, which is in stark contrast to proton transfer involving oxygen or nitrogen acids and bases at similar thermodynamic driving forces. A compiled list of proton transfer rate constants for a variety of different transition metal hydrides and the associated $\Delta G_{PT}$ values for the reactions studied is presented in Table 1. In this section, we provide experimental case studies to show how electronic and structural rearrangements manifest in slower observed proton transfer rate constants for reactions involving transition metal hydrides vs. organic acids. We will also discuss theoretical studies that explore the influence of electronic and structural rearrangements on proton transfer rate constants.

In 1979, Pearson and coworkers reported rate constants for deprotonation of transition metal carbonyl hydrides in methanol.[12] They observed that when isoenergetic reactions were monitored, the magnitude of the rate constants was similar to those for the deprotonation of carbon-based acids like (4-nitrophenyl)nitromethane and nitroparaffins. The proton transfer rate constants for the deprotonation of metal carbonyl hydrides with methoxide range from $10^2 - 10^6$ M$^{-1}$ s$^{-1}$ in methanol, which are orders of magnitude lower than those for the deprotonation rates of nitrogen- or oxygen-based acids, which are typically diffusion limited ($k_{PT} \sim 10^{10}$ M$^{-1}$ s$^{-1}$). The authors rationalized this observation using electronic and geometric arguments. When a nitrogen or oxygen-based acid is deprotonated, the electron pair in the N-H or O-H bond stays localized on the nitrogen or oxygen, and there is generally very little geometric or electronic rearrangement associated with deprotonation.[13] However, when a transition metal hydride complex is deprotonated, the coordination number at the central metal ion is lowered and the result is significant electronic and structural differences between the protonated and deprotonated form of the complex. Both the electronic and geometric changes are directly observed in a study by Marchetti and coworkers on cobalt carbonyl hydride complexes.[14] In the deprotonation of HCo(CO)$_4$ by NEt$_3$, the $\nu$(CO) values decrease by ~100 cm$^{-1}$ indicating a higher degree of backbonding, and the geometry changes from trigonal bipyramidal to tetrahedral upon deprotonation (Figure 2).

**Table 1.** Kinetic and thermodynamic acidity/basicity values of proton transfer reactions involving transition metal hydride complexes.

| Deprotonation Reactions | | | | | | |
|---|---|---|---|---|---|---|
| Compound | Base | $\Delta G_{PT}$ (kcal mol$^{-1}$) | $k_{PT}$ @ 25°C (M$^{-1}$ s$^{-1}$) | Solvent | Technique | Ref. |
| Monometallic Systems | | | | | | |
| CpCr(CO)$_3$H | CpCr(CO)$_3^-$ | 8.99 | 1.80 x 10$^4$ | MeCN | NMR line broadening | 36 |
| CpCr(CO)$_3$H | aniline | 6.81 | 1.80 x 10$^4$ | MeCN | NMR line broadening | 36 |
| CpMo(CO)$_3$H | CpMo(CO)$_3^-$ | 6.54 | 2.50 x 10$^3$ | MeCN | NMR line broadening | 36 |
| CpMo(CO)$_3$H | aniline | 11.98 | 3.90 x 10$^3$ | MeCN | NMR line broadening | 36 |
| CpW(CO)$_3$H | CpW(CO)$_3^-$ | 0.00 | 6.50 x 10$^2$ | MeCN | NMR line broadening | 36 |
| CpW(CO)$_3$H | aniline | 8.85 | 2.50 x 10$^2$ | MeCN | NMR line broadening | 36 |
| CpW(CO)$_3$H | p-cyanoaniline | 6.13 | 3.00 x 10$^0$ | MeCN | NMR line broadening | 36 |
| CpW(CO)$_3$H | ethyl p-aminobenzoate | 10.21 | 8.00 x 10$^0$ | MeCN | NMR line broadening | 36 |
| CpW(CO)$_3$H | p-iodoaniline | 7.49 | 5.10 x 10$^1$ | MeCN | NMR line broadening | 36 |
| CpW(CO)$_3$H | p-methylaniline | 5.45 | 6.80 x 10$^2$ | MeCN | NMR line broadening | 36 |
| CpW(CO)$_3$H | p-methoxyaniline | 9.40 | 8.30 x 10$^2$ | MeCN | NMR line broadening | 36 |
| CpFe(CO)$_2$H | aniline | 14.30 | 4.00 x 10$^{-1}$ | MeCN | NMR line broadening | 36 |
| Cp*Mo(CO)$_3$H | aniline | -1.63 | 4.90 x 10$^1$ | MeCN | NMR line broadening | 36 |
| Mn(CO)$_5$H | aniline | -0.41 | 2.10 x 10$^2$ | MeCN | NMR line broadening | 36 |
| Mn(CO)$_5$H | p-cyanoaniline | 0.14 | 4.00 x 10$^0$ | MeCN | NMR line broadening | 36 |
| Mn(CO)$_5$H | p-bromoaniline | 0.41 | 6.50 x 10$^1$ | MeCN | NMR line broadening | 36 |
| Mn(CO)$_5$H | p-methylaniline | 0.95 | 4.20 x 10$^2$ | MeCN | NMR line broadening | 36 |
| Mn(CO)$_5$H | ethyl p-aminobenzoate | 0.00 | 1.50 x 10$^1$ | MeCN | NMR line broadening | 36 |
| Re(CO)$_5$H | aniline | 1.09 | 1.40 x 10$^{-2}$ | MeCN | NMR line broadening | 36 |
| Co(CO)$_4$H | aniline | 5.18 | 1.70 x 10$^6$ | MeCN | NMR line broadening | 36 |
| Co(CO)$_4$H | p-iodoaniline | 4.63 | 2.40 x 10$^5$ | MeCN | NMR line broadening | 36 |
| Co(CO)$_4$H | p-(CF$_3$)aniline | 4.36 | 9.50 x 10$^4$ | MeCN | NMR line broadening | 36 |
| Co(CO)$_4$H | ethyl p-aminobenzoate | 2.59 | 7.70 x 10$^4$ | MeCN | NMR line broadening | 36 |

| Co(CO)$_4$H | 2,4-dichloroaniline | 11.03 | $5.20 \times 10^4$ | MeCN | NMR line broadening | 36 |
|---|---|---|---|---|---|---|
| Co(CO)$_4$H | p-CN-aniline | 3.13 | $4.10 \times 10^4$ | MeCN | NMR line broadening | 36 |
| Fe(CO)$_4$H$_2$ | Fe(CO)$_4$H- | 13.89 | $1.40E \times 10^3$ | MeCN | NMR line broadening | 36 |
| Fe(CO)$_4$H$_3$ | aniline | 6.13 | $5.40 \times 10^4$ | MeCN | NMR line broadening | 36 |
| Fe(CO)$_4$H$_4$ | p-cyanoaniline | 2.59 | $7.60 \times 10^2$ | MeCN | NMR line broadening | 36 |
| Fe(CO)$_4$H$_5$ | 2,4-dichloroaniline | -0.54 | $1.10E \times 10^3$ | MeCN | NMR line broadening | 36 |
| Fe(CO)$_4$H$_6$ | ethyl p-aminobenzoate | 9.81 | $1.90E \times 10^3$ | MeCN | NMR line broadening | 36 |
| Fe(CO)$_4$H$_7$ | p-I-aniline | -5.31 | $7.40E \times 10^3$ | MeCN | NMR line broadening | 36 |
| Ru(CO)$_4$H$_2$ | aniline | -5.86 | $8.00 \times 10^0$ | MeCN | NMR line broadening | 36 |
| Os(CO)$_4$H$_2$ | Et$_3$N | 0.00 | $4.80 \times 10^2$ | MeCN | NMR line broadening | 36 |
| Os(CO)$_4$H$_3$ | aniline | 20.43 | $1.00 \times 10^{-2}$ | MeCN | NMR line broadening | 36 |
| Os(CO)$_4$(CH$_3$)H | Et$_3$N | -11.98 | $3.40 \times 10^1$ | MeCN | NMR line broadening | 36 |
| Os$_2$(CO)$_8$H$_2$ | Et$_3$N | 8.99 | $1.20 \times 10^1$ | MeCN | NMR line broadening | 36 |
| [Rh$_{13}$(CO)$_{24}$H$_3$]2- | aniline | 6.81 | $1.20 \times 10^{-3}$ | MeCN | IR spectrosopy | 15 |
| [H$_4$Re(PMe$_2$Ph)$_4$]+ | DNBu$_2$ | 6.54 | $5.00 \times 10^{-6}$ | MeCN | NMR spectroscopy? | 44 |
| Os(CO)$_4$(H)$_2$ | sodium methoxide | 11.98 | $8.20 \times 10^4$ | MeOH | Stopped-flow UV-Vis | 44 |
| Fe(CO)$_4$(H)$_2$ | sodium methoxide | 0.00 | $1.30 \times 10^6$ | MeOH | Stopped-flow UV-Vis | 12 |
| HMo(CO)$_2$(dppe) | pyridine | 8.85 | $6.90 \times 10^{-5}$ | DCM | FT-IR | 12 |
| H$_4$Re(PMe$_2$Ph)$_4$]$^+$ | aniline | 6.13 | $<10 \times 10^{-9}$ | MeCN | NMR line broadening | 42 |
| *Multimetallic Systems* | | | | | | |
| Ru$_4$(CO)$_{12}$H$_4$ | sodium methoxide | -6.81 | $6.20E \times 10^3$ | MeOH | Stopped-flow UV-Vis | 12 |
| FeRu$_3$(CO)$_{12}$H$_4$ | sodium methoxide | -4.49 | $8.60E \times 10^3$ | MeOH | Stopped-flow UV-Vis | 12 |
| Ru$_4$(CO)$_{13}$H$_2$ | sodium methoxide | -2.72 | $5.30 \times 10^2$ | MeOH | Stopped-flow UV-Vis | 12 |
| FeRu$_3$(CO)$_{13}$H$_2$ | sodium methoxide | -3.27 | $7.70 \times 10^2$ | MeOH | Stopped-flow UV-Vis | 12 |
| Os$_4$(CO)$_{12}$H$_4$ | sodium methoxide | -6.40 | $2.30E \times 10^3$ | MeOH | Stopped-flow UV-Vis | 12 |
| [Rh$_{13}$(CO)$_{24}$H$_3$]$^{2-}$ | toluidine | -0.27 | $1.42 \times 10^{-3}$ | MeCN | IR | 15 |
| [Rh$_{13}$(CO)$_{24}$H$_3$]$^{2-}$ | aniline | 0.54 | $1.20 \times 10^{-3}$ | MeCN | IR | 15 |
| [Rh$_{13}$(CO)$_{24}$H$_3$]$^{2-}$ | p-iodoaniline | 1.91 | $2.10 \times 10^{-4}$ | MeCN | IR | 15 |
| [Rh$_{13}$(CO)$_{24}$H$_3$]$^{2-}$ | p-CF$_3$-aniline | 3.27 | $1.30 \times 10^{-4}$ | MeCN | IR | 15 |
| **Protonation Reactions** | | | | | | |
| **Compound** | **Acid** | **$\Delta G_{PT}$ (kcal mol$^{-1}$)** | **$k_{PT}$ (M$^{-1}$ s$^{-1}$)** | **Solvent** | **Technique** | **Ref.** |
| *Monometallic Systems with Direct Metal Protonation* | | | | | | |

| | | | | | | |
|---|---|---|---|---|---|---|
| $Co(dmgBF_2)_2(CH_3CN)_2$ | 4-methoxyanilinium | - | $3.06 \times 10^4$ | MeCN | FOWA | 73 |
| $Co(dmgBF_2)_2(CH_3CN)_2$ | 4-tert-butylanilinium | - | $1.45 \times 10^5$ | MeCN | FOWA | 73 |
| $Co(dmgBF_2)_2(CH_3CN)_2$ | anilinium | - | $4.66 \times 10^5$ | MeCN | FOWA | 73 |
| $Co(dmgBF_2)_2(CH_3CN)_2$ | 4-Cl-anilinium | - | $3.70 \times 10^6$ | MeCN | FOWA | 73 |
| $Co(dmgBF_2)_2(CH_3CN)_2$ | 4-$(OCF_3)$-anilinium | - | $9.91 \times 10^6$ | MeCN | FOWA | 73 |
| $Co(dmgBF_2)_2(CH_3CN)_2$ | 4-methylbenzoateaniliniium | - | $3.80 \times 10^7$ | MeCN | FOWA | 73 |
| $Co(dmgBF_2)_2(CH_3CN)_2$ | 4-$CF_3$-anilinium | - | $7.97 \times 10^7$ | MeCN | FOWA | 73 |
| $Co(dmgBF_2)_2(CH_3CN)_2$ | 4-CN-anilinium | - | $2.73 \times 10^8$ | MeCN | FOWA | 73 |
| $[Co(dmgH)_2pyCl]$ | $Et_3NH^+$ | -6.38 | $\geq 10^8$ | DMF | CV Simulation | 81 |
| $[Co(dmgH)_2(4-Me_2NC_5H_4N)Cl]$ | $Et_3NH^+$ | -6.38 | $\geq 10^8$ | DMF | CV Simulation | 81 |
| $[Co(dmgH)_2(4-t-BuNHC(=O)C_5H_4N)Cl]$ | $Et_3NH^+$ | -3.54 | $\geq 10^8$ | DMF | CV Simulation | 81 |
| $[Co(dmgH)_2(OH_2)_2]$ | $Et_3NH^+$ | -4.08 | $\geq 10^4$ | DMF | CV Simulation | 81 |
| FeTPP | $HNEt_3Cl$ | - | $2.00 \times 10^8$ | DMF | Peak shift analysis | 91 |
| FeTPP + Quin cocatalyst | AcOH | - | $1.00 \times 10^{10}$ | DMF | FWHM Plateau Current | 92 |
| FeTPP + DABCO cocatalyst | AcOH | - | $2.00 \times 10^9$ | DMF | FWHM Plateau Current | 92 |
| FeTPP + $NEt_3$ cocatalyst | AcOH | - | $4.00 \times 10^9$ | DMF | FWHM Plateau Current | 92 |
| FeTPP + N-EtPip cocatalyst | AcOH | - | $3.00 \times 10^9$ | DMF | FWHM Plateau Current | 92 |
| FeTPP + N(i-Pr)$_2$Et cocatalyst | AcOH | - | $2.00 \times 10^8$ | DMF | FWHM Plateau Current | 92 |
| $[Pt(dmpe)_2]$ | phenol | -2.74 | $> 1 \times 10^{5b}$ | MeCN | CV Scan Rate Dependent Data | 94 |
| *Monometallic Systems with Ligand Cooperativity* | | | | | | |
| $Ni(P_2^{Ph}N_2^{Ph})_2^c$ | anilinium | - | $1.20 \times 10^6$ | MeCN | Peak shift analysis | 108 |
| $Ni(P_2^{Ph}N_2^{Ph})_2^c$ | anilinium | - | $6.50 \times 10^6$ | MeCN | FOWA | 108 |
| $[Ni(P_2^{Ph}N_2^{Ph})]^{+c}$ | $DMF(H^+)$ | - | $3.30 \times 10^5$ | MeCN | Ecat/2 FOWA | 109 |
| $[Ni(P_2^{Ph}N_2^{Ph})_2]^{2+}$ | $DMF(H^+)$ | - | $7.50 \times 10^4$ | MeCN | Catalytic peak current analysis | 106 |
| $[Ni(P_2^{Ph}N_2^{C6H4X})_2]^{2+}$ X = $CH_2P(O)(OEt)_2$ | $DMF(H^+)$ | 0.54 | $1.30 \times 10^3$ | MeCN | Catalytic peak current analysis | 107 |
| $[Ni(P_2^{Cy}N_2^{Arg})_2]^{6+}$ | $H_3O^+$ | 5.98 | $1.0 \times 10^{6b}$ | $H_2O$ | CV Simulation | 110 |
| Co-hangman porphyrin | -[a] | $8.04^{108}$ | $8.5 \times 10^{6b}$ | MeCN | Peak shift analysis & CV Simulations | 112 |
| Co-nonhangman porphyrin | benzoic acid | $8.87^{108}$ | $1.00 \times 10^3$ | MeCN | Peak shift analysis & CV Simulations | 112 |
| $[Ni(SPh)(triphos)]^d$ | lutidinium | - | $5.00 \times 10^0$ | MeCN | Stopped-flow UV-Vis | 125 |
| $[Ni(SEt)(triphos)]^d$ | lutidinium | - | $1.20 \times 10^3$ | MeCN | Stopped-flow UV-Vis | 126 |
| $[Ni(2\text{-Spy})(triphos)]^{+d}$ | lutidinium | - | $1.30 \times 10^4$ | MeCN | Stopped-flow UV-Vis | 126 |
| $[Co((DO)_2BF_2)pnBr_2]$ | 4-CN-anilinium | - | $1.20 \times 10^6$ | MeCN | Peak shift analysis | 160 |
| $[Co(N_4H)Cl_2]^+$ | 4-CN-anilinium | - | $2.50 \times 10^4$ | MeCN | FOWA & Ecat/2 FOWA | 161 |
| $[Co(N_4H)Cl_2]^+$ | 4-CN-anilinium | - | $2.05 \times 10^4$ | MeCN | Catalytic peak current analysis | 161 |
| CoCp(depe)[e] | phenol | 7.54 | $8.70 \times 10^3$ | MeCN | Peak shift analysis | 45 |
| CoCp(depe)[e] | 4-$CH_3$-phenol | 5.31 | $1.80 \times 10^4$ | MeCN | Peak shift analysis | 45 |
| CoCp(depe)[e] | 4-$CF_3$-phenol | 2.52 | $7.00 \times 10^5$ | MeCN | Peak shift analysis | 45 |

| | | | | | | |
|---|---|---|---|---|---|---|
| CoCp(depe)[e] | 4-Cl-phenol | 2.51 | $1.20 \times 10^5$ | MeCN | Peak shift analysis | 45 |
| CoCp(depe)[e] | acetic acid | -0.12 | $5.60 \times 10^6$ | MeCN | Peak shift analysis | 45 |
| CoCp(depe)[e] | benzoic acid | -2.85 | $3.60 \times 10^7$ | MeCN | Peak shift analysis | 45 |
| CoCp(depe)[e] | 2,3,5,6-$F_4$-phenol | -4.74 | $4.40 \times 10^7$ | MeCN | Peak shift analysis | 45 |
| CoCp(depe)[e] | benzylammonium | -9.11 | $3.80 \times 10^7$ | MeCN | Peak shift analysis | 45 |
| CoCp(depe)[e] | salicylic acid | -9.40 | $5.60 \times 10^7$ | MeCN | Peak shift analysis | 45 |
| CoCp(depe)[e] | 4-$CH_3$O-pyridinium | -12.76 | $3.20 \times 10^7$ | MeCN | Peak shift analysis | 45 |
| CoCp(depe)[e] | pyridinium | -15.08 | $3.50 \times 10^7$ | MeCN | Peak shift analysis | 45 |
| CoCp(depe)[e] | 4-$CH_3$-anilinium | -16.62 | $3.60 \times 10^7$ | MeCN | Peak shift analysis | 45 |
| CoCp(depe)[e] | 4-tBu-anilinium | -17.02 | $2.90 \times 10^7$ | MeCN | Peak shift analysis | 45 |
| CoCp(depe)[e] | 4-Cl-anilinium | -18.93 | $4.50 \times 10^7$ | MeCN | Peak shift analysis | 45 |
| CoCp(depe)[e] | 4-$CF_3$O-anilinium | -19.50 | $3.20 \times 10^7$ | MeCN | Peak shift analysis | 45 |
| CoCp(depe)[e] | 4-CN-anilinium | -22.61 | $1.50 \times 10^7$ | MeCN | Peak shift analysis | 45 |
| CoCp(dcpe)[e] | 4-Cl-phenol | 3.87 | $2.60 \times 10^2$ | MeCN | Peak shift analysis | 45 |
| CoCp(dcpe)[e] | acetic acid | 1.24 | $8.20 \times 10^3$ | MeCN | Peak shift analysis | 45 |
| CoCp(dcpe)[e] | 2,3,5,6-$F_4$-phenol | -3.38 | $8.20 \times 10^4$ | MeCN | Peak shift analysis | 45 |
| CoCp(dcpe)[e] | 2,3,4,5,6-pentaphenol | -3.39 | $1.10 \times 10^5$ | MeCN | Peak shift analysis | 45 |
| CoCp(dcpe)[e] | 2,3,5,6-$F_4$-4-$CF_3$-phenol | -8.14 | $1.30 \times 10^5$ | MeCN | Peak shift analysis | 45 |
| CoCp(dcpe)[e] | 4-$CH_3$O-pyridinium | -11.40 | $5.30 \times 10^4$ | MeCN | Peak shift analysis | 45 |
| CoCp(dcpe)[e] | pyridinium | -13.71 | $5.90 \times 10^4$ | MeCN | Peak shift analysis | 45 |
| CoCp(dcpe)[e] | 4-tBu-anilinium | -15.66 | $5.20 \times 10^4$ | MeCN | Peak shift analysis | 45 |
| CoCp(dcpe)[e] | anilinium | -16.32 | $4.90 \times 10^4$ | MeCN | Peak shift analysis | 45 |
| CoCp(dcpe)[e] | 4-Br-anilinium | -17.94 | $6.60 \times 10^4$ | MeCN | Peak shift analysis | 45 |
| CoCp(dppe)[e] | 4-Cl-phenol | 9.59 | $1.50 \times 10^2$ | MeCN | Peak shift analysis | 46 |
| CoCp(dppe)[e] | acetic acid | 6.96 | $3.20 \times 10^3$ | MeCN | Peak shift analysis | 46 |
| CoCp(dppe)[e] | benzoic acid | 4.24 | $1.50 \times 10^4$ | MeCN | Peak shift analysis | 46 |
| CoCp(dppe)[e] | 2,4,6-$Br_3$-phenol | 2.66 | $1.90 \times 10^4$ | MeCN | Peak shift analysis | 46 |
| CoCp(dppe)[e] | 2,3,5,6-$F_4$-phenol | 2.34 | $1.70 \times 10^5$ | MeCN | Peak shift analysis | 46 |
| CoCp(dppe)[e] | $F_5$-phenol | 2.33 | $2.30 \times 10^5$ | MeCN | Peak shift analysis | 46 |
| CoCp(dppe)[e] | salicylic acid | -2.32 | $2.30 \times 10^7$ | MeCN | Peak shift analysis | 46 |
| CoCp(dppe)[e] | 4-$CF_3$-2,3,5,6-$F_4$-phenol | -2.42 | $7.70 \times 10^6$ | MeCN | Peak shift analysis | 46 |
| CoCp(dppe)[e] | 2,4,6-trimethylpyridinium | -4.66 | $5.50 \times 10^3$ | MeCN | Peak shift analysis | 46 |
| CoCp(dppe)[e] | 4-OMe-pyridinium | -5.68 | $1.20 \times 10^7$ | MeCN | Peak shift analysis | 46 |
| CoCp(dppe)[e] | 2,6-lutidinium | -5.82 | $1.40 \times 10^4$ | MeCN | Peak shift analysis | 46 |
| CoCp(dppe)[e] | pyridinium | -7.99 | $2.70 \times 10^7$ | MeCN | Peak shift analysis | 46 |
| CoCp(dppe)[e] | 4-OMe-anilinium | -8.91 | $1.90 \times 10^7$ | MeCN | Peak shift analysis | 46 |
| CoCp(dppe)[e] | N,N-dimethylanilinium | -9.49 | $8.30 \times 10^4$ | MeCN | Peak shift analysis | 46 |
| CoCp(dppe)[e] | 4-methylanilinium | -9.53 | $1.70 \times 10^7$ | MeCN | Peak shift analysis | 46 |
| CoCp(dppe)[e] | 4-tBu-anilinium | -9.94 | $2.10 \times 10^7$ | MeCN | Peak shift analysis | 46 |
| CoCp(dppe)[e] | 4-Cl-anilinium | -11.85 | $2.40 \times 10^7$ | MeCN | Peak shift analysis | 46 |
| CoCp(dppe)[e] | 4-Br-anilinium | -12.22 | $2.50 \times 10^7$ | MeCN | Peak shift analysis | 46 |
| CoCp(dppe)[e] | p-toluenesulfonic acid | -13.35 | $1.80 \times 10^7$ | MeCN | Peak shift analysis | 46 |
| CoCp(dppe)[e] | 4-$CF_3$-anilinium | -14.12 | $1.70 \times 10^7$ | MeCN | Peak shift analysis | 46 |
| CoCp(dppe)[e] | 4-CN-anilinium | -15.53 | $1.70 \times 10^7$ | MeCN | Peak shift analysis | 46 |
| CoCp(dppe)[e] | DMF($H^+$) | -16.75 | $1.10 \times 10^7$ | MeCN | Peak shift analysis | 46 |
| *Multimetallic Systems* | | | | | | |
| [FeFe($\mu$-adt)$(CO)_4(PMe_3)_2$][f] | HCl | -6.40 | $2.20 \times 10^0$ | MeCN | Time-resolved IR | 151 |
| [FeFe($\mu$-Hadt)$(CO)_4(PMe_3)_2$][+g] | Triflic acid | -7.35 | $1.50 \times 10^{-1}$ | MeCN | Time-resolved IR | 151 |
| [FeFe($\mu$-Hadt)$(CO)_4(PMe_3)_2$][+g] | HBr | -3.54 | $>1 \times 10^2$ | MeCN | Time-resolved IR | 151 |
| $Fe_2$(pdt)$(CO)_4(PMe_3)_2$[h] | [$HBF_4 \bullet Et2O$] | - | $7.97 \times 10^2$ | MeCN | Stopped-flow UV-vis and IR | 152 |
| $Fe_2$(edt)$(CO)_4(PMe_3)_2$[i,j] | [$HBF_4 \bullet Et2O$] | - | $8.37 \times 10^1$ | MeCN | Stopped-flow UV-vis and IR | 152 |

**Journal Name**                             **ARTICLE**

| | | | | | | |
|---|---|---|---|---|---|---|
| $Fe_2(pdt)(CO)4(PMe_3)(CN)^{h,k}$ | [HBF$_4$•Et2O] | - | $>8 \times 10^5$ | MeCN | Stopped-flow UV-vis and IR | 152 |
| $Fe_2(edt)(CO)4(PMe_3)(CN)^{i,k}$ | [HBF$_4$•Et2O] | - | $>8 \times 10^5$ | MeCN | Stopped-flow UV-vis and IR | 152 |
| $[Fe_2(pdt)(CO)_4(PMe_3)(HCN)]^{+h,l}$ | -$^a$ | - | $2.7 \times 10^{-3b}$ | MeCN | Stopped-flow UV-vis and IR | 152 |
| $Fe_2(pdt)(CO)_4(CN)_2$ $^{h,k}$ | [HBF$_4$•Et2O] | - | $>8 \times 10^5$ | MeCN | Stopped-flow UV-vis and IR | 152 |
| $Fe_2(edt)(CO)_4(CN)_2$ $^{i,k}$ | [HBF$_4$•Et2O] | - | $>8 \times 10^5$ | MeCN | Stopped-flow UV-vis and IR | 152 |
| $[Fe_2(pdt)(CO)_4(CN)(HCN)]^{+\,h,l}$ | -$^a$ | - | $8.0 \times 10^{-3b}$ | MeCN | Stopped-flow UV-vis and IR | 152 |
| $[Fe_2(edt)(CO)_4(CN)(HCN)]^{+i,l}$ | -$^a$ | - | $9.0 \times 10^{-3b}$ | MeCN | Stopped-flow UV-vis and IR | 152 |
| $Fe_2(edt)(CO)_5(PMe_3)^i$ | [HBF$_4$•Et2O] | - | $3.70 \times 10^{-3}$ | MeCN | Stopped-flow IR | 153 |
| $Fe_2(pdt)(CO)_5(PMe_3)^h$ | [HBF$_4$•Et2O] | - | $2.84 \times 10^{-2}$ | MeCN | Stopped-flow IR | 153 |
| $Fe_2(MeSCH_2C(Me)(CH_2 S)_2)(CO)_5^j$ | [HBF$_4$•Et2O] | - | $5.70 \times 10^{-2}$ | MeCN | Stopped-flow IR | 153 |
| $Fe_2(PhS_2)(CO)_4(PMe_3)_2$ | [HBF$_4$•Et2O] | - | $9.30 \times 10^0$ | MeCN | Stopped-flow IR | 153 |
| $Fe_2(MeSCH_2C(Me)(CH_2 S)_2)(CO)_4(PMe_3)$ | [HBF$_4$•Et2O] | - | $4.70 \times 10^1$ | MeCN | Stopped-flow UV-vis | 153 |
| $Fe_2(edt)(CO)_4(PMe_3)_2^i$ | [HBF$_4$•Et2O] | - | $8.37 \times 10^1$ | MeCN | Stopped-flow UV-vis | 153 |
| $Fe_2(odt)(CO)_4(PMe_3)_2^m$ | [HBF$_4$•Et2O] | - | $1.02 \times 10^2$ | MeCN | Stopped-flow UV-vis | 153 |
| $Fe_2(Me\text{-}pdt)(CO)4(PMe_3)_2^n$ | [HBF$_4$•Et2O] | - | $1.04 \times 10^3$ | MeCN | Stopped-flow UV-vis | 153 |
| $Fe_2(iPr\text{-}pdt)(CO)4(PMe_3)_2^o$ | [HBF$_4$•Et2O] | - | $1.19 \times 10^3$ | MeCN | Stopped-flow UV-vis | 153 |
| $Fe_2(Me_2\text{-}pdt)(CO)_4(PMe_3)_2^p$ | [HBF$_4$•Et2O] | - | $2.48 \times 10^3$ | MeCN | Stopped-flow UV-vis | 153 |
| $Fe_2(iPr_2\text{-}pdt)(CO)_4(PMe_3)_2^q$ | [HBF$_4$•Et2O] | - | $4.30 \times 10^3$ | MeCN | Stopped-flow UV-vis | 153 |
| $Fe_2(pdt)(CO)2(PMe_3)_4^h$ | [HBF$_4$•Et2O] | - | $>8E \times 10^5$ | MeCN | Stopped-flow UV-vis | 153 |
| $[FeFe(\mu\text{-}pdt)(CO)_6]^{-h}$ | toluenesulfonic acid | - | $7.00 \times 10^7$ | MeCN | Time-resolved IR and UV-vis | 154 |
| $[FeFe(\mu\text{-}pdt)(CO)_6]^{-h}$ | trichloroacetic acid | - | $1.30 \times 10^7$ | MeCN | Time-resolved IR and UV-vis | 154 |
| $[FeFe(\mu\text{-}pdt)(CO)_6]^{-h}$ | dichloroacetic acid | - | $7.00 \times 10^5$ | MeCN | Time-resolved IR and UV-vis | 154 |
| $[Co_{13}C_2(CO)_{24}]^{4-}$ | anilinium BF4 | - | $2.30 \times 10^9$ | MeCN | Catalytic current | 158 |
| $[Co_{13}C_2(CO)_{24}]^{4-}$ | anilinium BF4 | - | $1.60 \times 10^9$ | MeCN | FOWA | 158 |
| $[Co_{11}C_2(CO)_{23}]^{3-}$ | p-OMe-anilinium BF4 | - | $3.00 \times 10^8$ | MeCN | Catlytic current | 159 |
| $[Fe_4N(CO)_{11}L]^-$ (L = Ph2P(o-N,N-dimethylC6H4NMe2)) | $H_2O$ | - | $0.9 \pm 0.4$ (under $N_2$) and $3 \pm 1.5$ (under $CO_2$) | MeCN:H$_2$O (99:1) | Peak shift analysis | 103 |
| $[Fe_4N(CO)_{11}L]^-$ (L = Ph$_2$P(o-C$_5$H$_4$N)) | $H_2O$ and $H_2CO_3$ | - | $8.7 \pm 2.9$ (under $N_2$) and $6.1 \pm 0.8$ (under $CO_2$) | MeCN:H$_2$O (99:1) | Peak shift analysis | 103 |

$^a$Proton source is intramolecular ligand-protonated species, $^b$Units for $k_{PT}$ in s$^{-1}$, $^c$N protonation, $^d$S protonation $^e$Cp ring protonation, $^f$adt = *N*-benzyl-azadithiolate, $^g$Hadt = protonated *N*-benzyl-azadithiolate, $^h$pdt = propanedithiolate, $^i$edt = ethanedithiolate, $^j$performed at 21°C, $^k$CN protonation $^l$tautomerization, $^m$odt = 2-oxapropane-1,3-dithiolate, $^n$Me-pdt = methylated propanedithiolate, $^o$iPr-pdt = Isopropylated propanedithiolate, $^p$Me2-pdt = dimethylated propanedithiolate, $^q$iPr2-pdt = diisopropylated propanedithiolate
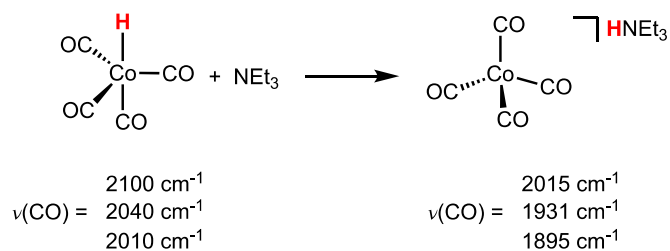
**ARTICLE**

**Figure 2.** Deprotonation of $HCo(CO)_4$ (trigonal bipyramidal) by $NEt_3$ to form $[HNEt_3][Co(CO)_4]$ (tetrahedral). The carbonyl stretching frequencies for the transition metal hydride complex and its conjugate base showcase electronic rearrangement upon deprotonation.

The hypothesis that electronic and structural rearrangement impacts proton transfer kinetics is further supported by the sluggish rate constants observed to deprotonate multimetallic clusters containing bridging hydride ligands. Often, bridging hydrides are thermodynamically more acidic than their monometallic transition metal hydride analogs, yet they exhibit slower proton transfer kinetics. Specifically, Norton and coworkers reported a series of deprotonation rate constants of $[Rh_{13}(CO)_{24}H_3]^{2-}$ by various substituted anilines, which include the extraordinarily slow rate constant of $1.42 \times 10^{-3}$ $M^{-1}$ $s^{-1}$ for $p$-toluidine, even though the deprotonation of $[Rh_{13}(CO)_{24}H_3]^{2-}$ by $p$-toluidine is a slightly exergonic reaction.[15] The high kinetic barrier to remove an interstitial proton was attributed to the structural and electronic rearrangement that occurs, including the decrease in average Rh-Rh bond distances upon deprotonation. However, the observed slow proton transfer kinetics may only be inherent to interstitial hydrides as we will demonstrate later in **Part II – Measuring proton transfer kinetics in multimetallic hydride systems** that several multimetallic species can exhibit sufficiently fast kinetics in the context of catalysis.

Theoretical studies also support the effects of electronic and structural rearrangement on proton transfer kinetics. Proton transfer reactions can be classified as either nonadiabatic and adiabatic based on the overlap of the localized reactant and product proton vibrational wave functions (Figure 3).[16–18] At large distances between proton exchanging centers ($Q$), the zero-point energy lies below the large proton barrier and proton transfer occurs via quantum nonadiabatic tunneling (Figure 3a). In the adiabatic regime where Q is small, the proton barrier is low enough such that one or both of the proton vibrational states lie above the barrier in the proton coordinate (Figure 3b). Therefore, proton transfer reactions can be treated by using an adiabatic[18–20] or a nonadiabatic[21–25] model based on the degree of vibrionic proton coupling, although more recent models including quantum mechanical effects have been shown to be applicable to both mechanistic regimes.[26–33] A comprehensive account of all computational methods is beyond the scope of this review, though we present a few relevant examples that rationalize and demonstrate correlations with experimental intrinsic barriers for proton transfer of metal hydride complexes and organic acids.
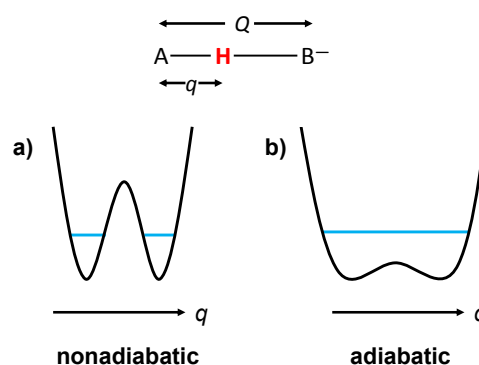


**Figure 3.** Proton potential energy vs $q$ (A—H distance) profiles for an A—B nuclear separation $Q$: (a) at large Q, proton transfer involves tunneling in the nonadiabatic regime and (b) at small Q, the PT occurs in the adiabatic regime as the proton barrier is lower than the zero-point energy of the system (blue line).

Agreement between experimental observations and computational predictions of proton transfer rate constants has been shown based on changes in coordination geometry and spatial separations between the proton-exchanging metal centers. Due to the lack of strong M—H----M⁻ hydrogen-bonding interaction,[34] Creutz and Sutin[24] used a nonadiabatic model to predict proton transfer kinetics of the $HM(Cp)(CO)_3/M(Cp)(CO)_3^-$ (M = Cr, Mo, and W) and $H_2M(CO)_4/HM(CO)_4^-$ (M = Fe and Os) self-exchange reactions, for which $\Delta G_{PT} = 0$. This model describes classical activation barriers to proton transfer as a function of angular nuclear configuration changes of ancillary ligands, which arise from influencing the probability of the "correct" orientation of metal hydride and its conjugate base in order for proton transfer to occur. In particular, the authors found that proton transfer kinetics of the $HM(Cp)(CO)_3/M(Cp)(CO)_3^-$ self-exchange reactions is relatively faster than those of the $H_2M(CO)_4/HM(CO)_4^-$ reactions, consistent with experimental observations by Norton and coworkers.[35,36] These results are attributed to the large geometric changes between the octahedral $H_2M(CO)_4$ and trigonal bipyramidal $HM(CO)_4^-$ complexes upon proton transfer (Scheme 1a), whereas only minimal structural changes in OC—M—CO bond angles (<10⁰) occur in the $HM(Cp)(CO)_3/M(Cp)(CO)_3^-$ system. Interestingly, incorporation of a pre-equilibrium interconversion of the equatorial and axial CO ligands of $HM(CO)_4^-$ *via* a Berry pseudorotation mechanism to approach a species more closely resembling the hydride (i.e., square pyramidal isomer) decreases the estimated proton transfer rates, such that they are closer to the experimental values (Scheme 1b).

**Scheme 1.** Large geometric changes upon proton transfer of $H_2M(CO)_4/HM(CO)_4^-$ complexes
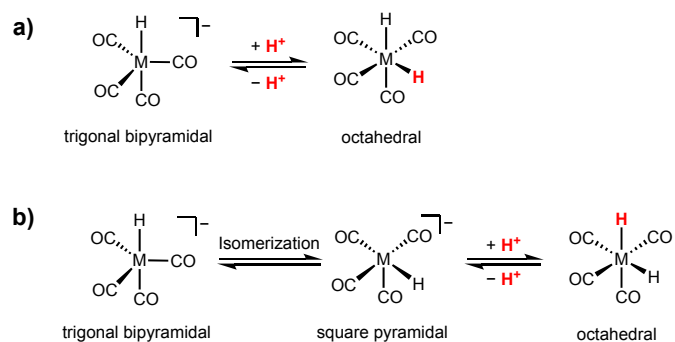


As noted above, proton transfer reactions of metal hydride complexes more closely resemble proton transfer reactions involving C-H bonds than O-H or N-H bonds. Thus, insight from studies investigating C-H bonds also provide a valuable perspective on this chemistry. Using quantum chemical calculations by accounting for the quantum character of proton transfer, Costentin and Savéant[37] observed a similar nonadiabatic character for proton transfer reactions between carbon-based acids and their conjugate bases, which explains their sluggish kinetics as opposed to proton transfer at oxygen and nitrogen. An analysis of the $CH_4/CH_3^-$,self-exchange reaction reveals a significantly lower rate constant (by almost 7 orders of magnitude) than those of the $NH_4^+/NH_3$, and $H_2O/OH^-$ reactions. The slower proton transfer kinetics of the $CH_4/CH_3^-$ reaction was attributed to the greater distance between the carbon centers in the transition state ($Q$) than between the nitrogen and oxygen atoms. This large separation arises from the less polar character of C—H bond as compared to that of the N—H and O—H bonds and thereby introduces a larger intrinsic barrier for proton transfer (Figure 4). Gronert also noted the smaller polarization of the C—H bond of $CH_4$ that results in a weaker interaction of the $CH_4/CH_3^-$ complex with a transition state energy of 9.3 kcal/mol vs −10.5 and −28 kcal/mol for the $NH_3/NH_2^-$ and $H_2O/OH^-$ complexes, respectively.[38] Notably, the increase in polarity of the C—H bond caused by the presence of an electron-withdrawing substituent (*e.g.*, $NO_2$ group) helps lower the proton transfer barrier though not sufficient to achieve adiabatic conditions as in $NH_3$ and $H_2O$. Pearson and coworkers also observed that the magnitude of rate constant for the deprotonation of carbon-based acids are closely matched deprotonation rates of transition metal hydrides with comparable thermodynamic driving forces, due to the similarly large electronic and structural rearrangement during proton transfer.[39] More recently, Sampaio et al. observed that the deprotonation of the C-H bond in oxidized benzimidazole hydride donors using N-base acids were well below the diffusion limit even for thermoneutral acid-base reactions.[40]
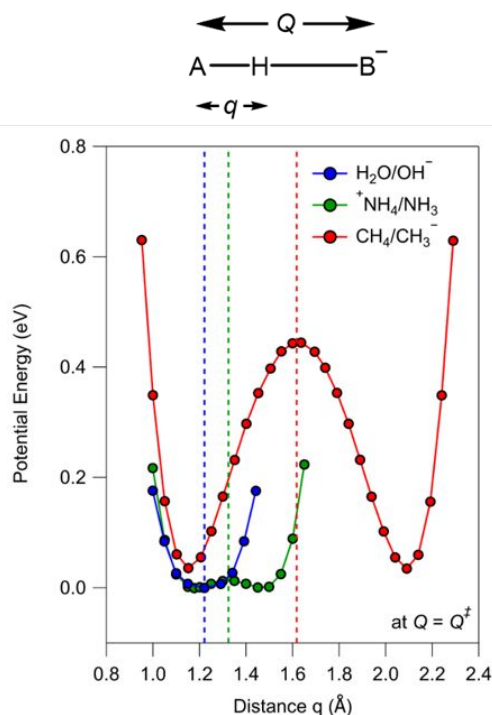


**Figure 4.** Potential energy vs $q$ (A—H distance) profiles at $Q = Q^{\ddagger}$ (A—B distance at the transition state) where A and B represent proton exchanging centers. Comparison between a carbon acid, $CH_4$, and two Eigen acids, $NH_3$ and $H_2O$. Adapted with permission from Costentin, C.; Savéant, J.-M. Why Are Proton Transfers at Carbon Slow? Self-Exchange Reactions. *J. Am. Chem. Soc.* **2004**, *126* (45), 14787–14795. Copyright 2004 American Chemical Society.

Together, the intrinsic barriers to metal-based proton transfer arise from the large geometric and electronic rearrangement associated with the reactions. (Figure 5). Even when the thermodynamic driving force is sufficiently exergonic, proton transfer to and from the metal center is often limited by these parameters, leading to slow proton transfer reactions. Table 1 includes a number of cases where the proton transfer rate constant is well below the diffusion limit when $\Delta G_{PT} < 0$ kcal/mol. Given the importance of proton transfer in fuel-forming catalysis, it is important for researchers to rationally design novel catalysts that exhibit minimal electronic and structural rearrangement for the proton transfer reaction, with the goal of increasing catalyst efficiency. Part II will discuss how these intrinsic barriers and their kinetic impact affect fuel-forming reactions, including effects on selectivity, mechanism, efficiency, and more.
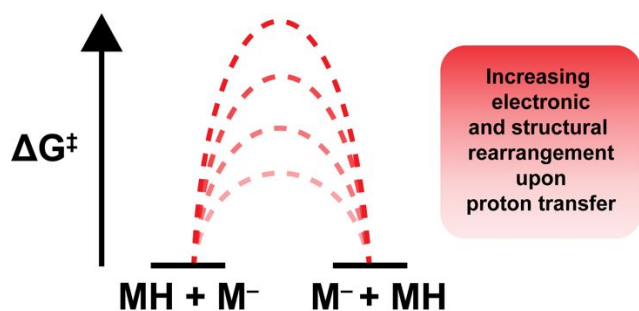
**ARTICLE**                                                                 **Journal Name**



**Figure 5.** Reaction coordinate diagram for the self-exchange reaction of different transition metal hydride complexes and their respective conjugate bases. The larger intrinsic barrier suggests larger electronic and structural rearrangement upon proton transfer

**Effects of Sterics on Proton Transfer Kinetics**

Sterically encumbered transition states for metal-based proton transfer are also known to exhibit slow kinetics. However, this concept is not intrinsic to transition metal hydrides as steric effects have been shown for oxygen and nitrogen-based proton transfer reactions as well. For instance, the Proton Sponge, 1,8-bis(dimethylamino)naphthalene, has a proton transfer rate constant far below the diffusion limit when using water as a proton source at a value of $2 \times 10^5$ M$^{-1}$ s$^{-1}$. The proton is placed in a strong hydrogen bond, but the N,N-dimethyl groups also make removal of the proton sterically inaccessible, where the congested transition state manifest in the slow proton transfer kinetics. In this section, we will provide experimental case studies to show how sterics manifest in observed proton transfer rate constants for reactions involving transition metal hydrides as well as discuss theoretical justifications for these steric arguments.

There are multiple examples of sterically encumbered transition metal hydrides that exhibit rather slow proton transfer rate constants (Table 1). Caulton and coworkers monitored the $^1$H and $^{31}$P NMR spectra of combinations of Cr(tripod)$_2$ (tripod = MeC(CH$_2$PMe$_2$)$_3$) and its conjugate acid [HCr(tripod)$_2$]$^+$. No line broadening or coalescence of the two resonances were observed, signaling that the intermolecular proton transfer rate constant must be less than 10 s$^{-1}$, if it occurs at all.[41] The authors suggest that intermolecular proton exchange was not observed because the steric bulk on the phosphine ligands led to a congested transition state and slow proton transfer.

In another example of the effects of sterics on transition metal hydride proton transfer reactions, Darensbourg et al. demonstrated that HMo(CO)$_2$(dxpe)$_2$ (dxpe = 1,2-bis(di-x-phosphino)ethane, where x = phenyl, methyl, or ethyl) complexes were deprotonated with rate constants far lower than would be predicted by thermodynamic arguments alone.[42] Interestingly, the rate of deprotonation of the hydride complexes by a number of amine bases was greatly enhanced when small anionic catalysts were added to solution (I$^-$, Br$^-$, Cl$^-$, F$^-$, acetate). The authors proposed a mechanism in which the two bulky bisphosphine ligands prevented facile approach of the amine base but allowed for small anionic "proton shuttles"

to approach the hydride ligand more easily and catalytically transfer the proton to the more thermodynamically stable amine base. The authors also found a complex relationship between deprotonation rate constants and phosphine substituents that arises from a combination of steric and electronic effects.[43]

In another case, Norton and coworkers described the thermodynamic and kinetic acidity of the polyhydride complex, [H$_4$Re(PMe$_2$Ph)$_4$]$^+$.[44] The proton transfer kinetics of the reaction between [H$_4$Re(PMe$_2$Ph)$_4$]$^+$ and aniline were monitored using NMR spectroscopy. This complex is deprotonated more than 5 orders of magnitude slower than predictions based on thermodynamic arguments. In this case, there is relatively little structural rearrangement between the transition metal hydride and its conjugate base. Instead, the dominant factors limiting proton transfer are steric effects. The ligand substituents yield a congested transition metal hydride which prevents facile approach of the aniline base, leading to the dramatically low rate constant for deprotonation.

Our group has also observed correlations between proton transfer rate constant and the steric bulk of transition metal hydride complex for a series of [CoCp(dxpe)(NCCH$_3$)]$^{2+}$ (Cp = cyclopentadienyl, dxpe = 1,2-bis(di-X-phosphino)ethane) complexes.[45] The proton transfer rate constants were determined using cyclic voltammetry peak shift analysis. When using depe (1,2-bis(diethylphosphino)ethane) and dcpe (1,2-bis(dicyclohexylphosphino)ethane) as the chelating diphosphine ligands, the ethyl derivative exhibited faster kinetics (max $k_{PT}$ = 3.5 x 10$^7$ M$^{-1}$ s$^{-1}$) than the ethyl derivative (maximum $k_{PT}$ = 7.1 x 10$^4$ M$^{-1}$ s$^{-1}$) under equivalent exergonic reaction conditions. By systematically varying the dxpe ligand in the cobalt complex, we showed that the three order of magnitude difference between these two $k_{PT}$ values is associated with the steric bulk of the diphosphine ligand substituents.

Although the examples highlighted thus far showcase the dramatic decrease in rate constants for sterically encumbered transition metal hydride complexes, sterics can also be utilized to stabilize transition metal hydride intermediates. For example, Gray and coworkers studied cobalt complexes containing the triphos ligand (1,1,1-tris(diphenylphosphinomethyl)ethane) for cobalt-catalyzed hydrogen evolution. The steric bulk on the triphos ligand helps stabilize and generate a transient hydride intermediate for chemical characterization. This is especially advantageous because it allowed the researchers to probe the mechanism for the remaining steps in the catalytic cycle. The kinetics of proton transfer for this system will be discussed more in depth with respect to the hydrogen evolution reaction (HER) in Part II.

In addition to steric effects of the transition metal hydride complexes themselves, the sterics of the organic acids/bases used can also impact proton transfer kinetics. Our group studied the proton transfer kinetics between CoCp(dppe) (dppe = 1,2-bis(diphenylphosphino)ethane) and a variety of exogenous acids, primarily based on anilinium and pyridinium salts.[46] When non-sterically hindered acids were used, a linear free energy Brønsted relationship was observed. Similarly, a LFER was

observed by Norton and coworkers, where they also treated a series of different metal carbonyl hydride complexes with the same exogeneous base to develop a kinetic acidity series.[36] However, in our study of CoCp(dppe), the proton transfer rate constants fell far below the predicted LFER when obtrusive substituents were introduced onto the acid (Figure 6). For example, the proton transfer rate constants when using 4-methylanilinium and N,N-dimethylanilinium were two orders of magnitude apart, despite a 0.03 p$K_a$ difference between the two acids, suggesting the kinetics are impeded by steric interactions between the reactants. To this point, we emphasize that when performing systematic studies to vary the driving force for a reaction, sterically encumbered acids and bases should be avoided.
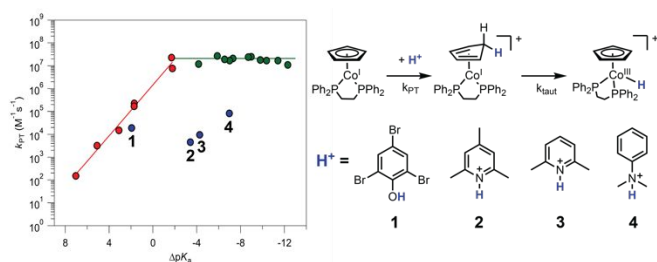


**Figure 6.** Brønsted plot for the apparent proton transfer rate constant of Co(I) species using bulky acids (blue) and nonbulky acids (red and green). Bulky acids have been drawn to showcase steric congestion.

Creutz and Sutin also used the nonadiabatic model to understand steric effects on proton transfer kinetics.[24] In addition to geometric arrangement, the proton transfer rate constants were found to rapidly decrease with reactant separation, which suggests that the factors preventing close approach of M-H/M⁻ can directly influence the kinetics of proton exchange. Experimental measurements of proton transfer rate constants, wherein bulky substituents surrounding the hydrides[42–44,47] and organic acids[46] provide steric constraints on proton transfer reactions, reveal slow proton transfer kinetics, as predicted by this theory

In summary, sterics associated with the transition metal complex and the exogenous organic acids and bases can lead to slower proton transfer kinetics than anticipated based on thermodynamics and Brønsted linear free energy relationships. Multiple examples can be found in Table 1. By understanding what causes slow proton transfer kinetics in transition metal hydride complexes, researchers can systematically design new catalysts in order to minimize steric congestion with the goal of increasing catalyst efficiency. Nevertheless, sterics can also be utilized to control reactivity patterns or stabilize metal hydride intermediates. In Part II, we will expand on how sterics and their kinetic impact manifest in fuel-forming reactions including effects on selectivity, mechanism, efficiency, and more.

### Establishing Standard Conditions for Determining Kinetic Acidity

To the best of our knowledge, Norton and coworkers were the first to directly discuss the concept of kinetic acidity.[35,36,48] Their 1982 report on the deprotonation rate constants for a series of transition metal carbonyl hydride complexes emphasized the need for systematic investigation of kinetic acidity under *standard conditions*.[35] To this point, there are multiple factors that should be considered for kinetic acidity measurements, including mechanistic studies, the solvent choice and thermodynamic driving force.

First, it is crucial to have mechanistic evidence for a proton transfer reaction before performing kinetic acidity measurements. Pivotal evidence includes kinetic isotope effects (KIEs), and readers can find a thorough report by Bullock on isotope effects in reactions of transition metal hydrides.[49] In short, theoretical treatment of a proton transfer self-exchange reaction predicts that the KIE should be largest for a thermoneutral reaction with a symmetric transition state. As driving force deviates from thermoneutrality (endergonic or exergonic), then the KIE should decrease. It is common to observe lower isotope effects for geometrically constrained complexes, since the steric constraints will affect the linearity of the transition state.[50] If extremely large KIE values are observed, then tunneling may be involved, and researchers are encouraged to perform temperature dependent KIE studies for further evidence.

Factors such as solubility and stability of reactants and products, self-ionization constants, and previously established thermodynamic parameters should be considered when choosing a solvent for these measurements. Acetonitrile is a popular candidate for kinetic acidity measurements because it can solubilize a wide variety of transition metal hydride complexes and effectively solvate cations to reduce ion-pair formation.[51] Additionally, acetonitrile has a low self-ionization constant, so it can suit a wide range of acid and base strengths.[51] Finally, there are well-established thermodynamic acid/base parameters for organic compounds in acetonitrile which facilitate identification of Δp$K_a$ and hence Δ$G_{PT}$ values.[52,53]

The thermodynamic driving force is generally described using either Δ$G_{PT}$ or Δp$K_a$, where Δp$K_a$ is the difference between the p$K_a$ of the transition metal hydride and the conjugate acid of the proton acceptor. Brønsted and Pederson showed that Δp$K_a$ has a profound and expected effect on the kinetics of proton transfer; a larger driving force should typically result in a faster reaction. Specifically, they discuss this reactivity in terms of the rate equilibrium correlation, described by equation 7, where the log of the rate constant varies as a function of the log of the equilibrium constant at constant temperature.[54] A typical Brønsted plot for proton transfer reactions involving transition metal hydride complexes has a linear free energy relationship (LFER) at endergonic or slightly exergonic reaction conditions, but as the driving force increases, the values may plateau at the diffusion limit (Figure 7).[55,56]

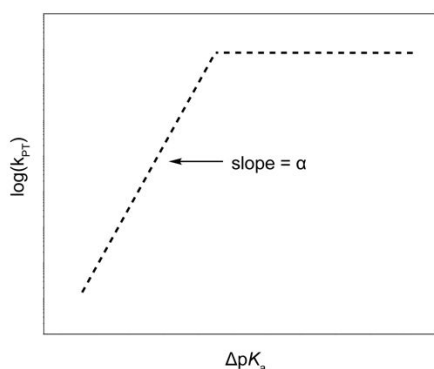$$\log (k_1) = \alpha\, log(K_{eq}) + C \tag{7}$$

**Figure 7.** Typical Brønsted plot for proton transfer reactions involving transition metal hydride complexes and structurally similar organic bases

Since $\Delta pK_a$ has such a large effect on the kinetics of proton transfer, the proton acceptor/donor choice for $k_{PT}$ measurements should be chosen carefully based on the technique used to monitor kinetic acidity, which will be further described in **Part I – Techniques to Monitor Kinetic Acidity**. For example, if the reaction is too endergonic or exergonic, then the kinetics may be too slow or too fast, respectively, to be able to extract meaningful information using the chosen technique.

Although the driving force for the proton transfer reactions to and from metal hydride complexes has a large influence on the observed proton transfer rate constants, the intrinsic barriers involving the electronic and structural rearrangement upon (de)protonation also significantly contribute to the observed slow proton transfer kinetics. Therefore, it is valuable to quantify the intrinsic barrier for proton transfer ($\Delta G^{\ddagger}_0$), which is $\Delta G^{\ddagger}$ when $\Delta G_{PT} = 0$.[57] Norton and coworkers have used self-exchange reactions to quantify $\Delta G^{\ddagger}_0$ for a number of isolable transition metal hydride complexes.[36] Additionally, for scenarios where $\Delta G_{PT} \neq 0$, Brønsted relationships can be used to determine $\Delta G^{\ddagger}_0$. This is done by varying $\Delta G_{PT}$ systematically through reactions of the transition metal hydride complex with structurally similar bases that have different $pK_a$ values (or conversely, through reactions of the transition metal complex with structurally similar acids with different $pK_a$ values). The $\Delta G_{PT}$ is related to $\Delta pK_a$ using equation 8. The slope of the LFER between $\log(k_{PT})$ and $\Delta pK_a$ is the Brønsted coefficient, $\alpha$, which can be used to extrapolate the value for $\Delta G^{\ddagger}_0$ using equation 9.[58,59] For systems with larger intrinsic barriers, $\alpha$ will vary slowly with $\Delta G_{PT}$ (Eqn 10)[54]. Marcus theory predicts that $\alpha$ should decrease toward 0.5 as $\Delta G_{PT}$ approaches zero, specifically, as the MH $pK_a$ decreases toward the conjugate acid $pK_a$.[57,58]

$$\Delta G_{PT} = 2.3RT(\Delta pK_a) \tag{8}$$

$$\alpha = \frac{1}{2} \cdot \frac{(1 + \Delta G_{PT})}{4\Delta G^{\ddagger}_0} \tag{9}$$

$$\frac{d\alpha}{d\Delta G_{PT}} = \frac{1}{8\Delta G^{\ddagger}_0} \tag{10}$$

Clearly, it is important to accurately quantify the proton transfer driving force, $\Delta G_{PT}$, in order to reliably compare proton transfer rate constants across multiple systems since $\Delta G_{PT}$

influences proton transfer rate constants (Brønsted relationship). Additionally, it will become more apparent in Part II that thermodynamics can have a large influence on the observed kinetics for fuel-forming reactions. Quantification of the metal hydride $pK_a$ value better informs the choice of acid for catalysis, as well as facilitates kinetic comparison with other reported fuel-forming catalysts. Therefore, we encourage readers to take advantage of the vast reports on the thermodynamic acidity of transition metal hydride complexes, as well as the well-established thermodynamic acid/base parameters for organic compounds in acetonitrile in order to understand how to quantify $\Delta pK_a$ values.

**Techniques to Monitor Kinetic Acidity**

There are a variety of techniques used for monitoring proton transfer reactions, and the choice of technique depends on many factors: the availability of spectroscopic handles, the rate of the chemical reaction, and the physical properties and stability of the reactants/intermediates/products. In this section, the discussion will focus on the various techniques that have been used to monitor proton transfer kinetics involving metal hydrides as reactants, intermediates, and products. A brief discussion will focus on what the technique specifically monitors, the time resolution of the technique, considerations that are important for experimental design to study kinetics, and limitations or pitfalls within specific techniques. Various NMR methods, stopped-flow rapid mixing techniques, electrochemical techniques, and transient absorption spectroscopic methods have been successfully used to study proton transfer reactions. Table 2, summarizes the discussed techniques, time resolution, and identifiable chemical traits.

**Table 2.** Reaction timescale and chemical handles for common techniques used to measure kinetics of proton transfer reactions[11,35,60–63]

| Technique | Timescale | Chemical Handle |
|---|---|---|
| $^1$H NMR | ms – s | Proton Chemical Shifts (ppm) |
| $^{31}$P NMR | ms – s | Phosphorous Chemical Shifts (ppm) |
| Stopped-flow UV-Vis | ms – mins | UV and Visible absorption features |
| Stopped-flow IR | ms – mins | Infrared active vibrations |
| Cyclic Voltammetry | ⊠s – secs | Redox events coupled to PT processes |
| Nanosecond Transient Absorption Spectroscopy | ns - ms | UV and Visible absorption features |

**Nuclear Magnetic Resonance (NMR) Spectroscopy** In general, NMR spectroscopy has been the most used method to

**Journal Name**

**ARTICLE**

analyze metal hydride species and their reactivity.[35,63–65] NMR spectroscopy surveys specific NMR-active nuclei and their associated chemical environment, and this technique is often used to compliment UV-Vis absorption and IR spectroscopy studies.

NMR spectroscopy can be used to monitor proton transfer exchange reactions that are under equilibrium. When designing an experiment around proton exchange, one should be aware of the following: 1) the nuclei you are observing, 2) the accessible ligand spectroscopy handles, and 3) the magnetic moment of your analyte (paramagnetic vs diamagnetic). $^1$H NMR allows both the ligand scaffold and the M-H proton itself to be probed, and both can often be used to quantify kinetics of a proton transfer reaction. While the chemical shift (in ppm) of the hydride proton varies greatly from complex to complex, in general metal-hydride protons are drastically up field versus metalated ligands or organic molecules, with most exceptions coming from $d^0$ and $d^{10}$ complexes.[63,66,67]

In a common NMR spectroscopy experiment to measure the kinetics of an exchange reaction, a metal hydride or metal complex and the corresponding base or acid known to undergo intermolecular proton transfer are chosen so that the driving force is relatively low ($\Delta G_{PT} \leq$ ~2 kcal/mol)[11] such that the reactants and products are in equilibrium. In this limit, proton exchange between a transition metal hydride complex and a base is observed by line broadening. Line broadening occurs when exchange is relatively rapid, causing sharp peaks of isolated reactants and products to "broaden".[63] Rate constants for proton transfer can be extrapolated from the difference between the original proton signature's FWHM (full width half maximum) and the FWHM observed for the same proton when undergoing equilibrium exchange with a proton acceptor. Equation 11 describes this relationship:[68]

$$W_a = \frac{1}{\pi}\left(k_A + \frac{1}{T_{2A}}\right); k_A = \pi(\Delta W) \qquad (11)$$

where $W_a$ is the width after equilibrium, $k_A$ is the rate of exchange from the reactants, $\Delta W$ is the change in the width from the control vs the peak broadening caused by exchange, and $T_{2A}$ is the relaxation time for the experiment.

Generally, the time resolution for 1D NMR experiments ranges from the milliseconds to seconds depending on the ability to optimize pulse and relaxation times, and temperatures.[11,70,71] In addition to 1D NMR techniques (e.g. $^1$H NMR), equilibria can also be probed using 2D NMR techniques, such as EXSY (EXchange SpectroscopY), to monitor the exchange of the spin active nuclei (including, but not limited to protons). EXSY can directly monitor two distinct molecules and the nuclei that exchange in a conformation change or chemical reaction, in this case a proton is monitored as the exchanged nuclei. Direct rates can be extrapolated with EXSY using Equation 12:

$$T_{m(opt)} = \frac{1}{k}ln\frac{R_1 + k}{R_1} \qquad (12)$$

where $T_m$ is the optimal mixing time, $R_1$ is a characteristic precision constant, and the desired rate of exchange k. If the $T_m$

is not optimized or the chemical exchange is too rapid in comparison ($R_1$ > ~ 10 ms), extrapolated rates can be unreliable.[58]

When NMR spectroscopy is used to analyze reaction kinetics, systems should be tailored to establish observable chemical equilibria and to operate in timescales that line broadening or chemical exchange with 1D and EXSY can be observed, respectively. Variable temperature (VT) NMR spectroscopy can be used to speed up or slow down reactions to allow line broadening to occur.

**Stopped-flow Rapid** Mixing In contrast to NMR spectroscopy that surveys systems in equilibrium, stopped-flow usually analyzes transient, irreversible reactions. Stopped-flow rapid mixing is a methodology that mixes two (or three) solutions of reactants and uses coupled optical monitoring to monitor the solution. Using known optical spectra of reactants, intermediates, and products, chemical reactivity can be studied. In standard stopped-flow setups there are two components, 1) a mixing apparatus where two or more syringes mix the analyte in a mixing chamber which then inject the reaction solution to an optical cell, and 2) a spectrometer that records UV-Vis or IR absorption spectra as a function of time (Figure 8).

The reactants are "rapidly" combined in a mixing chamber and injected into the optical cell. The mixing process causes a short delay time called the dead time due to mechanical mixing limitations. The optical spectra are collected as a function of time at different time intervals in an optical cell using UV-Vis or IR absorption spectroscopy. Single wavelength kinetics measurements are useful for kinetic analysis. The main limitation with stopped-flow rapid mixing techniques is the deadtime, which is in the order of milliseconds (ms), that prevents the identification of species that live shorter than the ms timescale. Reactions ideal to study with stopped-flow techniques are within the ms to minutes timescale.[59,60]

Metal hydrides complexes are quite amenable to stopped-flow kinetic analysis because of their UV-Vis and IR spectroscopic handles which often afford strong optical handles for monitoring reaction progress. When the metal hydride complex of interest does not have a clear optical handle in the accessible optical window, photometric acids and bases (those with unique spectra properties depending on their protonation state) can be used to probe the proton transfer reaction.[62,63] Common IR spectroscopic handles are M-H stretches which are usually in the 1,800 − 1,900 cm$^{-1}$ range and M-CO stretches which are typically in the 1,800 − 2,200 cm$^{-1}$ range. These handles can afford information about the formation or scission of the M-H bond in a particular reaction, or changes in the electronic structure and charge of the metal complex versus the M-CO reporter, respectively. However, it is important to note that the oscillator strength of M-H stretches can vary drastically from complex to complex depending on the atomic weight of the metal and cannot always be detected on the optical timescale.
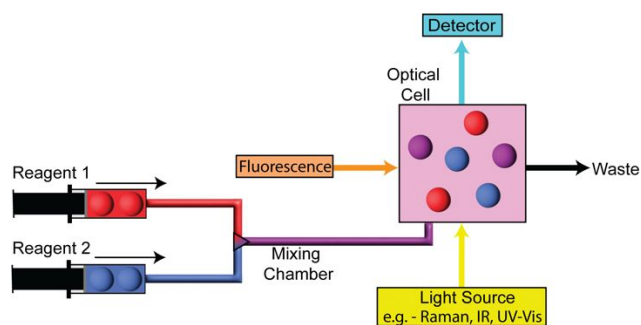
ARTICLE



**Figure 8.** Stopped-flow rapid mixing coupled with optical spectroscopy is used to monitor reactions on the timescale of milliseconds to minutes. Solutions in separate syringes are rapidly injected into an observation cell and a stopping syringe (not pictured). Once the cell and stopping syringe are filled, the flow is stopped and optical changes in the observation cell are tracked using a UV-Vis, infrared or fluorescence spectrophotometer.

**Transient Absorption Spectroscopy** While stopped-flow rapid mixing techniques can be used to study proton transfer kinetics using optical monitoring techniques, there are several limitations to the technique. As discussed above, the dead time due to mechanical mixing can obscure the observation of reactions that are complete before the first time point can be measured. Additionally, in most cases the stopped-flow rapid mixing technique requires either the reduced metal complex or the transition metal hydride to be isolable. The use of the flash-quench method with transient absorption spectroscopic monitoring has been used to circumvent both of these limitations.

In studying proton transfer kinetics involving metal hydrides, the flash-quench method involves the excitation of a photosensitizer with a short laser pulse (flash). This generated an excited-state that can transfer an electron to a transition metal complex in solution. This results in a more reduced transition metal complex (and oxidized photosensitizer), which is more basic and can be protonated by an external acid. Similar to the optical monitoring in stopped-flow rapid mixing experiments, spectroscopic handles of the transition metal hydrides, the reduced metal complexes, the acids or bases, or even the reduced and oxidized photosensitizer can all be monitored in order to obtain a complete picture of the reaction landscape.

**Electrochemistry** Electroanalytical methods are powerful tools for probing electron transfer reactions with coupled chemical reactions, such as proton transfer. Apriori knowledge of the coupled chemical reactions is useful to interpret the nature of the electrochemical observations, and can often be achieved by spectroscopic measurements.[64] In a typical cyclic voltammetry experiment, an electron transfer reaction (the reduction of M to $M^-$, Equation 13) is induced by scanning the electrode potential; measurement of the current responses as a function of applied potential informs both on the electron transfer process and any coupled chemical reactivity.

The Nernst equation (Equation 14) governs the equilibrium concentration of a reversible one-electron redox system:[65]

$$M + e^- \rightleftharpoons M^- \tag{13}$$

$$E = E^{o'} + \frac{RT}{F} ln \frac{C_M}{C_{M^-}} \tag{14}$$

Where E is the applied potential, $E^{o'}$ is the formal reduction potential, and $C_M$ and $C_{M^-}$ are the concentrations of the oxidized and reduced species, respectively. R is the ideal gas constant, T is the temperature, and F is Faraday's constant.

If a chemical reaction consumes one of the species involved in the Nernstian equilibrium, the equilibrium will be perturbed and changes to the current-potential response will be observed. From these deviations, kinetic and mechanistic information about the coupled chemical reaction can be gleaned. The EC reaction sequence is one where an electrochemical event (E) occurs first and is followed by a coupled chemical reaction (C), and is of relevance to the focus of this review.

$$M + e^- \rightleftharpoons M^- \tag{15a}$$

$$M^- + HA \xrightarrow{k_{PT}} MH + A^- \tag{15b}$$

Equation 15 describes such a system, where the reduction of complex M to $M^-$ occurs followed by the reaction of $M^-$ and proton source HA to form the metal hydride species MH (and conjugate base $A^-$). When the proton transfer is irreversible on the electrochemical timescale, the consumption of the electron transfer product $M^-$ leads to a shift in the cathodic peak potential ($E_{p,c}$) and a loss of the anodic peak on the reverse sweep. Analysis of the peak shift as a function of substrate concentration and/or scan rate can be used to calculate the rate constant for the coupled chemical reaction, $k_{PT}$.

$$E_{p,c} = E^{o'} - 0.78 \frac{RT}{F} + \frac{RT}{2F} ln \left( \frac{RTk_{PT}[HA]}{F \quad \upsilon} \right) \tag{16}$$

When the metal hydride species is an intermediate in catalysis, kinetics of its formation can sometimes still be extracted from cyclic voltammograms using 1) catalytic plateau current analysis or 2) foot of the wave analysis (FOWA). We refer the reader to in depth reviews that comprehensively cover applications of these techniques to extract elementary rate constants.[72–75]

Briefly, for complex reactions that involve multiple electron transfer processes and multiple chemical steps, catalytic plateau current analysis can be used to determine the rate constant for the rate-limiting step. For this analysis, electrocatalytic systems must be in the kinetically limited regime of cyclic voltammograms (zone KS), where an S-shaped wave is observed and the forward and backwards scans are perfectly overlapping. An example of this is the two-electron, two-proton reaction to make $H_2$ in an ECEC mechanism. Equation 17 directly correlates the plateau current versus the observed rate constant, $k_{obs}$, which equals $k_{PT}[HA]$ when proton transfer is the rate-limiting, second order proton transfer step. The remaining variables are known constants; A is the active

surface area of the electrode, $C_M^o$ is the concentration of the catalyst M, D is the diffusion coefficient of catalyst M, n is the number of unique electron transfer processes that occur at the electrode per catalyst and n' is the catalyst equivalents used per turnover. Many reviews and reports discuss plateau current analysis in detail.[72,73,75,76]

$$i_c = nFAC_M^0\sqrt{Dn'k_{obs}} \qquad (17)$$

Foot-of-the-wave analysis (FOWA) is often used to extract kinetics of catalysis when plateau currents are not accessible, such as when substrate consumption or other side phenomena are present. Similar to plateau current analysis, modified analytical expressions are employed based on the mechanism. Derivation and presentation of these expressions are beyond the scope of this review, and readers are directed to detailed reviews in the literature to apply FOWA properly.[75,77,78] Importantly, FOWA provides information about the first chemical step ($k_1$) regardless of whether this is the rate-limiting elementary step or not. In many reactions that form metal hydride intermediates, the initial proton transfer to form the metal hydride is the first chemical step. However, we emphasize that information about the reaction mechanism is needed to confidently use FOWA. The main assumption to extrapolate kinetics from FOWA is that the onset of catalysis around the "foot" of the catalytic response is akin to the "S" shaped curve.

In summary, cyclic voltammetry can be a powerful tool to extract out kinetics of proton transfer reactions that occur as stand-alone reactions or as part of catalytic transformations.

## Part II: Applications of Kinetic Acidity in Fuel-Forming Reactions

This section will expand on the implications of proton transfer kinetics involving transition metal hydride complexes with respect to fuel-forming reactions such as the hydrogen evolution reaction (HER) and carbon dioxide reduction reaction ($CO_2$RR). Proton transfer to and from the catalyst is often a key elementary step in catalytic processes, so understanding the associated kinetics will help guide researchers on how to tune reactivity, impart selectivity, or improve efficiency. Due to the nature and reactivity of transition metal hydrides in catalysis, experimentally determining elementary proton transfer rate constants can be extremely difficult. For example, the transition metal hydride complex may not be chemically isolable or stable for long periods of time, limiting direct characterization of the metal hydride intermediate. Also, the catalyst may give rise to complicated electrochemical responses and require exceptionally careful mechanistic and kinetic analysis to extract reliable proton transfer rate constants. Herein, we will highlight studies that have successfully measured proton transfer rate constants for a number of different catalytic systems, which have been divided into three categories: 1) direct proton transfer to the metal center of monometallic catalysts, 2) proton transfer to monometallic complexes involving ligand cooperativity, and 3) proton transfer in multimetallic systems.

We will also discuss studies that demonstrate the impacts of proton transfer kinetics on overall catalyst efficiency, selectivity, and mechanism and offer perspective on how fundamental understanding of elementary proton transfer rate constants can be leveraged to aid the fuel-forming catalysis field.

### Measuring Proton Transfer Kinetics of Monometallic Metal Hydride Intermediates

Monometallic metal catalysts are a simplified platform to understanding heterogenous and nature inspired (metalloenzyme) fuel-forming processes.[79–81] While catalytic reactions for fuel formation, such as hydrogen evolution reaction (HER) and carbon dioxide reduction reaction ($CO_2$RR) can involve a variety of chemical and electrochemical steps,[82,83] this section will focus on the proton transfer kinetics associated with metal hydride formation. Discussion in this review is focused on the studies in which kinetic information was determined and reported.

#### Hydrogen evolution catalysts

**Cobaloxime** Cobalt diglyoxime, or cobaloxime, catalysts are well-studied systems for HER in both organic and aqueous media (Figure 9).[81] During electrocatalytic HER, cobaloxime complexes generally exhibit a sequential ECEC mechanism where two electron and two chemical steps occur to evolve $H_2$.[73,84,85] The 4-step ECEC mechanism of HER for cobaloximes proceeds as follows: 1) Co(II) is reduced to Co(I); 2) Co(II) is protonated to form Co(III)-H; 3) the Co(III)-H is reduced to Co(II)-H; and 4) the Co(II)-H is protonated to release $H_2$ and regenerate the Co(II) species to close the catalytic cycle (Figure 10).[73,85–87] In this section, the proton transfer kinetics for cobalt hydride formation in organic and aqueous media will be discussed, along with a discussion of the influence of solvent on proton transfer.
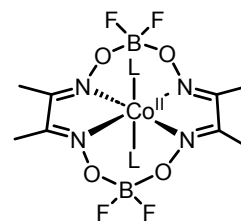


**Figure 9.** Example structure of cobaloxime

Our lab has applied electroanalytical techniques, including FOWA and plateau current analysis, to determine the proton transfer rate constants involved in the catalytic cycle for HER of Co(dmgBF$_2$)$_2$(L)$_2$ (dmgBF$_2$ = difluoroboryl-dimethylglyoxime) in acetonitrile.[73] By evaluating the electrocatalytic activity of Co(dmgBF$_2$)$_2$(L)$_2$ with *para*-substituted anilinium derivatives of different acid strengths, our lab was able to gain a deeper picture how the driving force affects the proton transfer kinetics associated with the first chemical step of the catalytic cycle, which describes protonation of the Co(I) species to form a Co(III)-H. FOWA afforded proton transfer rate constants, $k_1$,

ranging from $3.06 \times 10^4$ to $2.73 \times 10^8$ M$^{-1}$ s$^{-1}$ for acids with p$K_a$ values ranging from 12 to 7, respectively, in CH$_3$CN.[73] For the acids with p$K_a$ > 8.5, there is a linear correlation between log($k_{PT}$) and p$K_a$. At higher driving forces, the proton transfer kinetics almost reach diffusion limited rates, causing the values to deviate from the linear relationship. Our group also used plateau current analysis to extract global rate constants ($k_{gl}$) from this system, which describes the second proton transfer step, protonation of Co(II)-H ($k_{gl} = k_2$). This analysis led to proton transfer rate constants approximately 3 orders of magnitude lower than those obtained for $k_1$ from FOWA, which supported that the first proton transfer step is not rate-limiting. While outlining the determination of $k_2$ is beyond the scope of this review, our group's analysis of these voltammograms highlights the importance of matching the correct kinetic analysis to the correct elementary rate constant. Furthermore, it showcases the strength of electrochemical systems in obtaining proton transfer rates directly versus overall rates from flash photolysis methods.
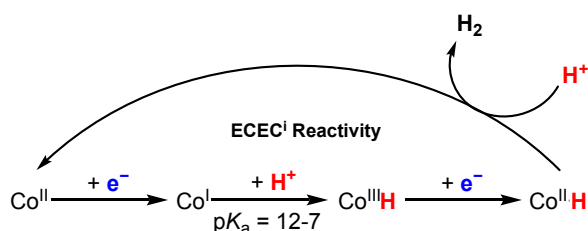


**Figure 10.** Proposed mechanism for hydrogen evolution for the cobaloxime shown in Figure 9 via ECECi mechanism. Bimolecular reactivity has been excluded for clarity.

As mentioned above, cobaloximes have also been studied in aqueous media. While it is known that solution pH influences HER reactivity with cobaloxime catalysts, the kinetics of proton transfer has not been deeply investigated in aqueous media to the best of our knowledge. Natali investigated the role of pH in photochemical HER using Co(dmg)$_2$(Cl)(py) (py = C$_5$H$_5$N) as a catalyst with a photosensitizer and reductant. They reported a pH balance between maintaining the reactivity of the sacrificial reductant, ascorbic acid, and the formation of the Co(III)-H (Figure 11).[88] If conditions were too acidic (pH < 5), ascorbic acid's biprotic equilibria favors the protonated form and disfavors the conjugate bases that are reduced by the photosensitizer [Ru(bpy)$_3$]$^{2+}$ (bpy = 2,2'-bipyridine). If conditions were too basic (pH > 5), Co(I) protonation is weakly favored. These effects can be observed through the turnover frequency (TOF) for HER, where a significant drop in H$_2$ formation is observed above and below pH 5. While proton transfer kinetics were not explicitly extrapolated, the strong pH dependence of the catalytic performance suggests that maximizing PT driving forces can be experimentally limiting.
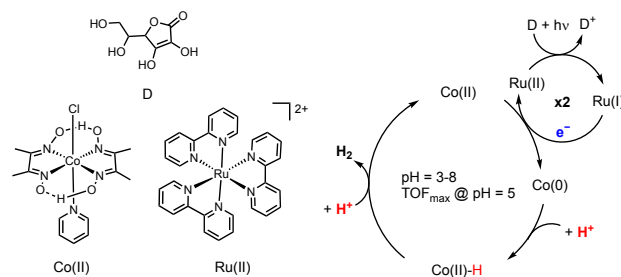


**Figure 11.** Structure of Cobaloxime Co(dmg)$_2$(Cl)(py), Ru(bpy)$_3$ sensitizer, and electron donor ascorbic acid. The proposed mechanism of Co(dmgO$_2$H)$_2$(L)$_2$ starts with initial stepwise reductions, followed by subsequent protonations to evolve hydrogen.

Overall, the HER catalytic cycle of cobaloxime has been thoroughly studied in organic and aqueous media. While the kinetics in aqueous conditions are not completely understood, the kinetic studies in organic media serve as an excellent template when studying a catalyst's ability to form a metal hydride at various driving forces.

**Iron Porphyrins** Metalloporphyrin complexes have been prominent in the field of HER and CO$_2$RR chemistry, serving as stable ligand platforms for a variety of metals and synthetic modifications.[82,89,90] Porphyrin ligands give a rigid and stable coordination environment to stabilize reactivity intermediates and can withstand a variety of solvent and acidic media. This makes metalloporphyrins an excellent model to systematically study the kinetics of metal hydride formation.
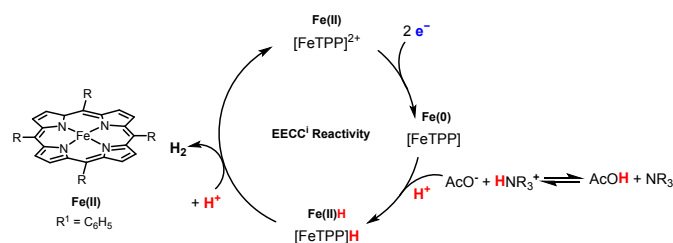


**Figure 12.** Structure of Fe Porphyrin with cocatalyst, and proposed mechanism of hydrogen evolution with cocatalyst tertiary amine via EECC mechanism.

Saveant and coworkers first studied an Fe(tetraphenylporphyrin) (TTP) complex for HER catalysis, which follows a 4-step EECC mechanism. The first reduction processes, Fe(II/I) and Fe(I/0), are followed by a protonation of the Fe(0) to Fe(II)-H. Subsequent steps include protonation of the hydride, and finally H$_2$ evolution and regeneration of the Fe(II) species. The Fe(II)-H formation step was evaluated with cyclic voltammetry and digital simulations, and a proton transfer rate constant of $2 \times 10^8$ M$^{-1}$s$^{-1}$ was determined when using triethylammonium as the proton source. The relatively fast proton transfer to form the metal hydride established a benchmark for proton transfer in TTP systems, and subsequent work in the field focused on how the primary coordination sphere enhances these rates.

Nocera and coworkers evaluated how rates could be controlled using external cocatalysts.[92] A variety of tertiary amines were added with Fe(TTP) and catalysis was probed electrochemically and spectroscopically. The tertiary amines had a p$K_a$ range of 8.8 - 11.3 in DMF for their conjugate acids, but interestingly did not bind to Fe(I) intermediates, and by extension did not modulate the nucleophilicity of the metal center towards subsequent protonation. Instead, the cocatalysts pre-associated with the acetic acid (AcOH, p$K_a$ = 13.2 in DMF). This pre-association allowed formation of ammonium ions (Figure 12), where the driving force for protonation of the iron center and subsequent H$_2$ evolution increased. Analysis of plateau currents allowed for rate extrapolation for metal hydride formation via PT which were close to diffusion limits, $k_{PT}$ = 2.8 x $10^8$ – 1.0 x $10^{10}$. While direct correlations to TOF/TON were not discussed, the clear increase in proton transfer rate constants shows the effect the cocatalysts have on metal hydride formation and overall catalytic activity.

**Carbon Dioxide Reduction Catalysts**

In contrast to HER, CO$_2$RR is significantly more complex as CO$_2$ can be reduced to a variety of products.[93] To limit the scope of this discussion, formate forming catalysts will be the main focus. Pathways that form formate proceed through a M-H intermediate, where the M-H bond transfers a hydride to generate formate upon reacting with CO$_2$. By contrast, in reactions that reduce CO$_2$ to CO, CO$_2$ generally directly binds to a nucleophilic metal center to promote a C-O bond scission mechanism.[83,94,95] The highly reduced nature of these metal centers can accentuate metal hydride formation to promote insertion to CO$_2$ versus parasitic side reactivity towards HER. Thorough reports by Yang and coworkers discuss in great detail how thermodynamic strategies can be leveraged to avoid HER while maximizing product formation.[11,93] While thermodynamic studies on molecular CO$_2$ reduction catalysts are ubiquitous,[83,93,96,97] kinetic control over CO$_2$RR is limited. In this section, we will briefly discuss opportunities in the field to study kinetic hydride formation for systems involving CO$_2$RR.

**Platinum Phosphine** Yang and coworkers reported a highly selective formate-production catalyst, [Pt(dmpe)$_2$]$^{2+}$.[93,95] Upon two-electron reduction, the complex reacts with phenol to form a platinum hydride complex under a CO$_2$ atmosphere. Scan-rate-dependent cyclic voltammetry data show that the rate of protonation of [Pt(dmpe)$_2$] (> $10^5$ s$^{-1}$) is at least 4 orders of magnitude faster than the rate of CO$_2$ binding to [Pt(dmpe)$_2$] (1.27 s$^{-1}$). Therefore, metal hydride formation is under kinetic control. Subsequent reactivity of the Pt(II)-H depends on thermodynamics, where the possible products are formate or H$_2$. The CO$_2$ insertion between the Pt(II)-H bond is a thermodynamically downhill process ($\Delta G_{PT}$ = -2.2 kcal/mol), whereas protonation of Pt(II)-H is thermodynamically uphill ($\Delta G_{PT}$ = 5.5 kcal/mol). Given these values, selectivity for formate is favored over H$_2$ evolution. Therefore, the product selectivity is dominated both by kinetic and thermodynamic control. Computational studies have also been completed by Head-Gordon and on an iron polypyridine electrocatalyst, showcasing the interplay of thermodynamic and kinetic control on product

selectivity.[98] These experimental and computation reports are extremely useful to understand how to use kinetics and/or thermodynamic parameters to curb deleterious pathways in catalysis.
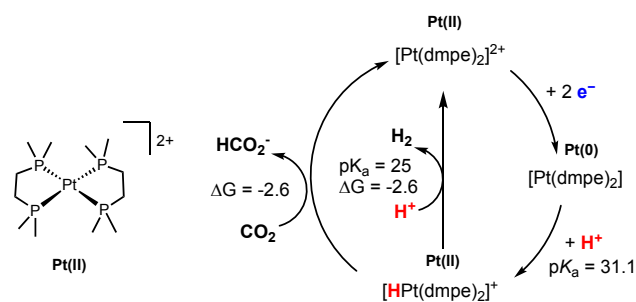


**Figure 13.** Structure of Platinum DMPE, and proposed mechanism of CO$_2$ to formate via an EECC[i] mechanism

To expand on the thorough reports on molecular formate-forming catalysts,[93,99–101] there are promising systems available for kinetic studies of metal hydride formation. For example, Brookhart and coworkers studied an iridium pincer trans-dihydride complex (Figure 14) which selectively favors formate products with a FE = 85% in CH$_3$CN using water as a proton source.[99] While CO$_2$ binding intermediates were identified via NMR spectroscopy, the formation of the metal hydride was not studied in the absence of CO$_2$. Therefore, there may be unique kinetic properties available for this system to inform design of CO$_2$ to formate catalysts.

More complex metal hydride motifs, such as monometallic systems that cooperate with pendant ligands to promote catalysis and multimetallic systems that have multiple active metal centers, are also known formate-producing catalysts. Artero and coworkers have investigated a 1$^{st}$ row CpCo(P$_2$N$_2$) complex (P$_2$N$_2$ = 1,5-diaza-3,7-diphosphacyclooctanes) (Figure 14) that drives the formation of formate while suppressing HER.[100] The catalyst forms a metal hydride intermediate via ligand cooperativity, which can then bind with CO$_2$. The pendant amine ligand assists in catalysis by stabilizing the CO$_2$ binding intermediates while thermodynamically suppressing HER, giving a FE = 92% in DMF using H$_2$O as a proton source. While the kinetics were studied in terms of CO$_2$RR catalysis, the convoluted dynamics to form the metal hydride are not fully understood.

While the previously described reactivity proceeds through a metal hydride intermediate, researchers are also interested in designing catalysts for orthogonal hydride transfer. Yang and coworkers note the challenges in designing systems to prevent metal hydride formation and promote pendant base protonation reactions.[102] The next section touches on how pendant amine ligands can tune proton transfer reactions towards or away from metal hydride formation, and serves as a transition to more complex reactivity with ligands that participate in proton transfer and catalysis.

Berben and coworkers synthesized a series of multimetallic carbonyl clusters which supports a multimetallic hydride that activates CO$_2$ to formate production; the last section of Part II covers the unique metal hydride motif's catalytic capabilities

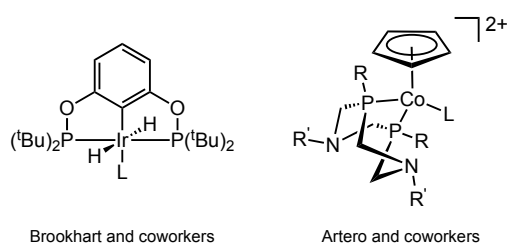and the kinetic acidity of the multimetallic system in more detail.[103]



**Figure 14.** Structures of Ir(POCOP) and $[CpCo(P_2N_2)L]^{2+}$, $CO_2$ to formate electrocatalysts for suggested study.

A deeper understanding of kinetic acidity (and basicity) is poised to advance the field of selective $CO_2RR$. It can help guide understanding of how to select for the various accessible products, as chemists can tailor complexes to systematically tune kinetics for both HER or $CO_2RR$. The lack of appreciable comparisons between the kinetics of metal hydride formation versus $CO_2$ binding to compliment the rigorous computational and thermochemical studies reported presents a standing barrier. As the field grows, complexes that can support both aqueous and organic catalytic reactions are invaluable to measure the impact of kinetics and establish meaningful trends with existing thermodynamic studies.

**Measuring Proton Transfer Kinetics When Ligand Cooperativity is Involved**

As highlighted throughout the review, proton transfer to and from the metal center is kinetically challenging, which can lead to bottlenecks in catalytic processes. Therefore, researchers have been interested in using ligand cooperativity in the second coordination sphere to give rise to faster kinetics of fuel-forming catalytic cycles. Often times, this reactivity is leveraged by protonating a kinetically-accessible ligand protonation site, after which the ligand-protonated intermediate will tautomerize to form the thermodynamically-favored metal hydride complex (Figure 15). In order to exploit ligand acid-base functionality for this purpose, both the thermodynamics and the position of the proton-responsive ligand should be considered. For example, the pendant base should be basic enough to effectively accept the proton from the external acid source and be positioned proximal to the metal center to feasibly shuttle protons from the ligand to the metal. There are several examples of proton-responsive ligands that have been successfully used to mediate proton transfer to and from the metal center including amines, oxygen and nitrogen-based hangman arms or axial sites, thiolates, and cyclopentadienyl rings. In this section, each class of compounds will be discussed in terms of measuring proton transfer kinetics and the impact the kinetics have on the efficiency, selectivity, or mechanism of fuel-forming reactions.
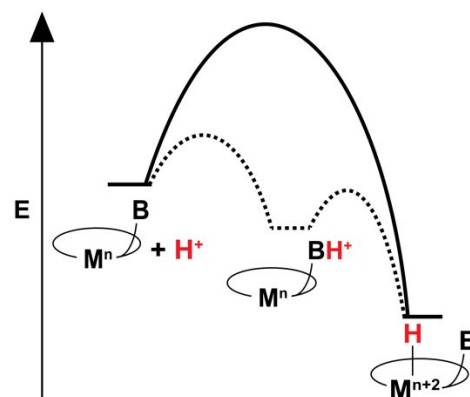


**Figure 15.** Reaction coordinate diagram for the proton transfer to a coordination complex, showcasing the kinetically favored pathway via ligand protonation followed by intramolecular proton transfer (dotted lines) and the direct metal-protonation pathway (solid line) to form the metal hydride complex

**Amines** Pendant amines have been incorporated into molecular complexes for their ability to facilitate proton transfer in catalytic cycles. This has been widely accomplished using the $P_2N_2$ (1,5-diaza-3,7-diphosphacyclooctanes) and PNP $(R_2PCH_2)_2NR')$ ligand scaffold (Figure 16). Bullock and coworkers recently reviewed the catalytic activity of molecular complexes containing this class of ligands, where the most widely studied complex is the family of $[Ni(P_2N_2)]^{2+}$ complexes.[104–107] Herein, we aim to highlight the works that have studied proton transfer kinetics for $[Ni(P_2N_2)]^{2+}$ with respect to HER, as well as other key kinetic studies with complexes containing pendant amines in the ligand backbone.
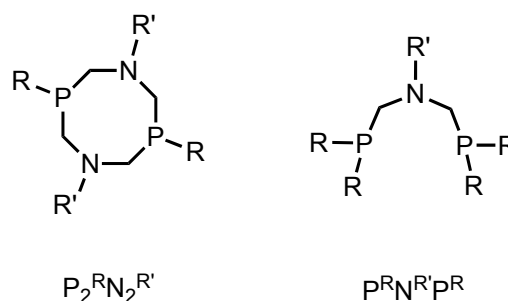


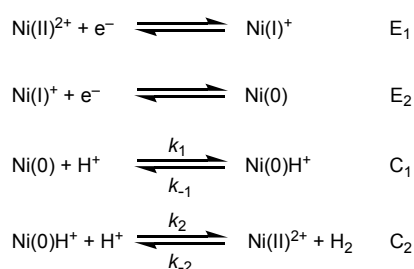**Figure 16.** General structure of $P_2N_2$ and PNP ligands

Due to the complexity of the catalytic cycle for $[Ni(P_2N_2)]^{2+}$, kinetic information obtained is dependent on the catalytic mechanism. Depending on the strength or concentration of the proton source, an EECC pathway or ECEC pathway can be operative during HER (Scheme 2). Often times, the two mechanisms are in competition, which makes it extremely difficult to deconvolute kinetic information from parallel reaction pathways. Therefore, it is crucial to have a deep understanding of the mechanism at hand to interpret kinetic information for $[Ni(P_2N_2)]^{2+}$. The proton transfer kinetics have been successfully extracted when solely the EECC or ECEC pathway are under operation. We will describe the two kinetic analyses of this system and the implications they have on leveraging kinetic acidity to enhance catalysis.

**Scheme 2.** Catalytic cycle for $[Ni(P_2^R N_2^{R'})]^{2+}$ including both the ECEC and EECC pathways. The steps regarding exo protonation of the $Ni^I$ species and the R and R' groups on the phosphorous and nitrogen atoms have been omitted for clarity.
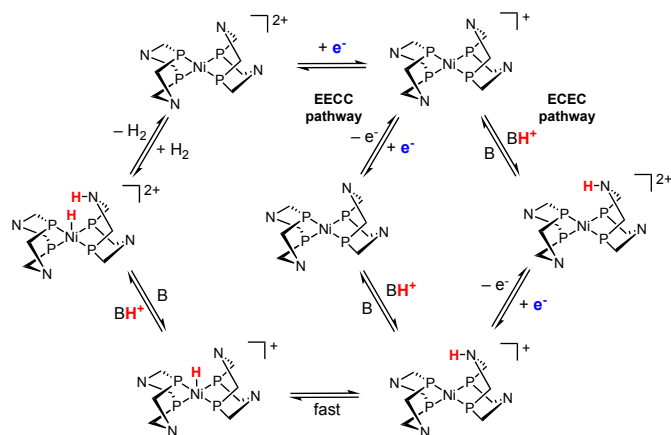


Our group studied the kinetics of elementary reactions steps for hydrogen production catalyzed by $[Ni(P_2^{Ph} N_2^{Ph})]^{2+}$ via the EECC pathway (Scheme 8).[108] Modulating the proton source $pK_a$ to a weaker acid, (anilinium; $pK_a$ = 10.6 in $CH_3CN$) the EECC mechanism was exclusively operative. Peak shift analysis and FOWA were used to quantify the proton transfer rate constant for the first chemical step. Peak shift analysis afforded a $k_1$ value of $1.2 \times 10^6$ $M^{-1}$ $s^{-1}$ and FOWA yielded a similar value of $6.5 \times 10^6$ $M^{-1}$ $s^{-1}$, which describes the protonation of the pendant amine of the Ni(0) species. Ligand protonation is followed by fast intramolecular proton transfer to form the Ni(II)-$H^+$ species, so the $k_1$ values effectively dominate the hydride formation kinetics. Although the kinetics for the elementary steps after hydride formation are beyond the scope of this review, we direct readers to this specific work to understand how stopped-flow kinetic analysis, current plateau, and NMR spectroscopy can be used to determine proton transfer rate constants for additional steps in HER.
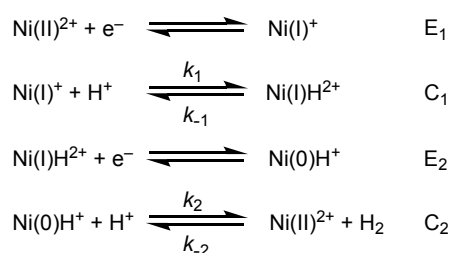
**Scheme 3.** EECC Mechanism for $[Ni(P_2^{Ph} N_2^{Ph})]^{2+}$

$$Ni(II)^{2+} + e^- \rightleftharpoons Ni(I)^+ \qquad E_1$$

$$Ni(I)^+ + e^- \rightleftharpoons Ni(0) \qquad E_2$$

$$Ni(0) + H^+ \underset{k_{-1}}{\overset{k_1}{\rightleftharpoons}} Ni(0)H^+ \qquad C_1$$

$$Ni(0)H^+ + H^+ \underset{k_{-2}}{\overset{k_2}{\rightleftharpoons}} Ni(II)^{2+} + H_2 \qquad C_2$$

As mentioned earlier, accessible kinetic information for $[Ni(P_2^R N_2^{R'})]^{2+}$ will be dependent on the mechanism at play. Wiedner and coworkers used $E_{cat/2}$ values to perform a kinetic analysis of the protonation of $[Ni(P_2^{Ph} N_2^{Ph})]^{2+}$ using $(DMF)H^+$ ($pK_a$ = 6.1 in $CH_3CN$) as the proton source ($E_{cat/2}$ is the first maximum potential in the first derivative of the $i$–$E$ plot).[109] This stronger acid promotes the ECEC pathway, where $k_1$ now

describes the protonation rate constant for proton transfer to the pendant amine of the Ni(I) species. When the researchers applied FOWA using $i_{cat}$ values to determine $k_1$, they saw proton transfer rate constants lower than those predicted based off of electrochemical digital simulations. This was because the reduction potential of Ni(I)-$H^{2+}$ overlaps with the foot of the wave, causing an inflation of observed current values for kinetic analysis. Due to this complication, the authors used analysis of the $E_{cat/2}$ to determine the value of $k_1$. This analysis is similar to FOWA, but instead takes advantage of the fact that $E_{cat/2}$ is easily discernable from the rest of the CV features. Since the current at $E_{cat/2}$ corresponds to half of $i_{cat}$, this method can be used to more reliably determine $k_1$ for the ECEC mechanism. Plots of the pseudo-first-order rate constants versus the concentration of $DMF(H)^+$ after correction for homoconjugation ultimately lead to determination of $k_1$ to be $3.3 \times 10^5$ $M^{-1}$ $s^{-1}$. This investigation highlights how necessary it is to have a detailed mechanistic understanding of the catalytic system at play before applying kinetic analysis. Without such knowledge, rate constants can easily be misinterpreted.

**Scheme 4.** ECEC Mechanism for $[Ni(P_2^{Ph} N_2^{Ph})]^{2+}$

$$Ni(II)^{2+} + e^- \rightleftharpoons Ni(I)^+ \qquad E_1$$

$$Ni(I)^+ + H^+ \underset{k_{-1}}{\overset{k_1}{\rightleftharpoons}} Ni(I)H^{2+} \qquad C_1$$

$$Ni(I)H^{2+} + e^- \rightleftharpoons Ni(0)H^+ \qquad E_2$$

$$Ni(0)H^+ + H^+ \underset{k_{-2}}{\overset{k_2}{\rightleftharpoons}} Ni(II)^{2+} + H_2 \qquad C_2$$

In both mechanistic regimes, the pendant amines in $[Ni(P_2^R N_2^{R'})]^{2+}$ are leveraged to mediate proton transfer to evolve hydrogen and circumvent kinetic barriers to direct metal protonation. Additional work by Artero, Costentin and coworkers focuses on the bidirectionality ($H_2$ evolution/$H_2$ oxidation) of the $[Ni(P_2^R N_2^{R'})]^{2+}$ system, where all of the kinetic constants were extracted for the proposed reversible reaction scheme.[110] Notably, this study shows the importance of the $P_2^R N_2^{R'}$ ligand scaffold not only for its conformational flexibility and proper positioning of the pendant amine for metal hydride formation, but also for the effective deprotonation of the nickel-hydride species.

In comparison to the $[Ni(P_2^R N_2^{R'})]^{2+}$ system, the $[Ni(PNP)_2]^{2+}$ systems are active for $H_2$ oxidation, but inactive for $H_2$ evolution due to the improper positioning of the pendant amine to mediate metal hydride formation.[80] Therefore, placement and flexibility of pendant amines are crucial factors to consider in order to observe kinetic improvements in fuel-forming reactions.

The $P_2^R N_2^{R'}$ ligand scaffold has also been extended to cobalt-based electrocatalysts for HER. Dubois and coworkers studied the HER catalytic performance of $[Co(P_2^{Ph} N_2^{Ph})(CH_3CN)_3][BF_4]_2$ with triflic acid as the proton source.[111] Interestingly, this catalytic activity is observed only with the mono-$P_2 N_2$ ligand complex, as opposed to the two required for the nickel complexes discussed above. When the group studied an

analogous complex lacking a pendant amine, [Co(dppp)(CH$_3$CN)$_3$][BF$_4$]$_2$, no significant activity for HER was observed under the same conditions that [Co(P$_2^{Ph}$N$_2^{Ph}$)(CH$_3$CN)$_3$][BF$_4$]$_2$ showed high catalytic activity. This shows the critical role of the pendant amine in the cobalt-based complexes' catalytic activity, yet the kinetics of the elementary proton transfer steps within the catalytic cycle have not been well documented. Therefore, there is still valuable information to gain from an in-depth kinetic analysis of proton transfer involving cobalt complexes containing P$_2^R$N$_2^{R'}$ ligands

**Hangman Porphyrins and Other Axial Positioned Proton Responsive Groups**   Researchers have also been interested in ligand motifs that offer pendant protonation sites that position the acid-base functional group above the metal center active site to improve proton transfer kinetics for fuel-forming reactions. One example of this includes "hangman" macrocycles. This idea was pioneered by the Nocera group, where the macrocycle typically consists of a porphyrin or corrole and the hangman moiety consists of an acid/base functional group (carboxylic acid, sulfonic acid, amine, amide, etc.) in the ligand backbone that "hangs" above the metal active site to serve as a local proton source (Figure 17). Like the P$_2$N$_2$ ligands, the basicity and proximal location of the hangman group is important for optimizing catalytic performance. There are several hangman platforms that have been studied, most of them based off Co, Fe, or Ni. In this section, the available proton transfer kinetics will be discussed for each metal center as well as their impacts on fuel-formation processes. A similar effect of acid/base functional groups positioned above the metal center via modifications to bipyridine and phenanthroline ligands will also be presented.
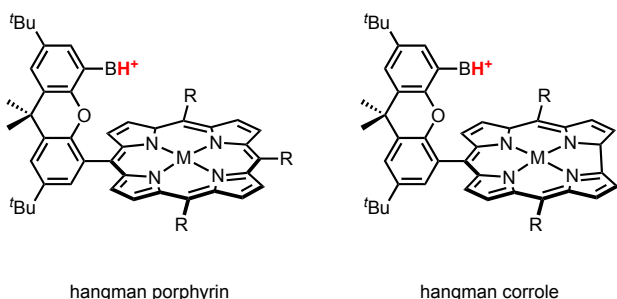


**Figure 17.** General hangman macrocycle platforms where M = Co, Fe, or Ni

To understand the effect of the hangman group on the proton transfer kinetics involved in the hydrogen evolution reaction, Nocera and coworkers reported the rate constant for intramolecular proton transfer from the carboxylic acid hangman group to the reduced cobalt center of a cobalt hangman porphyrin (Scheme 5).[112] Notably, this was the first direct measure of a proton transfer rate constant for HER conversion, which is described by the proton transfer step described in the EC mechanism shown in Scheme 10.
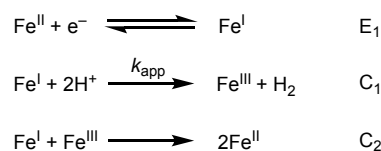
**Scheme 5.** EC Mechanism for Co-based hangman porphyrin system
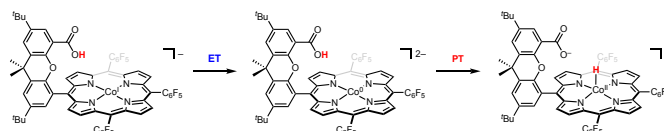


Peak shift analysis showed that the relationship between the peak potential and the natural logarithm of the scan rate ($\ln(\upsilon)$) deviated from linearity at higher scan rates. The authors attributed this non-ideality at higher scan rates to a kinetic competition between the ET step and PT step of Scheme 5. Since the ET step starts to become rate-limiting at faster scan rates, experimental peak shift analysis could not be reliably employed. Therefore, CV simulations were employed to simulate the peak potential as a function of scan rate. Optimization of the simulated values afforded a $k_{PT}$ value of 8.5 x 10$^6$ s$^{-1}$ for the PT step of Scheme 5. Hammes-Schiffer and coworkers used transition state theory to calculate the $k_{PT}$ value for the same hangman system, and the theoretical calculations resulted in a rate constant of 1.4 x 10$^6$ s$^{-1}$, which agrees with experimental values.[113] To compare these values with proton transfer for a non-hangman porphyrin system, Nocera and coworkers performed a similar tandem experimental and digital simulation analysis to determine a second order rate constant for the protonation of an analogous cobalt non-hangman porphyrin complex with benzoic acid. This value was on the order of 10$^3$ M$^{-1}$s$^{-1}$, suggesting that the pendant proton relay in the hangman system enhances the proton transfer rate analogous to an effective benzoic acid concentration greater than 3000 M. Therefore, the "hangman effect" shows that proton transfer kinetics are improved by the proximal location of the hangman moiety to the reduced metal center, leading to enhanced HER activity. To this point, Nocera and coworkers studied cobalt hangman porphyrin systems with varying distances between the carboxylic acid functional group and the Co center. They observed that the shortest distance resulted in higher activity for HER and concluded that intramolecular proton transfer can be facilitated by the position of the hangman arm.[114]

In addition to cobalt-based hangman porphyrins, Nocera and coworkers have also studied iron hangman porphyrin's catalytic activity toward HER using FOWA.[115] In 2014, they studied a series of iron complexes with hanging dibenzofuran porphyrin ligands that undergo hydrogen evolution by the following proposed mechanism described by Scheme 6.
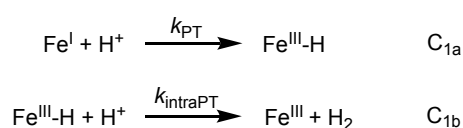
**Scheme 6.** Proposed mechanism for HER involving Fe-based hangman porphyrins

$$Fe^{II} + e^- \rightleftharpoons Fe^I \qquad E_1$$

$$Fe^I + 2H^+ \xrightarrow{k_{app}} Fe^{III} + H_2 \qquad C_1$$

$$Fe^I + Fe^{III} \longrightarrow 2Fe^{II} \qquad C_2$$

The steady state approximation was applied to use FOWA to determine the apparent rate constant, $k_{app}$, for the general steps corresponding to step C$_1$ in Scheme 6. The authors observed a correlation between the hanging group p$K_a$ value

and the observed $k_{app}$ values; as the proton donating ability of the pendant group increases, the rate of catalysis also increases. The highest $k_{app}$ value was observed for the complex bearing the strongest acid in the hanging group, a sulfonic acid, at high acid concentrations. They suggest the HER rate enhancement is due to the complex's ability to perform intramolecular proton transfer, which has a lower energetic barrier than intermolecular proton delivery. A 2021 report by Dey and coworkers used cyclic voltammetry and FOWA to further unravel the mechanism and kinetics of HER for iron porphyrins containing proton relay arms.[116] A deeper dive into the mechanism for step $C_1$ in Scheme 6 by cyclic voltammetry shows that the two protons interact with the Fe(I) center as follows:

**Scheme 7.** Proposed mechanism for HER proton transfer steps involving Fe-based hangman porphyrins

$$Fe^I + H^+ \xrightarrow{k_{PT}} Fe^{III}\text{-}H \qquad C_{1a}$$

$$Fe^{III}\text{-}H + H^+ \xrightarrow{k_{intraPT}} Fe^{III} + H_2 \qquad C_{1b}$$

where step $C_{1b}$ in Scheme 7 is the rate-determining step. Therefore, the experimentally determined proton transfer rate constants correspond to the protonation of the Fe(III)-H via intramolecular proton transfer from the proton relay arm, $k_{intraPT}$, rather than the H—Fe(III) formation. Since protonation of the Fe(I) metal center is not rate-limiting, it suggests there is minimal electronic and structural rearrangement to form H—Fe(III). Although the kinetics reported are not directly correlated to the concept of kinetic acidity of transition metal hydrides, the results from reports by Nocera and Dey regarding Fe-based hangman porphyrins shed light on ways to control catalytic rates of HER, which can be useful to minimize unwanted HER side reactions. Specifically, the authors observed kinetic trends with two parameters regarding the protonation of Fe(III)—H⁻: (a) the $pK_a$ of the distal base and (b) the number of basic substituents in the arm. The first-order reaction rate increases as the strength of the exogenous acid increases (the added proton source must be more acidic than the basic substituent in the hangman arm in order to observe HER activity). Additionally, the authors observed that proton transfer rates diminished for an iron porphyrin complex containing three pyridines as opposed to two. They attribute this to a "proton sponge" effect, slowing down intramolecular proton transfer to Fe(III)—H⁻.

To understand the kinetics and mechanism of proton transfer for $H_2$ production for nickel-based hangman porphyrins, Nocera and coworkers used cyclic voltammetry and digital simulations for a series of nickel hangman complexes with hanging carboxylic acids.[117] Their electrochemical data and complimentary DFT calculations were consistent with a CE mechanism for Ni(II) hydride formation (Scheme 8).

**Scheme 8.** CE Mechanism for Ni-based hangman porphyrin system
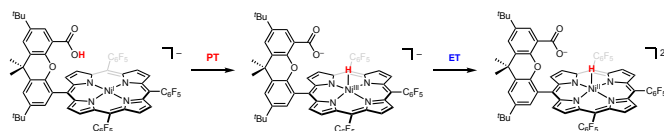


In this case, the authors were able to simulate experimental CV data to obtain a lower limit of $10^5$ s⁻¹ for the forward proton transfer rate constant associated with PT step of Scheme 8. When compared to the Co analogue, the Ni hangman porphyrin systems showed improved catalytic activity for HER, which is attributed to the accessible CE pathway circumventing the need to proceed through a formal metal 0 oxidation state. From the studies discussed herein on hangman platforms based off Co, Fe, and Ni, it is clear the electronics of the metal center play a key role in the mechanism and kinetics of proton transfer for hangman porphyrin complexes. Yet, in all systems, the position of the hangman arm is advantageous to control the delivery of protons within the catalytic cycle, resulting in proton transfer rate constants higher than those observed for non-hangman systems.

Similar to hangman porphyrins, proton-responsive functional groups have been positioned axial to the metal center on bipyridine and phenanthroline ligands to alter proton transfer kinetics and change product selectivity. Specifically, oxygen- or nitrogen-based groups have been incorporated into the class of manganese and rhenium tricarbonyl bipyridine and phenanthroline complexes. Without any proton-responsive modifications, these catalysts have excellent selectivity for CO under $CO_2$ reduction conditions. However, incorporation of oxygen- or nitrogen-based groups that hang above the metal center increase selectivity for products that proceed through metal hydride intermediates, such as $H_2$ or formate (Figure 18).[118–124] Siewart and coworkers have studied and reviewed the effect of proton relays in manganese and rhenium tricarbonyl complexes with respect to $CO_2$RR, so we direct readers to their review for an extensive report on this system.[118] A key takeaway from their review is that appending proton responsive groups in axial positions relative to the metal center enables a favorable interaction between the pendant proton and the metal active site. This agrees with the observations made by Nocera and coworkers for hangman porphyrin complexes. Both classes of complexes position the proton appropriately to facilitate intramolecular proton transfer and increase metal hydride formation kinetics.
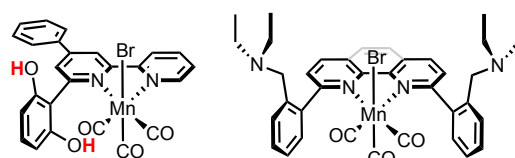


**Figure 18.** Examples of manganese tricarbonyl bromide catalysts with pendant bases incorporated into axial sites of the bipyridine or phenanthroline ligand

One key example was reported by Gobetto, Nervi, and coworkers where they studied the electrochemical behavior of *fac*-Mn(dhbpy)(CO)₃Br (dhbpy = 4-phenyl-6-(1,3-dihydroxybenzen-2-yl)2,2'-bipyridine) under a $CO_2$

atmosphere.[122] The dhbpy ligand contains two acidic hydroxyl groups. They reported that this complex has a much higher Faradaic efficiency for formate, which is formed via metal hydride formation, compared to an analogous complex without any hydroxyl groups. As more exogenous acid is added to this system, formate production increases.[123] Gobetto, Nervi, and coworkers suggest that addition of axial hydroxyl groups changes the proton transfer kinetics for Mn hydride formation, where the hydride formation pathway is now in kinetic competition with $CO_2$RR. Similar selectivity changes were observed by Daasbjerg and coworkers when they studied electrochemical $CO_2$ reduction by a series of manganese tricarbonyl complexes with bipyridine ligands containing axial amine groups.[121] The axial positioning of amine groups on the bipyridine ligand changed the product selectivity from CO to formate. Therefore, proper placement of hydroxyl or amine groups can have a drastic effect on selectivity of fuel-forming reactions.

**Thiolates** Thiolate ligands have played a critical role in designing molecular mimics for a variety of metalloenzymes. At the heart of these enzymatic energy-related transformations are the proton transfer steps associated with the sulfur atom and metal center. This section will focus on the kinetic analyses for monometallic iron-based thiolate complexes and the associated experimentally determined proton transfer rate constants. Due to the relevance of iron thiolate complexes to metalloenzymes, the vast majority of mechanistic and kinetic analyses of the thiolate motif are on multimetallic systems, of which there is a more in-depth analysis in **Part II – Measuring proton transfer kinetics in multimetallic hydride systems**.

To understand proton migration between sulfur and metal atoms with respect to nickel-based hydrogenase systems, Henderson and coworkers reported protonation kinetics of [Ni(SR)(triphos)][BPh$_4$] (R = Ph or Et; triphos = (Ph$_2$PCH$_2$CH$_2$)$_2$PPh) with 2,6-dimethylpyridinium (lutH+) using stopped-flow rapid mixing with UV-Vis spectroscopy monitoring (Scheme 14).[125] They report electronic and geometric arguments for the different reactivity when R = Ph vs Et. When R = Ph, a rate law for proton transfer to the sulfur atom was consistent with a single-step equilibrium reaction involving protonation of the sulfur atom, and the forward proton transfer rate constant was determined to be 20 ± 2 M$^{-1}$ s$^{-1}$ (Equation 18). However, when R = Et, stopped-flow data analysis yields a rate law consistent with two, coupled equilibria: an initial sulfur atom protonation with $k_1$ = (1.8 ± 0.3) x 10$^2$ M$^{-1}$ s$^{-1}$ followed by a second equilibrium, which the authors hypothesize is a partial proton transfer to the nickel via an η$^2$-EtS-H ligand due to the electron-donating alkanethiolate with $k_2$ = (0.05 ± 0.01) s$^{-1}$ (Equation 19). Therefore, the initial rate of proton transfer to [Ni(Set)(triphos)]+ is an order of magnitude faster than that of [Ni(SPh)(triphos)]+, likely due to the decrease in steric congestion. However, electronics control migration of the proton to the nickel center; the EtS ligand increases electron density at the Ni center, allowing the proton to effectively bridge the nickel and sulfur sites.
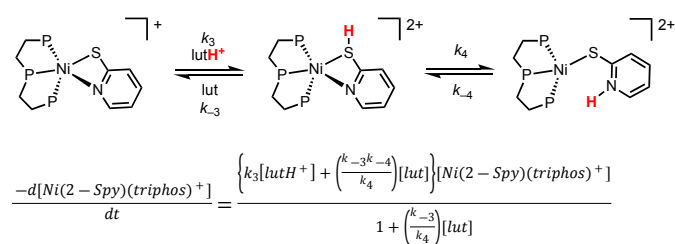
**Scheme 9.** Generic mechanism of proton transfer between [Ni(SR)(triphos)]+ (R = Ph or Et; triphos = (Ph$_2$PCH$_2$CH$_2$)$_2$PPh) and 2,6-dimethylpyridinium (lutH+). $k_2$ only applicable for R = Et. The phenyl rings of the triphos ligand have been abbreviated for clarity.



$$-\frac{d[Ni(SPh)(triphos)^+]}{dt} = \{k_1^{SPh}[lutH^+] + k_{-1}^{SPh}[lut]\}[Ni(SPh)(triphos)^+] \qquad (18)$$
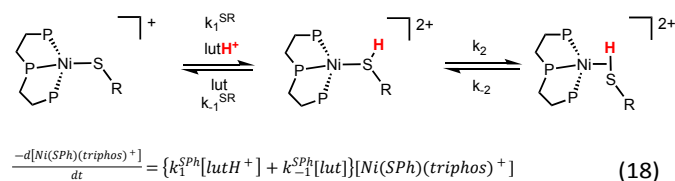
$$-\frac{d[Ni(SEt)(triphos)^+]}{dt} = \frac{\{k_1^{SEt}k_2^{SEt}[lutH^+] + (k_2^{SEt} + k_{-2}^{SEt})\}[Ni(SEt)(triphos)^+]}{k_1^{SEt}[lutH^+] + k_{-1}^{SEt}[lut]}$$

$$(19)$$

In a later study, Henderson and coworkers reported the proton transfer mechanism and kinetics for the reaction of [Ni(2-Spy)(triphos)]+ (2-Spy = 2-pyridinethiolate) with 2,6-dimethylpyridinium (lutH+) using a combination of calculations and stopped-flow rapid mixing.[126] The pyridinethiolate ligand has two possible initial protonation sites: the sulfur and nitrogen atoms. Theoretical methods indicated that the kinetic protonation site is the coordinated sulfur, but the thermodynamic product corresponds to an N-protonated pyridine where the nitrogen is not coordinated to Ni (Scheme 10). The coordination of the nitrogen in the pyridine ring makes N inaccessible to protonation and therefore and promotes initial sulfur protonation. Kinetic analysis led to a proton transfer rate constant for sulfur protonation ($k_{PT}$ = $k_3$ = 1.38 x 10$^4$ M$^{-1}$ s$^{-1}$) and the associated rate law (Equation 20).

**Scheme 10.** Protonation mechanism of [Ni(2-Spy)(triphos)]+ by 2,6-dimethylpyridinium (lutH+). The triphos ligand has been abbreviated for clarity.



$$-\frac{d[Ni(2-Spy)(triphos)^+]}{dt} = \frac{\left\{k_3[lutH^+] + \left(\frac{k_{-3}k_{-4}}{k_4}\right)[lut]\right\}[Ni(2-Spy)(triphos)^+]}{1 + \left(\frac{k_{-3}}{k_4}\right)[lut]}$$

(20)

The authors note that this proton transfer rate constant is at least two orders of magnitude higher than those of [Ni(SR)(triphos)]+ complexes. They hypothesize that this is a result of anchimeric assistance, where the electronegative nitrogen atom facilitates proton transfer to the sulfur site. This is a key example of how to extract proton transfer kinetics to coordinated sulfur sites, as well as how to extract mechanistic information for proton movement between multiple basic sites

in the ligand backbone. However, the proton is not reported to migrate to the Ni center, which is in contrast to the [Ni(Set)(triphos)]$^+$ complex shown above. This highlights the importance of matching the thermodynamics of the pendant base to the thermodynamics of the metal hydride. If the pendant base is too thermodynamically favored, then the proton cannot feasibly shuttle to the metal center, ultimately preventing metal hydride formation. As mentioned above, the involvement of thiolate protonation and their role in catalytic transformations will be further discussed with respect to multi-metallic systems in **Part II – Measuring proton transfer kinetics in multimetallic hydride systems**.

**Cp rings** Although proton transfer reactions involving carbon-based acids are typically slow, Cp and Cp* rings have unique dynamic behavior where they can serve as kinetically accessible protonation sites in organometallic complexes.[127–132] However, the involvement of the Cp ring depends largely on the electronics of the coordination complex itself. This class of ligand-participation is documented to a lesser extent than the other proton-responsive ligands discussed throughout the review.

Our group has identified a proton transfer mechanism involving initial Cp protonation for the class of CoCp(dxpe) complexes using deuterium scrambling studies and performed peak shift analysis to determine proton transfer rate constants (Scheme 11). Deuterium incorporation into the Cp ring was observed by reacting CoCp(dxpe) with deuterated acids CD$_3$COOD (p$K_a$ = 23.51) and anilinium-d$_3$ (p$K_a$ = 10.41). In both cases, deuterium incorporation was observed in the Cp and deuteride region via $^2$H NMR spectroscopy, suggesting that the deuteron initially docks on the Cp ring, and then quickly tautomerizes to form the thermodynamically favored DCo$^{III}$ complex. We hypothesized this mechanism is due to large electronic and structural reorganization energy associated with the reaction of CoCp(dxpe) with acid to form [HCoCp(dxpe)]$^+$ and the conjugate organic base. Using cyclic voltammetry and peak shift analysis, we extracted apparent $k_{PT}$ values for the protonation reaction that range from $10^2 – 10^7$ M$^{-1}$ s$^{-1}$. Transient absorption was also used to photogenerate the Co(I) species in the presence of acid sources, and slightly different $k_{PT}$ values were obtained as compared to those using the electrochemical methods. These differences, however, are due to minor ground-state interactions present in the photoinitiated studies which are absent in the electrochemical study, and the overall $k_{PT}$ values are in the same range depending on the methods used.

At endergonic or mildly exergonic conditions, a Brønsted LFER is observed, but the values plateau under more exergonic conditions because the reaction kinetics become gated by the rate of CH$_3$CN dissociation (Figure 19). From this work, we developed the hypothesis that when kinetic barriers to metal-based protonation are insurmountable, the proton leverages the dynamic behavior of the ligand scaffold to circumvent kinetic barriers to metal hydride formation. This hypothesis has led our lab to systematic investigations of ligand-based PCET pathways to metal hydride formation, which are currently underway.

**Scheme 11.** Mechanism for the electrochemical reaction to form [HCoCp(dxpe)]$^+$. The Co(III/II) reduction step and CH$_3$CN ligand loss have been excluded for clarity. The PT step is depicted endo, but exo protonation is also possible.
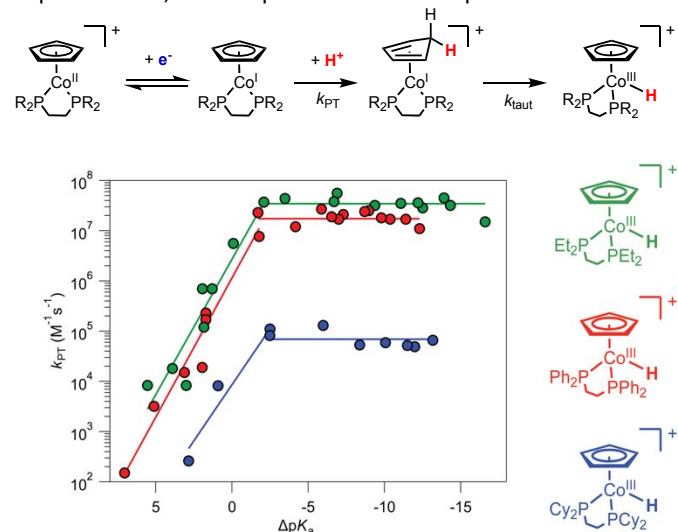




**Figure 19.** Brønsted plots for the apparent proton transfer rate constant of Co(I)Cp(dxpe) species using nonbulky acids to form [HCoCp(dxpe)]$^+$

The protonation of metallocenes have also received attention, specifically with respect to catalytic N$_2$-to-NH$_3$ conversion. While ferrocene, an extremely well-studied Group 8 metallocene, has been shown to form an iron hydride via direct iron protonation in the presence of acid, the protonation of other Group 6 and Group 9 metallocenes has been explored to a lesser extent.[134,135] Peters and coworkers used pulsed electron paramagnetic resonance (EPR) techniques at low temperature to characterize the protonation products of Cp*$_2$Co where Cp* = pentamethylcyclopentadienyl.[127] The EPR data, along with DFT calculations, support that protonation occurs at the Cp* ligand, resulting in a weak C-H bond (<29 kcal mol$^{-1}$) and challenge the common conception that Cp* is an innocent ligand (Figure 20). They suggest this reactivity may be leveraged to serve as a PCET donor for N-H bond formation and exploit new-found reactivity of this class of ligands for proton management. While the Peters group has laid out a strong thermodynamic study of ligand-based proton transfer to Cp*$_2$Co, there is a gap in knowledge when it comes to the proton transfer kinetics for this system.[136] Understanding the rate at which the proton transfers to and from the Cp* ring would be useful information to modify and improve systems for catalytic N$_2$-to-NH$_3$ conversion cycles and shut off deleterious HER side reactions.
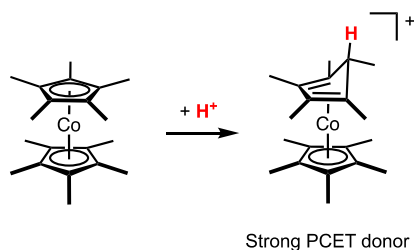
**Figure 20.** Protonation mechanism of Cp*$_2$Co

## Measuring proton transfer kinetics in multimetallic hydride systems

Kinetic studies of proton transfer at multimetallic complexes have been primarily driven by the need to develop a better mechanistic understanding of fuel-forming reactions catalyzed by metalloenzymes and to improve the performance of synthetic catalysts.[137–142] Multimetallic clusters can also be regarded as molecular models of heterogeneous or nanomaterial catalysts since they maintain structural complexity (e.g., metal-metal bonds, multiple protonation sites, etc.) while their elementary reaction steps can be characterized and studied by using molecular techniques.[101,143–145] Here, we highlight novel examples that use the desirable characteristics of multimetallic clusters, and in a few cases, coupled with ligand participation to influence the kinetics of hydride formation and fuel-forming catalysis.

**Fe-S Based Clusters** Hydrogenase enzymes, especially the [FeFe] system (Figure 21), have received a significant attention because of their ability to reduce protons to H$_2$ which is one of the targeted alternative fuels.[146] Protonation of the [Fe$_2$S$_2$] unit has been proposed to involve the formation of a transient hydride intermediate in either a bridging or terminal binding mode.[147,148] Additionally, calculations predict that both the primary and secondary coordination sphere ligands can serve as protonation sites to promote H$_2$ evolution catalysis.[149,150] Therefore, establishing mechanistic principles for proton transfer at synthetic clusters is fundamental to understanding the detailed mechanisms by which proton transfer occurs at [FeFe]-hydrogenases and developing efficient fuel-forming catalysts.
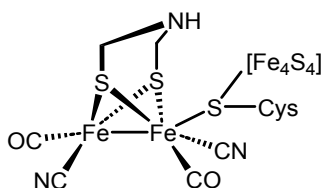


**Figure 21.** Chemical structure of the [FeFe] hydrogenase active site.

The protonated azadithiolate ligand of the [Fe$_2$S$_2$] active site has been suggested to serve as proton source for the formation of H$_2$. To help understand this functionality, Lomoth, Ott, and coworkers employed a combination of spectroscopic methods to study the proton transfer b behavior of an [FeFe]-hydrogenase mimic, eFe($\mu$-adt)(CO)$_4$(Pme$_3$)$_2$ (adt = $N$-benzyl-azadithiolate) (Figure 22, complex **1**), in acetonitrile.[151] In the presence of strong acids (p$K_a$ < 2.6), the central nitrogen atom of the azadithiolate ligand is protonated (the p$K_a$ of the ligand-protonated complex **2** is 12). However, when HCl (p$K_a$ = 10.3) was used, time-resolved IR spectroscopy monitoring the changes in CO stretching frequencies revealed that the ligand protonated complex undergoes a tautomerization to generate a hydride species **3**, with an estimated p$K_a$ value of 15. Interestingly, the presumably unimolecular tautomerization reaction exhibits first order kinetics with respect to HCl with a bimolecular rate constant of 2.2 M$^{-1}$ s$^{-1}$. These observations imply that the azadithiolate protonation is kinetically more accessible although the Fe—Fe bond is the more basic site, and that the hydride formation is catalyzed by HCl. The doubly protonated complex **4**, with p$K_a$ (hydride) = 8 and p$K_a$ (ammonium proton) = 5, can be accessed by treating the ligand-protonated complex with strong acids such as triflic acid (p$K_a$ = 2.6), albeit at a slow proton transfer rate ($k_{PT}$ = 0.15 M$^{-1}$ s$^{-1}$). However, this reaction becomes substantially faster ($k_{PT}$ > 10$^{2}$ $^{-1}$ s$^{-1}$) with HBr (p$K_a$ = 5.4) despite having a lower driving force. The formation of the doubly protonated species **4** was hypothesized to occur via the initial, rate-limiting tautomerization followed by a rapid protonation at the azadithiolate ligand (Figure 22). In this chemistry, the tautomerization is likely hindered by the bulky phosphine ligands and the use of small hydrohalic acids helps facilitate this process such that the hydride can form. The steric demand imposed by PMe$_3$ has been noted in the proton transfer chemistry of the related diiron dithiolate complexes whereby substitutions with smaller ligands like cyanide result in fast protonation at cyanide ($k_{PT}$ > 8 x 10$^5$ M$^{-1}$ s$^{-1}$) followed by tautomerization to form hydride complexes ($k_{PT}$ = 8–9 x 10$^{-3}$ s$^{-1}$).[152] Importantly, the catalytic formation of H$_2$ was only observed when the ligand-protonated complex is reduced by one electron, suggesting that there may be large electronic or structural changes (e.g., ligand dissociation) upon reduction that help circumvent the rate-limiting hydride formation.
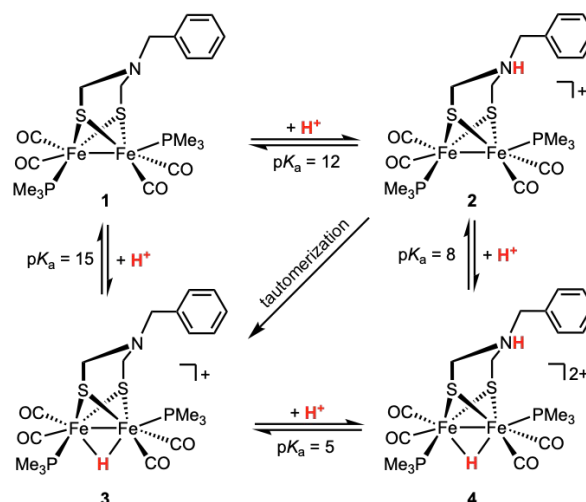


**Figure 22.** Proton transfer reactions involving the hydrogenase mimic [FeFe($\mu$-adt)(CO)$_4$(Pme$_3$)$_2$] (adt = $N$-benzyl-azadithiolate).

In the absence of sufficiently basic ligands, Pickett and coworkers hypothesize that protonation of synthetic clusters occurs directly at the metal—metal bonds to generate bridging hydride species. In their study, the rate constants of protonation at metal-metal bonds in a series of synthetic diiron-dithiolate $H_2$ evolution catalysts, $Fe_2(X)(CO)_{6-n}(PMe_3)_n$ (X = substituted dithiolate and n = 1 or 2), were measured using stopped-flow UV-Vis and FT-IR techniques in acetonitrile (Figure 23).[153] Notably, the proton transfer rate constants spanning 6 orders of magnitude ($k_{PT}$ = 3.7 x $10^{-3}$ – 4.3 x $10^3$ $M^{-1}s^{-1}$) were found to vary with the energy of the metal—metal bond based highest occupied molecular orbital (HOMO) as measured by the oxidation potentials of the complexes ($E_{1/2}$):

$$\log (k_{PT}) = 0.20 - 11.7 E_{1/2} \qquad (21)$$

This relationship implies the direct engagement of the HOMO in the protonation of the metal—metal bond, which also explains the stereoelectronic influence of the nature of the bridging dithiolate ligand on the rate of proton transfer. For example, it was found that dialkyldithiolate-bridged complexes exhibit enhanced rate for protonation as compared to the monoalkyldithiolate bridged congeners. Analyses of the solid-state molecular structures and DFT studies reveal that the monoalkyldithiolate bridged complexes display only terminal arrangement of the CO ligands, whereas the dialkyldithiolate bridged species contain a semibridging CO group. The switching of a terminal CO to a semibridging binding mode was found to destabilize the HOMO, consistent with the lower $E_{1/2}$ values and hence faster proton transfer kinetics. The authors also observed faster proton transfer rate constants for complexes with more electron donating $PMe_3$ groups installed. Notably, the linear relationship (Equation 21) predicts a turnover frequency of ~$10^3$ $s^{-1}$ for the formation of a bridging hydride at the enzymatic active site, which is an order of magnitude slower than that observed in the enzyme, suggesting that proton transfer at the active site may instead involve rapid formation of a terminal hydride as a kinetic product.
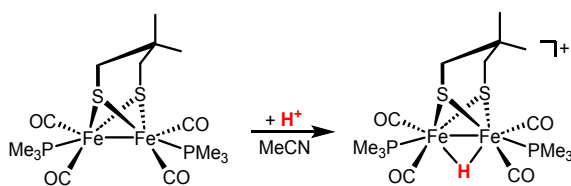


**Figure 23.** Representative proton transfer reaction of a diiron dithiolate complex, $Fe_2(X)(CO)_4(Pme_3)_2$, where X here represents a dimethylated propane-1,3-dithiolate bridging ligand.

To further understand the proton transfer chemistry of [FeFe]-hydrogenase mimics, the Hammarström group provides direct spectroscopic evidence for a one-electron reduced form of a $H_2$ evolution catalyst [FeFe($\mu$-pdt)(CO)$_6$] (pdt = propanedithiolate) and its protonated species using time-resolved infrared and UV-Vis spectroscopy.[154] Analysis of proton transfer kinetics by monitoring the flash-quench

generated [FeFe($\mu$-pdt)(CO)$_6$]$^-$ species with varying concentrations of three weak acids (8.5 < p$K_a$ < 13.3) revealed second-order rate constants (7.0 x $10^5$ – 7.0 x $10^7$ $M^{-1}s^{-1}$, Table 1), which are several orders of magnitude faster than the reactions of neutral diiron dithiolate species (*vide supra*).[153] The resulting bridging hydride species exhibits higher $v$(CO) stretching frequencies (by 80 cm$^{-1}$) and a shorter Fe–Fe bond (by 0.06 Å). The driving force dependence of the rate constants with a Brønsted slope of 0.4 suggests a Marcus theory type charge transfer with a reorganization energy greater than 23 kcal/mol, consistent with the large structural changes due to a direct protonation at the metal centers. While the coordination sphere of [FeFe($\mu$-pdt)(CO)$_6$]$^-$ remains intact upon reduction, an analogous species [FeFe($\mu$-bdt)(CO)$_6$]$^-$ (bdt = benzenedithiolate) undergoes an Fe–S bond cleavage giving rise to different proton transfer behaviors (Figure 24). Despite having a lower p$K_a$ value (~11), the proton transfer rate constants for [FeFe($\mu$-bdt)(CO)$_6$]$^-$ are comparable to those of [FeFe($\mu$-pdt)(CO)$_6$]$^-$ which is a weaker base with an estimated value of 11 < p$K_a$ < 15.6. The authors attributed the slower proton transfer kinetics to the larger reorganization upon protonating [FeFe($\mu$-bdt)(CO)$_6$]$^-$ which involves a re-ligation of the thiolate ligand (Figure 24b). Despite the large reorganization, the protonation of [FeFe($\mu$-pdt)(CO)$_6$]$^-$ is still sufficiently fast even with moderately weak acids, suggesting that proton transfer may not be a rate-limiting step in light-driven $H_2$ formation for these complexes.
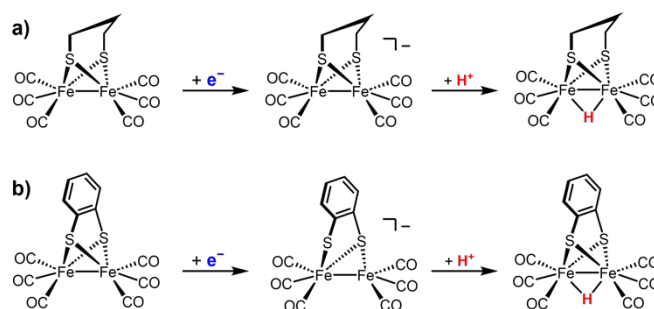


**Figure 24.** Reduction and protonation reactions of proton reduction catalysts a) [FeFe($\mu$-pdt)(CO)$_6$] and b) [FeFe($\mu$-bdt)(CO)$_6$].

Metal hydride complexes have also been implicated as key intermediates in the efficient conversion of dinitrogen to ammonia by the iron-molybdenum cofactor of nitrogenases (Figure 25)[3] and its synthetic models.[155] In addition to $N_2$, the multimetallic active sites are known to reduce a variety of substrates including those related to fuel formation like $CO_2$, CO, and $H^+$.[156] Despite the limited structural and spectroscopic characterization of the hydride intermediates,[157] it has been hypothesized that the multiple protonation sites available in the multimetallic clusters help facilitate the multi-proton/electron transfer processes required for these challenging transformations.[155]
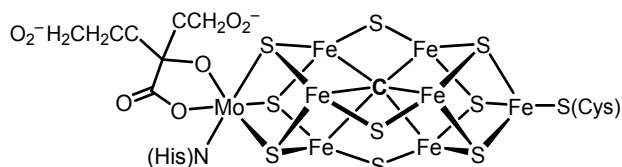
**ARTICLE**

**Figure 25.** Chemical structure of iron-molybdenum cofactor of nitrogenase enzymes.

Henderson and coworkers reported the kinetics and mechanisms of the conversions of $H^+$ to $H_2$ and $C_2H_2$ to $C_2H_4$ by a simple nitrogenase mimic, $[Fe_4S_4(SPh)_4]^{3-}$, using 2,6-dimethylpyridinium (lutH$^+$) as the proton source in acetonitrile. The kinetic profile of the proton reduction reaction exhibits two mechanistic regimes corresponding to fast and slow phases (Figure 26). The fast phase involves the initial triple protonation of $[Fe_4S_4(SPh)_4]^{3-}$ to $[Fe_4S_2(SH)_2(SPh)_3(SHPh)]$ followed by the dissociation of the protonated thiolate ligand (SHPh). This labilization is induced by cluster protonation and is essential to allow for the subsequent protonation at an open coordination site of Fe to generate a hydride species. Reduction of this hydride intermediate presumably by another equivalent of $[Fe_4S_2(SH)_2(SPh)_3(SHPh)]$ affords a "super reduced" hydride cluster $[Fe_4(H)S_2(SH)_2(SPh)_3]$ that undergoes a hydride transfer reaction to substrate ($H^+$ or $C_2H_2$) in the slow phase. Analysis of the kinetic data reveals the rate law for the fast phase and relevant rate constants associated with the proposed steps shown in Figure 26 ($k_1 = 2.5 \pm 0.3$ s$^{-1}$, $k_3/k_2 = 100 \pm 10$ M$^{-1}$ s$^{-1}$, and $k_{-1}/k_2 = (5.2 \pm 0.8) \times 10^3$ M$^{-1}$). Although the hydride formation rate ($k_3$) was not explicitly determined, this reaction was shown to be rapid at high concentrations of lutH$^+$ to productively generate $H_2$. Otherwise, at low concentrations of acid, substoichiometric amounts of $H_2$ were observed despite the quantitative conversion of the cluster. These observations suggest that a parallel reductive pathway (presumably $k_2$ step) to consume the cluster is competing with the hydride formation. Therefore, a fast proton transfer is necessary to promote substrate conversion pathways by $[Fe_4S_4]$ clusters, and this can be assisted by ligand labilization under high acid concentrations.
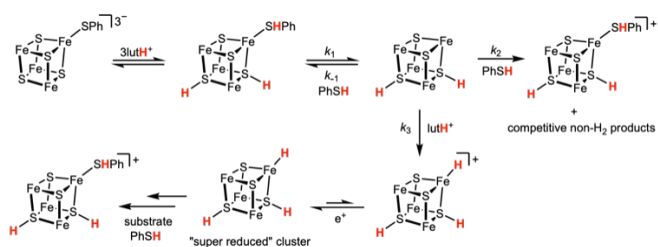


**Figure 26.** Proposed mechanism for the $H_2$-forming reaction between $[Fe_4S_4(SPh)_4]^{3-}$ and lutH$^+$ in MeCN. Only one thiol ligand is shown for clarity.

**Metal carbonyl clusters** Metal carbonyl clusters represent an important class of multimetallic catalysts that can support proton and electron transfer reactions to form hydride intermediates. Berben and coworkers utilized the multiple metal-metal bonds presented by a cobalt carbonyl cluster

$[Co_{13}C_2(CO)_{24}]^{4-}$ to statistically enhance proton transfer and $H_2$ evolution rates.[158] The IR spectra of this complex in the presence of anilinium tetrafluoroborate (AnH$^+$) suggest that the singly and doubly protonated hydride species are accessible (Figure 27a). Using cyclic voltammetry, a catalytic wave at the $[Co_{13}C_2(CO)_{24}]^{4-}/[Co_{13}C_2(CO)_{24}]^{5-}$ couple was observed to shift to more negative potentials as the concentration of AnH$^+$ increased, which is consistent with a $H_2$ evolution mechanism initiated by coupled electron and proton transfer steps (Figure 27b). Although the observed catalytic waves resemble the purely kinetic regime due to fast catalysis, the catalytic rate constant was estimated to be $2.3 \times 10^9$ M$^{-1}$ s$^{-1}$ from the current density at peak potential ($E_p$). Foot-of-the-wave analysis (FOWA) performed over a range of scan rates between 0.1–10 V s$^{-1}$ also yielded a similar catalytic rate constant of $(1.6 \pm 0.5) \times 10^9$ M$^{-1}$ s$^{-1}$. The similar values obtained suggest that the observed rate constant likely describes the rate of the first proton transfer in the catalytic cycle to generate a hydride intermediate following an overall ECCE or ECEC mechanism (see Section 1.iv.3 for more details regarding electrochemical kinetic analyses). A subsequent study using a another carbonyl cluster $[Co_{11}C_2(CO)_{23}]^{3-}$ revealed a similarly fast rate for the first proton transfer step ($k_{PT1} = 3 \times 10^8$ M$^{-1}$ s$^{-1}$).[159] However, the rate for the second proton transfer step is $k_{PT2} = 3.7 \times 10^3$ M$^{-1}$ s$^{-1}$ which is five orders of magnitude slower compared to that of $[Co_{13}C_2(CO)_{24}]^{4-}$. The independent control of the two proton transfer rates was attributed to the difference in hydride donor ability (hydricity) of the two clusters. Nevertheless, these fast, diffusion-limited proton transfer reactions promise further development of proton transfer rates for hydride formation using molecular clusters and provide insights into fuel-forming reactions mediated by heterogeneous electrocatalysts.
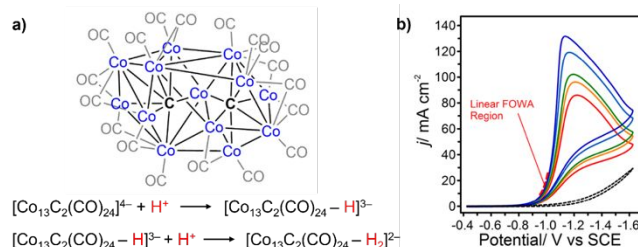


$$[Co_{13}C_2(CO)_{24}]^{4-} + H^+ \longrightarrow [Co_{13}C_2(CO)_{24} - H]^{3-}$$
$$[Co_{13}C_2(CO)_{24} - H]^{3-} + H^+ \longrightarrow [Co_{13}C_2(CO)_{24} - H_2]^{2-}$$

**Figure 27.** a) Structure of $[Co_{13}C_2(CO)_{24}]^{4-}$ and its associated singly and doubly protonation reactions b) Catalytic waves of $[Co_{13}C_2(CO)_{24}]^{4-}$ with varying concentrations of AnH$^+$. Adapted with permission from Carr, C. R.; Taheri, A.; Berben, L. A. Fast Proton Transfer and Hydrogen Evolution Reactivity Mediated by $[Co_{13}C_2(CO)_{24}]^{4-}$. *J. Am. Chem. Soc.* **2020**, *142* (28), 12299–12305. Copyright 2020 American Chemical Society.

Effects of secondary coordination sphere functional groups have also been explored using iron carbonyl clusters $[Fe_4N(CO)_{11}L]^-$ (L = $Ph_2P$-SCS) that are capable of catalyzing $H_2$ evolution and $CO_2$ conversion to formate in acetonitrile-water mixtures.[103] These transformations were proposed to involve an ECCE type mechanism in which the first chemical step is the proton transfer to form a hydride intermediate followed by hydride transfer to the substrate (Figure 28). Analyses of the

change in $E_p$ over a range of scan rates gave different proton transfer rates for clusters with varying sizes of secondary coordination sphere groups under $N_2$ and $CO_2$, despite their comparable $pK_a$ values. Under $N_2$ atmosphere, the bulkier secondary coordination sphere group was hypothesized to hinder the approach of the proton source (acetonitrile-water adducts; $(MeCN)H_2O$ or $(MeCN)_2H_2O$). However, under $CO_2$ atmosphere, the smaller pyridyl group facilitates the protonation by $MeCN-H_2O$ adducts as well as allowing for a smaller source of proton (*i.e.*, $H_2CO_3$) to engage in the protonation. Therefore, the multimetallic catalyst appended with a larger *N,N*-dimethylanilinyl group exhibits slower proton transfer rates ($k_{PT}(N_2) = 0.9 \pm 0.4$ and $k_{PT}(CO_2) = 3 \pm 1.5$ M$^{-1}$ s$^{-1}$) compared to those of the cluster bearing a smaller pyridyl secondary coordination sphere group ($k_{PT}(N_2) = 8.7 \pm 2.9$ and $k_{PT}(CO_2) = 6.1 \pm 0.8$ M$^{-1}$ s$^{-1}$). Significantly, the slower proton transfer kinetics influenced by the larger secondary coordination sphere group results in the enhanced selectivity for formate formation since the hydride transfer to bulky $MeCN-H_2O$ adducts for the competitive $H_2$ evolution is suppressed by the sterics of the secondary coordination sphere group. This work demonstrates the roles of secondary coordination sphere groups in the proton transfer chemistry of multimetallic electrocatalysts and provides design principles to promote formate selectivity when transport of protons and $CO_2$ are in competition.
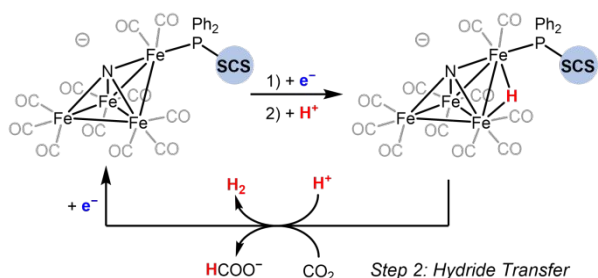


**Figure 28.** Proposed mechanistic steps for $H_2$ and formate production catalyzed by $[Fe_4N(CO)_{11}L]^-$ (L = $Ph_2P$-SCS) clusters bearing secondary coordination sphere (SCS) functional groups. Adapted with permission from Loewen, N. D.; Berben, L. A. Secondary Coordination Sphere Design to Modify Transport of Protons and CO$_2$. *Inorg. Chem.* **2019**, *58* (24), 16849–16857. Copyright 2019 American Chemical Society.

## Conclusions and Outlook

The kinetics of proton transfer involving transition metal hydride complexes has been examined and reviewed. These data make it apparent that proton transfer to and from the metal center is often slow, with values well below the diffusion limit (~$10^{10}$ M$^{-1}$ s$^{-1}$). The slow kinetics typically arise from the intrinsic barriers to metal-based proton transfer, which can be described by the large electronic and structural rearrangement that often occurs during metal-based proton transfer reactions. Additionally, steric constraints of the transition metal hydride complex and the exogenous acids and bases used in proton

transfer reactions can further contribute to the sluggish proton transfer rate constants. Due to the range of proton transfer rate constants and the different spectroscopic handles available, numerous techniques to unravel the proton transfer kinetics associated with transition metal hydride complexes have been employed. We have discussed these techniques in Part I and provided key examples of their application in Part II.

The importance of determining elementary rate constants for proton transfer steps has been discussed with respect to catalytic fuel-formation. While many researchers often acknowledge the effect of proton transfer kinetics on catalytic responses, the associated $k_{PT}$ values for elementary metal hydride formation steps are often not reported. The studies summarized in this review are prime examples of how to determine elementary proton transfer rate constants for a wide variety of systems. Determination of these $k_{PT}$ values can directly inform researchers on how to control proton mobility for energy conversion processes. We encourage researchers to take advantage of the electronic, geometric, and steric descriptors for rational design of transition metal hydride complexes for catalysis or fundamental studies. For example, if the goal is to increase the turnover frequency for hydrogen evolution, then it would be favorable to minimize electronic and structural rearrangement between the protonated and deprotonated forms of the transition metal complex in order to speed up proton transfer to the metal center. Another option is to incorporate acid/base functionality in the secondary coordination sphere to exploit the faster proton transfer kinetics associated with oxygen- or nitrogen-based acids and bases to circumvent kinetic barriers to metal-based protonation. Alternatively, if the goal is to shut off deleterious pathways that proceed through metal hydride intermediates, such as unwanted HER or $CO_2$-to-formate catalysis, then alternate design principles may be implemented to slow down metal hydride formation. Sterics is another descriptor that can be modified to either increase proton transfer rate constants or to stabilize metal hydride intermediates.

We emphasize the importance of performing tandem thermodynamic and kinetic analysis for proton transfer reactions involving transition metal hydride complexes. Experimental determination of the $pK_a$ of transition metal hydride complexes permits quantification of the driving force for proton transfer, and can ultimately better inform the choice of exogenous acid or base for fuel-forming reactions. As mentioned throughout the review, the driving force can have dramatic impacts on proton transfer rate constants and overall catalytic efficiency. Despite this important correlation, the synergy of thermodynamics and kinetics is often overlooked in the systems described in this review. This is prevalent in Table 1, where numerous entries contain a $k_{PT}$ value, but lack a corresponding $\Delta G_{PT}$ value. Therefore, we advocate that driving force determination should go hand in hand with extracting proton transfer rate constants. This is especially important because misleading chemical information and trends can be extracted by comparing rate constants across different metal hydride complexes with varying $pK_a$ values.

There are a number of entries in Table 1 with $\Delta G_{PT}$ = 0 kcal/mol, which describe self-exchange reactions. The trends that can be extrapolated from these data relate to intrinsic barriers to proton transfer to and from the metal center. For instance, $k_{PT}$ values for $CpM(CO)_3H$ complexes (M = Cr, Mo, W) decrease going down the periodic table. As the size of the metal center increases, the electronic and structural rearrangement increases, leading to larger intrinsic barriers to metal-based proton transfer. While the value for the self-exchange reaction of $HMo(CO)_2(dppe)$ and its conjugate acid is extraordinarily slow ($k_{PT}$ = 6.9 x $10^{-5}$ $s^{-1}$) due to steric constraints, this study was performed in $CH_2Cl_2$, whereas the majority of proton transfer rate constants were reported in $CH_3CN$. We caution readers to avoid direct comparison of proton transfer rate constants under different conditions. Additionally, we emphasize the importance of establishing standard conditions for measuring kinetic acidity and utilizing these conditions when there are no solubility constraints. Another point to consider for the kinetics of self-exchange reactions is that the proton donor and proton acceptor are both transition metal complexes, which tend to be sterically bulkier than organic acids and bases. This further rationalizes the extraordinarily slow $k_{PT}$ values for entries in Table 1 with $\Delta G_{PT}$ = 0 kcal/mol.

The $k_{PT}$ values with associated nonzero $\Delta G_{PT}$ values are presented in Figure 29 showing the rate equilibrium correlation for proton transfer reactions to (Figure 29a) and from (Figure 29b) transition metal complexes.
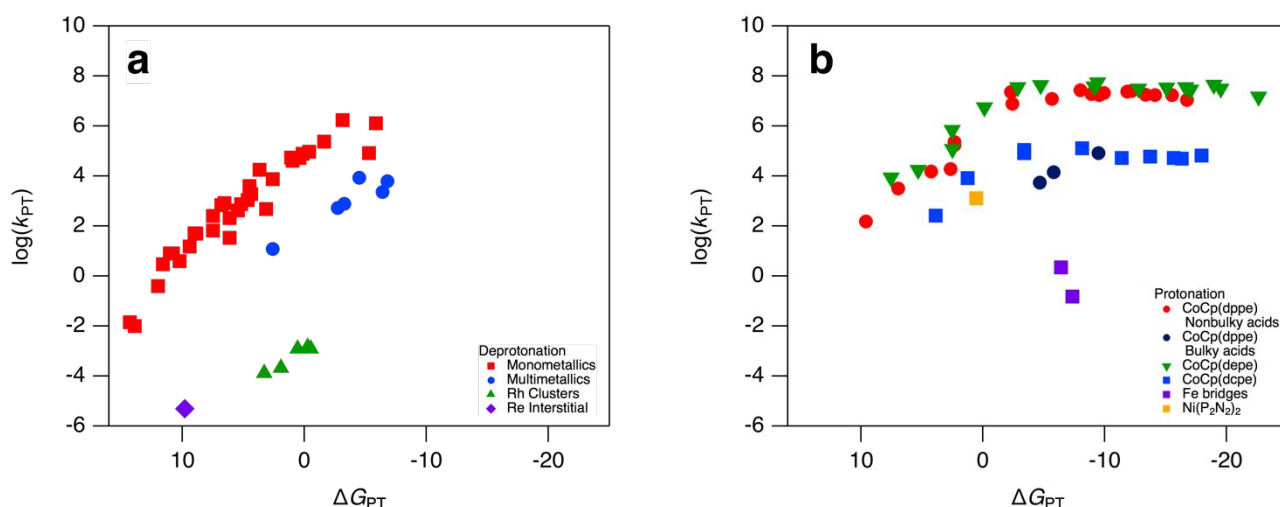


**Figure 29.** Brønsted plot for proton transfer reactions (a) to deprotonate metal hydride complexes and (b) to protonate transition metal complexes from the values presented in Table 1.

Proton transfer from metal hydride complexes (deprotonation reactions) are presented in Figure 29a. The monometallic [■] data set consists of monometallic transition metal hydride complexes and shows a correlation between the thermodynamic driving force and proton transfer kinetics, with an overall α value of −0.38. However, the multimetallic complexes, consisting of different Fe, Ru, Os [●] and Rh [▲] carbonyl clusters, the log($k_{PT}$) values show less of a dependence on $\Delta G_{PT}$ giving lower α values of −0.28 and −0.29, respectively, compared to the monometallic system. This suggests that when multiple metal centers are involved, the driving force has a lesser influence on proton transfer kinetics. Notably, the $k_{PT}$ values for the multimetallic systems fall below the $k_{PT}$ values for monometallic systems at similar driving forces. This correlates well with the connections we have emphasized on the electronic, structural, and steric descriptors for proton transfer kinetics involving transition metal hydride complexes. To further emphasize this point, the standalone data point in Figure 29a [◆] data describes proton transfer from an interstitial site of a Rh cluster, which exhibits extremely slow kinetics due the larger structural and electronic rearrangement the cluster must undergo.

Proton transfer to metal hydride complexes (protonation reactions) are presented in Figure 29b. The majority of these data are from work in our lab on CoCp(dxpe) complexes [●,●,▼,■], with additional entries coming from iron hydrogenase active-site mimics [■] and the nickel bisdiphosphine system [■]. We want to emphasize that the CoCp(dxpe) (dxpe = 1,2-bis(di-x-phosphino)ethane, where x = phenyl, methyl, or ethyl) data sets [●,●,▼,■] describe the protonation of the Cp ring as opposed to direct protonation of the cobalt center, which may be why these $k_{PT}$ values are higher than those reported for the Fe bridges [■]. Due to the lack of elementary proton transfer rate constants and corresponding thermodynamic driving force, many entries from Table 1 did not have sufficient data to plot on Figure 29b.

Although the implications of the kinetics of proton transfer involving transition metal hydrides are seen throughout the fuel-forming catalysis field, the elementary proton transfer rate constants are rarely reported for metal hydride formation; and if they are reported, then they often lack a corresponding driving force value. To conclude and reiterate our statements above, we aim to encourage readers to monitor the kinetics of proton transfer to and from metal hydride complexes, quantify the associated thermodynamic driving force, and leverage

understanding of the kinetic acidity of transition metal hydride complexes for applications in catalytic fuel forming reactions.

## Conflicts of interest

There are no conflicts to declare.

## Acknowledgements

## Notes and references

(1)     Bullock, R. M.; Helm, M. L. Molecular Electrocatalysts for Oxidation of Hydrogen Using Earth-Abundant Metals: Shoving Protons Around with Proton Relays. *Acc. Chem. Res.* **2015**, *48* (7), 2017–2026. https://doi.org/10.1021/acs.accounts.5b00069.

(2)     Francke, R.; Schille, B.; Roemelt, M. Homogeneously Catalyzed Electroreduction of Carbon Dioxide—Methods, Mechanisms, and Catalysts. *Chem. Rev.* **2018**, *118* (9), 4631–4701. https://doi.org/10.1021/acs.chemrev.7b00459.

(3)     Hoffman, B. M.; Lukoyanov, D.; Yang, Z.-Y.; Dean, D. R.; Seefeldt, L. C. Mechanism of Nitrogen Fixation by Nitrogenase: The Next Stage. *Chem. Rev.* **2014**, *114* (8), 4041–4062. https://doi.org/10.1021/cr400641x.

(4)     Blakemore, J. D.; Crabtree, R. H.; Brudvig, G. W. Molecular Catalysts for Water Oxidation. *Chem. Rev.* **2015**, *115* (23), 12974–13005. https://doi.org/10.1021/acs.chemrev.5b00122.

(5)     Agarwal, R. G.; Coste, S. C.; Groff, B. D.; Heuer, A. M.; Noh, H.; Parada, G. A.; Wise, C. F.; Nichols, E. M.; Warren, J. J.; Mayer, J. M. Free Energies of Proton-Coupled Electron Transfer Reagents and Their Applications. *Chem. Rev.* **2022**, *122* (1), 1–49. https://doi.org/10.1021/acs.chemrev.1c00521.

(6)     Wiedner, E. S.; Chambers, M. B.; Pitman, C. L.; Bullock, R. M.; Miller, A. J. M.; Appel, A. M. Thermodynamic Hydricity of Transition Metal Hydrides. *Chem. Rev.* **2016**, *116* (15), 8655–8692. https://doi.org/10.1021/acs.chemrev.6b00168.

(7)     Morris, R. H. Estimating the Acidity of Transition Metal Hydride and Dihydrogen Complexes by Adding Ligand Acidity Constants. *J. Am. Chem. Soc.* **2014**, *136* (5), 1948–1959. https://doi.org/10.1021/ja410718r.

(8)     Morris, R. H. Brønsted–Lowry Acid Strength of Metal Hydride and Dihydrogen Complexes. *Chem. Rev.* **2016**, *116* (15), 8588–8654. https://doi.org/10.1021/acs.chemrev.5b00695.

(9)     Simoes, J. A. M.; Beauchamp, J. L. Transition Metal-Hydrogen and Metal-Carbon Bond Strengths: The Keys to Catalysis. *Chem. Rev.* **1990**, *90* (4), 629–688. https://doi.org/10.1021/cr00102a004.

(10)    Tilset, M.; Parker, V. D. Solution Homolytic Bond Dissociation Energies of Organotransition-Metal Hydrides. *J. Am. Chem. Soc.* **1989**, *111* (17), 6711–6717. https://doi.org/10.1021/ja00199a034.

(11)    Brereton, K. R.; Smith, N. E.; Hazari, N.; Miller, A. J. M. Thermodynamic and Kinetic Hydricity of Transition Metal Hydrides. *Chem. Soc. Rev.* **2020**, *49* (22), 7929–7948. https://doi.org/10.1039/D0CS00405G.

(12)    Walker, H. W.; Kresge, C. T.; Ford, P. C.; Pearson, R. G. Rates of Deprotonation and PKa Values of Transition Metal Carbonyl Hydrides. *J. Am. Chem. Soc.* **1979**, *101* (24), 7428–7429. https://doi.org/10.1021/ja00518a061.

(13)    Eigen, M. Proton Transfer, Acid-Base Catalysis, and Enzymatic Hydrolysis. Part I: ELEMENTARY PROCESSES. *Angew. Chem. Int. Ed. Engl.* **1964**, *3* (1), 1–19. https://doi.org/10.1002/anie.196400011.

(14)    Calderazzo, F.; Fachinetti, G.; Marchetti, F.; Zanazzi, P. F. Preparation and Crystal and Molecular Structure of Two Trialkylamine Adducts of HCo(CO)4 Showing a Preferential NR3H+···[(OC)3Co(CO)]– Interaction. *J. Chem. Soc. Chem. Commun.* **1981**, No. 4, 181–183. https://doi.org/10.1039/C39810000181.

(15)    Weberg, R. T.; Norton, J. R. Kinetic and Thermodynamic Acidity of Hydrido Transition-Metal Complexes. 6. Interstitial Hydrides. *J. Am. Chem. Soc.* **1990**, *112* (3), 1105–1108. https://doi.org/10.1021/ja00159a033.

(16)    Borgis, D.; Hynes, J. T. Curve Crossing Formulation for Proton Transfer Reactions in Solution. *J. Phys. Chem.* **1996**, *100* (4), 1118–1128. https://doi.org/10.1021/jp9522324.

(17)    Borgis, D.; Tarjus, G.; Azzouz, H. Solvent-Induced Proton Transfer in Strongly Hydrogen-Bonded Complexes: An Adiabatic Dynamical Simulation Study. *J. Phys. Chem.* **1992**, *96* (8), 3188–3191. https://doi.org/10.1021/j100187a003.

(18)    Borgis, D.; Tarjus, G.; Azzouz, H. An Adiabatic Dynamical Simulation Study of the Zundel Polarization of Strongly H-bonded Complexes in Solution. *J. Chem. Phys.* **1992**, *97* (2), 1390–1400. https://doi.org/10.1063/1.463265.

(19)    Laria, D.; Ciccotti, G.; Ferrario, M.; Kapral, R. Molecular-dynamics Study of Adiabatic Proton-transfer Reactions in Solution. *J. Chem. Phys.* **1992**, *97* (1), 378–388. https://doi.org/10.1063/1.463582.

(20)    Kiefer, P. M.; Hynes, J. T. Nonlinear Free Energy Relations for Adiabatic Proton Transfer Reactions in a Polar Environment. I. Fixed Proton Donor–Acceptor Separation. *J. Phys. Chem. A* **2002**, *106* (9), 1834–1849. https://doi.org/10.1021/jp0134244.

(21)    Borgis, D.; Hynes, J. T. Molecular-dynamics Simulation for a Model Nonadiabatic Proton Transfer Reaction in Solution. *J. Chem. Phys.* **1991**, *94* (5), 3619–3628. https://doi.org/10.1063/1.459733.

(22)    Tully, J. C.; Preston, R. K. Trajectory Surface Hopping Approach to Nonadiabatic Molecular Collisions: The Reaction of H$^+$ with D$_2$. *J. Chem. Phys.* **1971**, *55* (2), 562–572. https://doi.org/10.1063/1.1675788.

(23)    Webster, F.; Rossky, P. J.; Friesner, R. A. Nonadiabatic Processes in Condensed Matter: Semi-Classical Theory and Implementation. *Comput. Phys. Commun.* **1991**, *63* (1–3), 494–522. https://doi.org/10.1016/0010-4655(91)90272-M.

(24)    Creutz, Carol.; Sutin, Norman. Intrinsic Barriers to Proton Exchange between Transition-Metal Centers:  Application of a Weak-Interaction Model. *J. Am. Chem. Soc.* **1988**, *110* (8), 2418–2427. https://doi.org/10.1021/ja00216a014.

(25)    Borgis, D.; Hynes, J. T. Dynamical Theory of Proton Tunneling Transfer Rates in Solution: General Formulation. *Chem. Phys.* **1993**, *170* (3), 315–346. https://doi.org/10.1016/0301-0104(93)85117-Q.

(26)    Hammes-Schiffer, S.; Tully, J. C. Proton Transfer in Solution: Molecular Dynamics with Quantum Transitions. *J. Chem. Phys.* **1994**, *101* (6), 4657–4667. https://doi.org/10.1063/1.467455.

(27)    Yu, Q.; Roy, S.; Hammes-Schiffer, S. Nonadiabatic Dynamics of Hydrogen Tunneling with Nuclear-Electronic Orbital Multistate Density Functional Theory. *J. Chem. Theory Comput.* **2022**, *18* (12), 7132–7141. https://doi.org/10.1021/acs.jctc.2c00938.

(28)    Tao, Z.; Yu, Q.; Roy, S.; Hammes-Schiffer, S. Direct Dynamics with Nuclear–Electronic Orbital Density Functional Theory. *Acc. Chem. Res.* **2021**, *54* (22), 4131–4141. https://doi.org/10.1021/acs.accounts.1c00516.

(29)    Hammes-Schiffer, S. Multiconfigurational Molecular Dynamics with Quantum Transitions: Multiple Proton Transfer Reactions. *J. Chem. Phys.* **1996**, *105* (6), 2236–2246. https://doi.org/10.1063/1.472093.

(30)    Collepardo-Guevara, R.; Craig, I. R.; Manolopoulos, D. E. Proton Transfer in a Polar Solvent from Ring Polymer Reaction Rate Theory. *J. Chem. Phys.* **2008**, *128* (14), 144502. https://doi.org/10.1063/1.2883593.

(31)    Soudackov, A. V.; Hammes-Schiffer, S. Nonadiabatic Rate Constants for Proton Transfer and Proton-Coupled Electron Transfer Reactions in Solution: Effects of Quadratic Term in the Vibronic Coupling Expansion. *J. Chem. Phys.* **2015**, *143* (19), 194101. https://doi.org/10.1063/1.4935045.

(32)    Hammes-Schiffer, S.; Stuchebrukhov, A. A. Theory of Coupled Electron and Proton Transfer Reactions. *Chem. Rev.* **2010**, *110* (12), 6939–6960. https://doi.org/10.1021/cr1001436.

(33)    Zhao, L.; Wildman, A.; Pavošević, F.; Tully, J. C.; Hammes-Schiffer, S.; Li, X. Excited State Intramolecular Proton Transfer with Nuclear-Electronic Orbital Ehrenfest Dynamics. *J. Phys. Chem. Lett.* **2021**, *12* (14), 3497–3502. https://doi.org/10.1021/acs.jpclett.1c00564.

(34)    Levina, V. A.; Filippov, O. A.; Gutsul, E. I.; Belkova, N. V.; Epstein, L. M.; Lledos, A.; Shubina, E. S. Neutral Transition Metal Hydrides as Acids in Hydrogen Bonding and Proton Transfer: Media Polarity and Specific Solvation Effects. *J. Am. Chem. Soc.* **2010**, *132* (32), 11234–11246. https://doi.org/10.1021/ja103862r.

(35)    Jordan, R. F.; Norton, J. R. Kinetic and Thermodynamic Acidity of Hydrido Transition-Metal Complexes. 1. Periodic Trends in Group VI Complexes and Substituent Effects in Osmium Complexes. *J. Am. Chem. Soc.* **1982**, *104* (5), 1255–1263. https://doi.org/10.1021/ja00369a019.

(36)    Edidin, R. T.; Sullivan, J. M.; Norton, J. R. Kinetic and Thermodynamic Acidity of Hydrido Transition-Metal Complexes. 4. Kinetic Acidities toward Aniline and Their Use in Identifying Proton-Transfer Mechanisms. *J. Am. Chem. Soc.* **1987**, *109* (13), 3945–3953. https://doi.org/10.1021/ja00247a019.

(37)    Costentin, C.; Savéant, J.-M. Why Are Proton Transfers at Carbon Slow? Self-Exchange Reactions. *J. Am. Chem. Soc.* **2004**, *126* (45), 14787–14795. https://doi.org/10.1021/ja046467h.

(38)    Gronert, S. Theoretical Studies of Proton Transfers. 1. The Potential Energy Surfaces of the Identity Reactions of the First- and Second-Row Non-Metal Hydrides with Their Conjugate Bases. *J. Am. Chem. Soc.* **1993**, *115* (22), 10258–10266. https://doi.org/10.1021/ja00075a047.

(39)    Walker, H. W.; Pearson, R. G.; Ford, P. C. Broensted Acidities of Carbonyl Hydride Complexes of Iron, Ruthenium, and Osmium: PKa Values and Deprotonation Rates in Methanol Solution. *J. Am. Chem. Soc.* **1983**, *105* (5), 1179–1186. https://doi.org/10.1021/ja00343a017.

(40)    Sampaio, R. N.; Grills, D. C.; Polyansky, D. E.; Szalda, D. J.; Fujita, E. Unexpected Roles of Triethanolamine in the Photochemical Reduction of CO2 to Formate by Ruthenium Complexes. *J. Am. Chem. Soc.* **2020**, *142* (5), 2413–2428. https://doi.org/10.1021/jacs.9b11897.

(41)    Thaler, E.; Folting, K.; Huffman, J. C.; Caulton, K. G. Bis[Tris(Dimethylphosphinomethyl)Ethane]Hydridochromium(1+) Tetraethylborate(1-): The First Synthesis of a Cationic Hydride Complex from Triethylborate(1-). *Inorg. Chem.* **1987**, *26* (3), 374–377. https://doi.org/10.1021/ic00250a007.

(42)    Hanckel, J. M.; Darensbourg, M. Y. Anion Assisted Transfer of a Sterically Constrained Proton: Molecular Structure of Bis[1,2-Ethanediylbis(Diphenylphosphine)]Dicarbonylhydridomolybdenum Tetrachloroaluminate [HMo(CO)2(Ph2PCH2CH2PPh2)2+ AlCl4-]. *J. Am. Chem. Soc.* **1983**, *105* (23), 6979–6980. https://doi.org/10.1021/ja00361a049.

(43)    Darensbourg, M. Y.; Ludvig, M. M. Deprotonation of Molybdenum Carbonyl Hydrido Diphosphine [HMo(CO)2(PP)2]BF4 Complexes: Hard Anions as Proton Carriers. *Inorg. Chem.* **1986**, *25* (16), 2894–2898. https://doi.org/10.1021/ic00236a047.

(44)    Kristjansdottir, S. S.; Loendorf, A. J.; Norton, J. R. Kinetic and Thermodynamic Acidity of Hydrido Transition-Metal Complexes. 9. A Sterically Hindered Cationic Hydride, [H4Re(PMe2Ph)4]+. *Inorg. Chem.* **1991**, *30* (23), 4470–4471. https://doi.org/10.1021/ic00023a037.

(45)    Kurtz, D. A.; Dhar, D.; Elgrishi, N.; Kandemir, B.; McWilliams, S. F.; Howland, W. C.; Chen, C.-H.; Dempsey, J. L. Redox-Induced Structural Reorganization Dictates Kinetics of Cobalt(III) Hydride Formation via Proton-Coupled Electron Transfer. *J. Am. Chem. Soc.* **2021**, *143* (9), 3393–3406. https://doi.org/10.1021/jacs.0c11992.

(46)    Elgrishi, N.; Kurtz, D. A.; Dempsey, J. L. Reaction Parameters Influencing Cobalt Hydride Formation Kinetics: Implications for Benchmarking H2-Evolution Catalysts. *J. Am. Chem. Soc.* **2017**, *139* (1), 239–244. https://doi.org/10.1021/jacs.6b10148.

(47)    Thaler, E.; Folting, K.; Huffman, J. C.; Caulton, K. G. Bis[Tris(Dimethylphosphinomethyl)Ethane]Hydridochromium(1+) Tetraethylborate(1-): The First Synthesis of a Cationic Hydride

(48)    JORDAN, R. F.; NORTON, J. R. Proton-Transfer Reactions in Organometallic Chemistry. In *Mechanistic Aspects of Inorganic Reactions*; ACS Symposium Series; AMERICAN CHEMICAL SOCIETY, 1982; Vol. 198, pp 403–423. https://doi.org/10.1021/bk-1982-0198.ch017.

(49)    R. Morris, B. Isotope Effects in Reactions of Transition Metal Hydrides. In *Transition Metal Hydrides*; Dedieu, A., Ed.; Wiley-VCH, 1996.

(50)    Smith, K.-T.; Tilset, M.; Kristjansdottir, S. S.; Norton, J. R. Kinetic Isotope Effects on Metal to Nitrogen Proton Transfers. *Inorg. Chem.* **1995**, *34* (26), 6497–6504. https://doi.org/10.1021/ic00130a015.

(51)    Coetzee, J. F. Ionic Reactions in Acetonitrile. In *Progress in Physical Organic Chemistry*; John Wiley & Sons, Ltd, 1967; pp 45–92. https://doi.org/10.1002/9780470171837.ch2.

(52)    Coetzee, J. F.; Padmanabhan, G. R. PROPERTIES OF BASES IN ACETONITRILE AS SOLVENT. II. THE AUTOPROTOLYSIS CONSTANT OF ACETONITRILE. *J. Phys. Chem.* **1962**, *66* (9), 1708–1713. https://doi.org/10.1021/j100815a036.

(53)    Kolthoff, I. M.; Chantooni, M. K. Jr.; Bhowmik, S. Dissociation Constants of Uncharged and Monovalent Cation Acids in Dimethyl Sulfoxide. *J. Am. Chem. Soc.* **1968**, *90* (1), 23–28. https://doi.org/10.1021/ja01003a005.

(54)    Brönsted, J. N.; Pedersen, K. Die katalytische Zersetzung des Nitramids und ihre physikalisch-chemische Bedeutung. *Z. Für Phys. Chem.* **1924**, *108U* (1), 185–235. https://doi.org/10.1515/zpch-1924-10814.

(55)    Eigen, M. Proton Transfer, Acid-Base Catalysis, and Enzymatic Hydrolysis. Part I: ELEMENTARY PROCESSES. *Angew. Chem. Int. Ed. Engl.* **1964**, *3* (1), 1–19. https://doi.org/10.1002/anie.196400011.

(56)    Hibbert, F.; Long, F. A. Proton Transfer from Cyanocarbon Acids. IV. Kinetic Ionization Behavior of p-Nitrobenzyl Cyanide and Bromomalonitrile. *J. Am. Chem. Soc.* **1972**, *94* (8), 2647–2651. https://doi.org/10.1021/ja00763a014.

(57)    Marcus, R. A. Theoretical Relations among Rate Constants, Barriers, and Broensted Slopes of Chemical Reactions. *J. Phys. Chem.* **1968**, *72* (3), 891–899. https://doi.org/10.1021/j100849a019.

(58)    Kresge, A. J. The Brønsted Relation – Recent Developments. *Chem. Soc. Rev.* **1973**, *2* (4), 475–503. https://doi.org/10.1039/CS9730200475.

(59)    Bell, R. P. (Ronald P. *The Proton in Chemistry*; Ithaca, N.Y. : Cornell University Press, 1973.

(60)    Morris, R. H. Estimating the Wavenumber of Terminal Metal-Hydride Stretching Vibrations of Octahedral D6 Transition Metal Complexes. *Inorg. Chem.* **2018**, *57* (21), 13809–13821. https://doi.org/10.1021/acs.inorgchem.8b02314.

(61)    Perutz, R. N.; Procacci, B. Photochemistry of Transition Metal Hydrides. *Chem. Rev.* **2016**, *116* (15), 8506–8544. https://doi.org/10.1021/acs.chemrev.6b00204.

(62)    Rennie, B. E.; Eleftheriades, R. G.; Morris, R. H. Systematic Trends in the Electrochemical Properties of Transition Metal Hydride Complexes Discovered by Using the Ligand Acidity Constant Equation. *J. Am. Chem. Soc.* **2020**, *142* (41), 17607–17629. https://doi.org/10.1021/jacs.0c08000.

(63)    Ruiz-Morales, Y.; Schreckenbach, G.; Ziegler, T. Origin of the Hydridic 1H NMR Chemical Shift in Low-Valent Transition-Metal Hydrides. *Organometallics* **1996**, *15* (19), 3920–3923. https://doi.org/10.1021/om960218n.

(64)    Hamon, J.-R.; Hamon, P.; Toupet, L.; Costuas, K.; Saillard, J.-Y. Classical and Non-Classical Iron Hydrides: Synthesis, NMR Characterisation, Theoretical Investigation and X-Ray Crystal Structure of the Iron(IV) Dihydride 〚Cp*Fe(Dppe)(H)2〛+BF4−. *Comptes Rendus Chim.* **2002**, *5* (2), 89–98. https://doi.org/10.1016/S1631-0748(02)01327-9.

(65)    Castro, A. C.; Balcells, D.; Repisky, M.; Helgaker, T.; Cascella, M. First-Principles Calculation of 1H NMR Chemical Shifts of Complex Metal Polyhydrides: The Essential Inclusion of Relativity and

Dynamics. *Inorg. Chem.* **2020**, *59* (23), 17509–17518. https://doi.org/10.1021/acs.inorgchem.0c02753.

(66) Buckingham, A. D.; Stephens, P. J. 528. Proton Chemical Shifts in the Nuclear Magnetic Resonance Spectra of Transition-Metal Hydrides: Octahedral Complexes. *J. Chem. Soc. Resumed* **1964**, No. 0, 2747–2759. https://doi.org/10.1039/JR9640002747.

(67) Hartwig, J. *Organotransition Metal Chemistry: From Bonding to Catalysis*, 1st edition.; University Science books: Sausalito, Calif, 2009.

(68) Soper, J. D.; Mayer, J. M. Slow Hydrogen Atom Self-Exchange between Os(IV) Anilide and Os(III) Aniline Complexes: Relationships with Electron and Proton Transfer Self-Exchange. *J. Am. Chem. Soc.* **2003**, *125* (40), 12217–12229. https://doi.org/10.1021/ja036328k.

(69) Soper, J. D.; Mayer, J. M. Slow Hydrogen Atom Self-Exchange between Os(IV) Anilide and Os(III) Aniline Complexes: Relationships with Electron and Proton Transfer Self-Exchange. *J. Am. Chem. Soc.* **2003**, *125* (40), 12217–12229. https://doi.org/10.1021/ja036328k.

(70) Bryant, R. G. The NMR Time Scale. *J. Chem. Educ.* **1983**, *60* (11), 933. https://doi.org/10.1021/ed060p933.

(71) Nikitin, K.; O'Gara, R. Mechanisms and Beyond: Elucidation of Fluxional Dynamics by Exchange NMR Spectroscopy. *Chem. – Eur. J.* **2019**, *25* (18), 4551–4589. https://doi.org/10.1002/chem.201804123.

(72) Lee, K. J.; Noémie, E.; Banu, K.; Dempsey, J. L. Electrochemical and Spectroscopic Methods for Evaluating Molecular Electrocatalysts. *Nat. Rev. Chem.* **2017**, *1* (5). https://doi.org/10.1038/s41570-017-0039.

(73) Rountree, E. S.; Martin, D. J.; McCarthy, B. D.; Dempsey, J. L. Linear Free Energy Relationships in the Hydrogen Evolution Reaction: Kinetic Analysis of a Cobaloxime Catalyst. *ACS Catal.* **2016**, *6* (5), 3326–3335. https://doi.org/10.1021/acscatal.6b00667.

(74) Artero, V.; Saveant, J.-M. Toward the Rational Benchmarking of Homogeneous H2-Evolving Catalysts. *Energy Environ. Sci.* **2014**, *7* (11), 3808–3814. https://doi.org/10.1039/C4EE01709A.

(75) Rountree, E. S.; McCarthy, B. D.; Eisenhart, T. T.; Dempsey, J. L. Evaluation of Homogeneous Electrocatalysts by Cyclic Voltammetry. *Inorg. Chem.* **2014**, *53* (19), 9983–10002. https://doi.org/10.1021/ic500658x.

(76) Savéant, J. M.; Su, K. B. Homogeneous Redox Catalysis of Electrochemical Reaction: Part VI. Zone Diagram Representation of the Kinetic Regimes. *J. Electroanal. Chem. Interfacial Electrochem.* **1984**, *171* (1), 341–349. https://doi.org/10.1016/0022-0728(84)80125-4.

(77) Costentin, C.; Savéant, J.-M. Multielectron, Multistep Molecular Catalysis of Electrochemical Reactions: Benchmarking of Homogeneous Catalysts. *ChemElectroChem* **2014**, *1* (7), 1226–1236. https://doi.org/10.1002/celc.201300263.

(78) Wang, V. C.-C.; Johnson, B. A. Interpreting the Electrocatalytic Voltammetry of Homogeneous Catalysts by the Foot of the Wave Analysis and Its Wider Implications. *ACS Catal.* **2019**, *9* (8), 7109–7123. https://doi.org/10.1021/acscatal.9b00850.

(79) Adams, R. E.; Grusenmeyer, T. A.; Griffith, A. L.; Schmehl, R. H. Transition Metal Hydride Complexes as Mechanistic Models for Proton Reduction Catalysis. *Coord. Chem. Rev.* **2018**, *362*, 44–53. https://doi.org/10.1016/j.ccr.2018.02.014.

(80) Curtis, C. J.; Miedaner, A.; Ciancanelli, R.; Ellis, W. W.; Noll, B. C.; Rakowski DuBois, M.; DuBois, D. L. [Ni(Et2PCH2NMeCH2PEt2)2]2+ as a Functional Model for Hydrogenases. *Inorg. Chem.* **2003**, *42* (1), 216–227. https://doi.org/10.1021/ic020610v.

(81) Razavet, M.; Artero, V.; Fontecave, M. Proton Electroreduction Catalyzed by Cobaloximes: Functional Models for Hydrogenases. *Inorg. Chem.* **2005**, *44* (13), 4786–4795. https://doi.org/10.1021/ic050167z.

(82) Castro-Cruz, H. M.; Macías-Ruvalcaba, N. A. Porphyrin-Catalyzed Electrochemical Hydrogen Evolution Reaction. Metal-Centered and Ligand-Centered Mechanisms. *Coord. Chem. Rev.* **2022**, *458*, 214430. https://doi.org/10.1016/j.ccr.2022.214430.

(83) Waldie, K. M.; Brunner, F. M.; Kubiak, C. P. Transition Metal Hydride Catalysts for Sustainable Interconversion of CO2 and Formate: Thermodynamic and Mechanistic Considerations. *ACS Sustain. Chem. Eng.* **2018**, *6* (5), 6841–6848. https://doi.org/10.1021/acssuschemeng.8b00628.

(84) Dempsey, J. L.; Brunschwig, B. S.; Winkler, J. R.; Gray, H. B. Hydrogen Evolution Catalyzed by Cobaloximes. *Acc. Chem. Res.* **2009**, *42* (12), 1995–2004. https://doi.org/10.1021/ar900253e.

(85) Hu, X.; Brunschwig, B. S.; Peters, J. C. Electrocatalytic Hydrogen Evolution at Low Overpotentials by Cobalt Macrocyclic Glyoxime and Tetraimine Complexes. *J. Am. Chem. Soc.* **2007**, *129* (29), 8988–8998. https://doi.org/10.1021/ja067876b.

(86) Dempsey, J. L.; Brunschwig, B. S.; Winkler, J. R.; Gray, H. B. Hydrogen Evolution Catalyzed by Cobaloximes. *Acc. Chem. Res.* **2009**, *42* (12), 1995–2004. https://doi.org/10.1021/ar900253e.

(87) Dempsey, J. L.; Winkler, J. R.; Gray, H. B. Kinetics of Electron Transfer Reactions of H2-Evolving Cobalt Diglyoxime Catalysts. *J. Am. Chem. Soc.* **2010**, *132* (3), 1060–1065. https://doi.org/10.1021/ja9080259.

(88) Natali, M. Elucidating the Key Role of PH on Light-Driven Hydrogen Evolution by a Molecular Cobalt Catalyst. *ACS Catal.* **2017**, *7* (2), 1330–1339. https://doi.org/10.1021/acscatal.6b03087.

(89) Cao, Y.-C.; Shi, L.-L.; Li, M.; You, B.; Liao, R.-Z. Deciphering the Selectivity of the Electrochemical CO2 Reduction to CO by a Cobalt Porphyrin Catalyst in Neutral Aqueous Solution: Insights from DFT Calculations. *ChemistryOpen* **2023**, *12* (2), e202200254. https://doi.org/10.1002/open.202200254.

(90) Grass, V.; Lexa, D.; Savéant, J.-M. Electrochemical Generation of Rhodium Porphyrin Hydrides. Catalysis of Hydrogen Evolution. *J. Am. Chem. Soc.* **1997**, *119* (32), 7526–7532. https://doi.org/10.1021/ja964100+.

(91) Bhugun, I.; Lexa, D.; Savéant, J.-M. Homogeneous Catalysis of Electrochemical Hydrogen Evolution by Iron(0) Porphyrins. *J. Am. Chem. Soc.* **1996**, *118* (16), 3982–3983. https://doi.org/10.1021/ja954326x.

(92) Margarit, C. G.; Asimow, N. G.; Thorarinsdottir, A. E.; Costentin, C.; Nocera, D. G. Impactful Role of Cocatalysts on Molecular Electrocatalytic Hydrogen Production. *ACS Catal.* **2021**, *11* (8), 4561–4567. https://doi.org/10.1021/acscatal.1c00253.

(93) Ceballos, B. M.; Yang, J. Y. Directing the Reactivity of Metal Hydrides for Selective CO2 Reduction. *Proc. Natl. Acad. Sci.* **2018**, *115* (50), 12686–12691. https://doi.org/10.1073/pnas.1811396115.

(94) Chen, L.; Guo, Z.; Wei, X.-G.; Gallenkamp, C.; Bonin, J.; Anxolabéhère-Mallart, E.; Lau, K.-C.; Lau, T.-C.; Robert, M. Molecular Catalysis of the Electrochemical and Photochemical Reduction of CO2 with Earth-Abundant Metal Complexes. Selective Production of CO vs HCOOH by Switching of the Metal Center. *J. Am. Chem. Soc.* **2015**, *137* (34), 10918–10921. https://doi.org/10.1021/jacs.5b06535.

(95) Ceballos, B. M.; Yang, J. Y. Highly Selective Electrocatalytic CO2 Reduction by [Pt(Dmpe)2]2+ through Kinetic and Thermodynamic Control. *Organometallics* **2020**, *39* (9), 1491–1496. https://doi.org/10.1021/acs.organomet.9b00720.

(96) Barlow, J. M.; Yang, J. Y. Thermodynamic Considerations for Optimizing Selective CO2 Reduction by Molecular Catalysts. *ACS Cent. Sci.* **2019**, *5* (4), 580–588. https://doi.org/10.1021/acscentsci.9b00095.

(97) Wiedner, E. S.; Chambers, M. B.; Pitman, C. L.; Bullock, R. M.; Miller, A. J. M.; Appel, A. M. Thermodynamic Hydricity of Transition Metal Hydrides. *Chem. Rev.* **2016**, *116* (15), 8655–8692. https://doi.org/10.1021/acs.chemrev.6b00168.

(98) Loipersberger, M.; Zee, D. Z.; Panetier, J. A.; Chang, C. J.; Long, J. R.; Head-Gordon, M. Computational Study of an Iron(II) Polypyridine Electrocatalyst for CO2 Reduction: Key Roles for Intramolecular Interactions in CO2 Binding and Proton Transfer. *Inorg. Chem.* **2020**, *59* (12), 8146–8160. https://doi.org/10.1021/acs.inorgchem.0c00454.

(99) Kang, P.; Cheng, C.; Chen, Z.; Schauer, C. K.; Meyer, T. J.; Brookhart, M. Selective Electrocatalytic Reduction of CO2 to

Formate by Water-Stable Iridium Dihydride Pincer Complexes. *J. Am. Chem. Soc.* **2012**, *134* (12), 5500–5503. https://doi.org/10.1021/ja300543s.

(100) Roy, S.; Sharma, B.; Pécaut, J.; Simon, P.; Fontecave, M.; Tran, P. D.; Derat, E.; Artero, V. Molecular Cobalt Complexes with Pendant Amines for Selective Electrocatalytic Reduction of Carbon Dioxide to Formic Acid. *J. Am. Chem. Soc.* **2017**, *139* (10), 3685–3696. https://doi.org/10.1021/jacs.6b11474.

(101) Loewen, N. D.; Neelakantan, T. V.; Berben, L. A. Renewable Formate from C–H Bond Formation with CO $_2$ : Using Iron Carbonyl Clusters as Electrocatalysts. *Acc. Chem. Res.* **2017**, *50* (9), 2362–2370. https://doi.org/10.1021/acs.accounts.7b00302.

(102) Yang, J. Y.; Kerr, T. A.; Wang, X. S.; Barlow, J. M. Reducing CO2 to HCO2– at Mild Potentials: Lessons from Formate Dehydrogenase. *J. Am. Chem. Soc.* **2020**, *142* (46), 19438–19445. https://doi.org/10.1021/jacs.0c07965.

(103) Loewen, N. D.; Berben, L. A. Secondary Coordination Sphere Design to Modify Transport of Protons and CO $_2$. *Inorg. Chem.* **2019**, *58* (24), 16849–16857. https://doi.org/10.1021/acs.inorgchem.9b03102.

(104) Wiedner, E. S.; Appel, A. M.; Raugei, S.; Shaw, W. J.; Bullock, R. M. Molecular Catalysts with Diphosphine Ligands Containing Pendant Amines. *Chem. Rev.* **2022**, *122* (14), 12427–12474. https://doi.org/10.1021/acs.chemrev.1c01001.

(105) Wilson, A. D.; Newell, R. H.; McNevin, M. J.; Muckerman, J. T.; Rakowski DuBois, M.; DuBois, D. L. Hydrogen Oxidation and Production Using Nickel-Based Molecular Catalysts with Positioned Proton Relays. *J. Am. Chem. Soc.* **2006**, *128* (1), 358–366. https://doi.org/10.1021/ja056442y.

(106) Helm, M. L.; Stewart, M. P.; Bullock, R. M.; DuBois, M. R.; DuBois, D. L. A Synthetic Nickel Electrocatalyst with a Turnover Frequency Above 100,000 S−1 for H2 Production. *Science* **2011**, *333* (6044), 863–866. https://doi.org/10.1126/science.1205864.

(107) Kilgore, U. J.; Roberts, J. A. S.; Pool, D. H.; Appel, A. M.; Stewart, M. P.; DuBois, M. R.; Dougherty, W. G.; Kassel, W. S.; Bullock, R. M.; DuBois, D. L. [Ni(PPh2NC6H4X2)2]2+ Complexes as Electrocatalysts for H2 Production: Effect of Substituents, Acids, and Water on Catalytic Rates. *J. Am. Chem. Soc.* **2011**, *133* (15), 5861–5872. https://doi.org/10.1021/ja109755f.

(108) Rountree, E. S.; Dempsey, J. L. Potential-Dependent Electrocatalytic Pathways: Controlling Reactivity with PKa for Mechanistic Investigation of a Nickel-Based Hydrogen Evolution Catalyst. *J. Am. Chem. Soc.* **2015**, *137* (41), 13371–13380. https://doi.org/10.1021/jacs.5b08297.

(109) Wiedner, E. S.; Brown, H. J. S.; Helm, M. L. Kinetic Analysis of Competitive Electrocatalytic Pathways: New Insights into Hydrogen Production with Nickel Electrocatalysts. *J. Am. Chem. Soc.* **2016**, *138* (2), 604–616. https://doi.org/10.1021/jacs.5b10853.

(110) Reuillard, B.; Costentin, C.; Artero, V. Deciphering Reversible Homogeneous Catalysis of the Electrochemical H2 Evolution and Oxidation: Role of Proton Relays and Local Concentration Effects. *Angew. Chem. n/a* (n/a), e202302779. https://doi.org/10.1002/ange.202302779.

(111) Jacobsen, G. M.; Yang, J. Y.; Twamley, B.; Wilson, A. D.; Bullock, R. M.; DuBois, M. R.; DuBois, D. L. Hydrogen Production Using Cobalt-Based Molecular Catalysts Containing a Proton Relay in the Second Coordination Sphere. *Energy Environ. Sci.* **2008**, *1* (1), 167–174. https://doi.org/10.1039/B805309J.

(112) M. Roubelakis, M.; Kwabena Bediako, D.; K. Dogutan, D.; G. Nocera, D. Proton -Coupled Electron Transfer Kinetics for the Hydrogen Evolution Reaction of Hangman Porphyrins. *Energy Environ. Sci.* **2012**, *5* (7), 7737–7740. https://doi.org/10.1039/C2EE21123H.

(113) Solis, B. H.; Maher, A. G.; Honda, T.; Powers, D. C.; Nocera, D. G.; Hammes-Schiffer, S. Theoretical Analysis of Cobalt Hangman Porphyrins: Ligand Dearomatization and Mechanistic Implications for Hydrogen Evolution. *ACS Catal.* **2014**, *4* (12), 4516–4526. https://doi.org/10.1021/cs501454y.

(114) Roubelakis, M. M.; Bediako, D. K.; Dogutan, D. K.; Nocera, D. G. Influence of the Proton Relay Spacer on Hydrogen Electrocatalysis

by Cobalt Hangman Porphyrins. *J. Porphyr. Phthalocyanines* **2021**, *25* (07n08), 714–723. https://doi.org/10.1142/S108842462150067X.

(115) Graham, D. J.; Nocera, D. G. Electrocatalytic H2 Evolution by Proton-Gated Hangman Iron Porphyrins. *Organometallics* **2014**, *33* (18), 4994–5001. https://doi.org/10.1021/om500300e.

(116) Bhunia, S.; Rana, A.; Hematian, S.; Karlin, K. D.; Dey, A. Proton Relay in Iron Porphyrins for Hydrogen Evolution Reaction. *Inorg. Chem.* **2021**, *60* (18), 13876–13887. https://doi.org/10.1021/acs.inorgchem.1c01079.

(117) *Role of pendant proton relays and proton-coupled electron transfer on the hydrogen evolution reaction by nickel hangman porphyrins*. https://doi.org/10.1073/pnas.1414908111.

(118) Mukherjee, J.; Siewert, I. Manganese and Rhenium Tricarbonyl Complexes Equipped with Proton Relays in the Electrochemical CO2 Reduction Reaction. *Eur. J. Inorg. Chem.* **2020**, *2020* (46), 4319–4333. https://doi.org/10.1002/ejic.202000738.

(119) Fokin, I.; Denisiuk, A.; Würtele, C.; Siewert, I. The Impact of a Proton Relay in Binuclear α-Diimine-Mn(CO)3 Complexes on the CO2 Reduction Catalysis. *Inorg. Chem.* **2019**, *58* (16), 10444–10453. https://doi.org/10.1021/acs.inorgchem.9b00992.

(120) Madsen, M. R.; Jakobsen, J. B.; Rønne, M. H.; Liang, H.; Hammershøj, H. C. D.; Nørby, P.; Pedersen, S. U.; Skrydstrup, T.; Daasbjerg, K. Evaluation of the Electrocatalytic Reduction of Carbon Dioxide Using Rhenium and Ruthenium Bipyridine Catalysts Bearing Pendant Amines in the Secondary Coordination Sphere. *Organometallics* **2020**, *39* (9), 1480–1490. https://doi.org/10.1021/acs.organomet.9b00815.

(121) Rønne, M. H.; Cho, D.; Madsen, M. R.; Jakobsen, J. B.; Eom, S.; Escoudé, É.; Hammershøj, H. C. D.; Nielsen, D. U.; Pedersen, S. U.; Baik, M.-H.; Skrydstrup, T.; Daasbjerg, K. Ligand-Controlled Product Selectivity in Electrochemical Carbon Dioxide Reduction Using Manganese Bipyridine Catalysts. *J. Am. Chem. Soc.* **2020**, *142* (9), 4265–4275. https://doi.org/10.1021/jacs.9b11806.

(122) Franco, F.; Cometto, C.; Vallana, F. F.; Sordello, F.; Priola, E.; Minero, C.; Nervi, C.; Gobetto, R. A Local Proton Source in a [Mn(Bpy-R)(CO)3Br]-Type Redox Catalyst Enables CO2 Reduction Even in the Absence of Brønsted Acids. *Chem. Commun.* **2014**, *50* (93), 14670–14673. https://doi.org/10.1039/C4CC05563B.

(123) Franco, F.; Cometto, C.; Nencini, L.; Barolo, C.; Sordello, F.; Minero, C.; Fiedler, J.; Robert, M.; Gobetto, R.; Nervi, C. Local Proton Source in Electrocatalytic CO2 Reduction with [Mn(Bpy–R)(CO)3Br] Complexes. *Chem. – Eur. J.* **2017**, *23* (20), 4782–4793. https://doi.org/10.1002/chem.201605546.

(124) Hawecker, J.; Lehn, J.-M.; Ziessel, R. Electrocatalytic Reduction of Carbon Dioxide Mediated by Re(Bipy)(CO)3Cl (Bipy = 2,2'-Bipyridine). *J. Chem. Soc. Chem. Commun.* **1984**, No. 6, 328–330. https://doi.org/10.1039/C39840000328.

(125) Clegg, W. Kinetic Evidence for Intramolecular Proton Transfer Between Nickel and Coordinated Thiolate. *Inorg. Chem.* **2002**, *41* (5), 1128–1135. https://doi.org/10.1021/ic0104306.

(126) Petrou, A. L.; Koutselos, A. D.; Wahab, H. S.; Clegg, W.; Harrington, R. W.; Henderson, R. A. Kinetic and Theoretical Studies on the Protonation of [Ni(2-SC6H4N){PhP(CH2CH2PPh2)2}]+: Nitrogen versus Sulfur as the Protonation Site. *Inorg. Chem.* **2011**, *50* (3), 847–857. https://doi.org/10.1021/ic101444d.

(127) Chalkley, M. J.; Oyala, P. H.; Peters, J. C. Cp* Noninnocence Leads to a Remarkably Weak C–H Bond via Metallocene Protonation. *J. Am. Chem. Soc.* **2019**, *141* (11), 4721–4729. https://doi.org/10.1021/jacs.9b00193.

(128) Chalkley, M. J.; Del Castillo, T. J.; Matson, B. D.; Peters, J. C. Fe-Mediated Nitrogen Fixation with a Metallocene Mediator: Exploring PKa Effects and Demonstrating Electrocatalysis. *J. Am. Chem. Soc.* **2018**, *140* (19), 6122–6129. https://doi.org/10.1021/jacs.8b02335.

(129) Chalkley, M. J.; Del Castillo, T. J.; Matson, B. D.; Roddy, J. P.; Peters, J. C. Catalytic N2-to-NH3 Conversion by Fe at Lower Driving Force: A Proposed Role for Metallocene-Mediated PCET. *ACS Cent. Sci.* **2017**, *3* (3), 217–223. https://doi.org/10.1021/acscentsci.7b00014.

(130) Schild, D. J.; Drover, M. W.; Oyala, P. H.; Peters, J. C. Generating Potent C–H PCET Donors: Ligand-Induced Fe-to-Ring Proton Migration from a Cp*FeIII–H Complex Demonstrates a Promising Strategy. *J. Am. Chem. Soc.* **2020**, *142* (44), 18963–18970. https://doi.org/10.1021/jacs.0c09363.

(131) Pitman, C. L.; Finster, O. N. L.; Miller, A. J. M. Cyclopentadiene-Mediated Hydride Transfer from Rhodium Complexes. *Chem. Commun.* **2016**, *52* (58), 9105–9108. https://doi.org/10.1039/C6CC00575F.

(132) Quintana, L. M. A.; Johnson, S. I.; Corona, S. L.; Villatoro, W.; Goddard, W. A.; Takase, M. K.; VanderVelde, D. G.; Winkler, J. R.; Gray, H. B.; Blakemore, J. D. Proton-Hydride Tautomerism in Hydrogen Evolution Catalysis. *Proc. Natl. Acad. Sci. U. S. A.* **2016**, *113* (23), 6409–6414. https://doi.org/10.1073/pnas.1606018113.

(133) Kurtz, D. A.; Dempsey, J. L. Proton-Coupled Electron Transfer Kinetics for the Photoinduced Generation of a Cobalt(III)-Hydride Complex. *Inorg. Chem.* **2019**, *58* (24), 16510–16517. https://doi.org/10.1021/acs.inorgchem.9b02445.

(134) Curphey, T. J.; Santer, J. O.; Rosenblum, M.; Richards, J. H. PROTONATION OF METALLOCENES BY STRONG ACIDS. STRUCTURE OF THE CATION. *J. Am. Chem. Soc.* **1960**, *82* (19), 5249–5250. https://doi.org/10.1021/ja01504a062.

(135) Malischewski, M.; Seppelt, K.; Sutter, J.; Heinemann, F. W.; Dittrich, B.; Meyer, K. Protonation of Ferrocene: A Low-Temperature X-Ray Diffraction Study of [Cp2FeH](PF6) Reveals an Iron-Bound Hydrido Ligand. *Angew. Chem. Int. Ed.* **2017**, *56* (43), 13372–13376. https://doi.org/10.1002/anie.201704854.

(136) Koelle, U.; Infelta, P. P.; Graetzel, M. Kinetics and Mechanism of the Reduction of Protons to Hydrogen by Cobaltocene. *Inorg. Chem.* **1988**, *27* (5), 879–883. https://doi.org/10.1021/ic00278a026.

(137) Tard, C.; Pickett, C. J. Structural and Functional Analogues of the Active Sites of the [Fe]-, [NiFe]-, and [FeFe]-Hydrogenases. *Chem. Rev.* **2009**, *109* (6), 2245–2274. https://doi.org/10.1021/cr800542q.

(138) Saouma, C. T.; Pinney, M. M.; Mayer, J. M. Electron Transfer and Proton-Coupled Electron Transfer Reactivity and Self-Exchange of Synthetic [2Fe–2S] Complexes: Models for Rieske and MitoNEET Clusters. *Inorg. Chem.* **2014**, *53* (6), 3153–3161. https://doi.org/10.1021/ic403131p.

(139) Zhang, W.; Moore, C. E.; Zhang, S. Multiple Proton-Coupled Electron Transfers at a Tricopper Cluster: Modeling the Reductive Regeneration Process in Multicopper Oxidases. *J. Am. Chem. Soc.* **2022**, *144* (4), 1709–1717. https://doi.org/10.1021/jacs.1c10948.

(140) Grönberg, K. L. C.; Henderson, R. A.; Oglieve, K. E. A Unified Mechanism for the Stoichiometric Reduction of H+ and C2H2 by [Fe4S4(SPh)4]3− in MeCN. *J. Chem. Soc. Dalton Trans.* **1998**, No. 18, 3093–3104. https://doi.org/10.1039/a803223h.

(141) Bates, K.; Garrett, B.; Henderson, R. A. Rates of Proton Transfer to Fe–S-Based Clusters: Comparison of Clusters Containing {MFe($\mu_2$-S)$_2$}$^{n+}$ and {MFe$_3$($\mu_3$-S)$_4$}$^{n+}$ (M = Fe, Mo, or W) Cores. *Inorg. Chem.* **2007**, *46* (26), 11145–11155. https://doi.org/10.1021/ic7015484.

(142) Yamamura, T.; Christou, G.; Holm, R. H. The Homogeneous Hydrogen-Evolving Systems [Mo2Fe6S8(SPh)9]4-,5-/C6H5SH: Reaction Characteristics, Kinetics, and Possible Mechanisms. *Inorg. Chem.* **1983**, *22* (6), 939–949. https://doi.org/10.1021/ic00148a019.

(143) Chu, K.-T.; Liu, Y.-C.; Chung, M.-W.; Poerwoprajitno, A. R.; Lee, G.-H.; Chiang, M.-H. Energy-Efficient Hydrogen Evolution by Fe–S Electrocatalysts: Mechanistic Investigations. *Inorg. Chem.* **2018**, *57* (13), 7620–7630. https://doi.org/10.1021/acs.inorgchem.8b00543.

(144) Amtawong, J.; Nguyen, A. I.; Tilley, T. D. Mechanistic Aspects of Cobalt–Oxo Cubane Clusters in Oxidation Chemistry. *J. Am. Chem. Soc.* **2022**, *144* (4), 1475–1492. https://doi.org/10.1021/jacs.1c11445.

(145) Fertig, A. A.; Brennessel, W. W.; McKone, J. R.; Matson, E. M. Concerted Multiproton–Multielectron Transfer for the Reduction of $O_2$ to $H_2O$ with a Polyoxovanadate Cluster. *J. Am. Chem. Soc.*

**2021**, *143* (38), 15756–15768. https://doi.org/10.1021/jacs.1c07076.

(146) Lubitz, W.; Ogata, H.; Rüdiger, O.; Reijerse, E. Hydrogenases. *Chem. Rev.* **2014**, *114* (8), 4081–4148. https://doi.org/10.1021/cr4005814.

(147) Ezzaher, S.; Capon, J.-F.; Gloaguen, F.; Petillon, F. Y.; Schollhammer, P.; Talarmin, J.; Pichon, R.; Kervarec, N. Evidence for the Formation of Terminal Hydrides by Protonation of an Asymmetric Iron Hydrogenase Active Site Mimic.

(148) Zhao, X.; Georgakaki, I. P.; Miller, M. L.; Yarbrough, J. C.; Darensbourg, M. Y. H/D Exchange Reactions in Dinuclear Iron Thiolates as Activity Assay Models of Fe–H$_2$Ase. *J. Am. Chem. Soc.* **2001**, *123* (39), 9710–9711. https://doi.org/10.1021/ja0167046.

(149) Eur J Inorg Chem - 2011 - Liu - Density Functional Calculations on Protonation of the FeFe -Hydrogenase Model Complex Fe2 .Pdf.

(150) Liu, Z.-P.; Hu, P. Mechanism of H2 Metabolism on Fe-Only Hydrogenases.

(151) Eilers, G.; Schwartz, L.; Stein, M.; Zampella, G.; de Gioia, L.; Ott, S.; Lomoth, R. Ligand versus Metal Protonation of an Iron Hydrogenase Active Site Mimic. *Chem. - Eur. J.* **2007**, *13* (25), 7075–7084. https://doi.org/10.1002/chem.200700019.

(152) Jablonskytė, A.; Wright, J. A.; Pickett, C. J. Mechanistic Aspects of the Protonation of [FeFe]-Hydrogenase Subsite Analogues. *Dalton Trans.* **2010**, *39* (12), 3026–3034. https://doi.org/10.1039/B923191A.

(153) Jablonskytė, A.; Webster, L. R.; Simmons, T. R.; Wright, J. A.; Pickett, C. J. Electronic Control of the Protonation Rates of Fe–Fe Bonds. *J. Am. Chem. Soc.* **2014**, *136* (37), 13038–13044. https://doi.org/10.1021/ja506693m.

(154) Wang, S.; Aster, A.; Mirmohades, M.; Lomoth, R.; Hammarström, L. Structural and Kinetic Studies of Intermediates of a Biomimetic Diiron Proton-Reduction Catalyst. *Inorg. Chem.* **2018**, *57* (2), 768–776. https://doi.org/10.1021/acs.inorgchem.7b02687.

(155) Ćorić, I.; Holland, P. L. Insight into the Iron–Molybdenum Cofactor of Nitrogenase from Synthetic Iron Complexes with Sulfur, Carbon, and Hydride Ligands. *J. Am. Chem. Soc.* **2016**, *138* (23), 7200–7211. https://doi.org/10.1021/jacs.6b00747.

(156) Seefeldt, L. C.; Yang, Z.-Y.; Lukoyanov, D. A.; Harris, D. F.; Dean, D. R.; Raugei, S.; Hoffman, B. M. Reduction of Substrates by Nitrogenases. *Chem. Rev.* **2020**, *120* (12), 5082–5106. https://doi.org/10.1021/acs.chemrev.9b00556.

(157) Igarashi, R. Y.; Laryukhin, M.; Dos Santos, P. C.; Lee, H.-I.; Dean, D. R.; Seefeldt, L. C.; Hoffman, B. M. Trapping H⁻ Bound to the Nitrogenase FeMo-Cofactor Active Site during H$_2$ Evolution: Characterization by ENDOR Spectroscopy. *J. Am. Chem. Soc.* **2005**, *127* (17), 6231–6241. https://doi.org/10.1021/ja043596p.

(158) Carr, C. R.; Taheri, A.; Berben, L. A. Fast Proton Transfer and Hydrogen Evolution Reactivity Mediated by [Co$_{13}$C$_2$(CO)$_{24}$]$^{4-}$. *J. Am. Chem. Soc.* **2020**, *142* (28), 12299–12305. https://doi.org/10.1021/jacs.0c04034.

(159) Pattanayak, S.; Berben, L. A. Cobalt Carbonyl Clusters Enable Independent Control of Two Proton Transfer Rates in the Mechanism for Hydrogen Evolution. *ChemElectroChem* **2021**, *8* (13), 2488–2494. https://doi.org/10.1002/celc.202100402.

(160) Li, C.-B.; Bagnall, A. J.; Sun, D.; Rendon, J.; Koepf, M.; Gambarelli, S.; Mouesca, J.-M.; Chavarot-Kerlidou, M.; Artero, V. Electrocatalytic Reduction of Protons to Dihydrogen by the Cobalt Tetraazamacrocyclic Complex [Co(N4H)Cl2]+: Mechanism and Benchmarking of Performances. *Sustain. Energy Fuels* **2021**, *6* (1), 143–149. https://doi.org/10.1039/D1SE01267C.

(161) Sun, D.; Karippara Harshan, A.; Pécaut, J.; Hammes-Schiffer, S.; Costentin, C.; Artero, V. Hydrogen Evolution Mediated by Cobalt Diimine-Dioxime Complexes: Insights into the Role of the Ligand Acid/Base Functionalities. *ChemElectroChem* **2021**, *8* (14), 2671–2679. https://doi.org/10.1002/celc.202100413.

# ARTICLE